Information Engineering Letters, ISSN: **2163-4114**
Volume **3**, Number **3**, September, **2013**

Diversity-based Feature Partitioning for Combination of Nearest Mean Classifier

Abdullah

Dept. of Information System, Universitas Islam Indragiri, Tembilahan 29200, Indonesia

abdialam@yahoo.com

doi.10.5729/iel.vol3.issue3.16

Keywords: Nearest mean classifier, Feature partitioning, Multiple classifier combination

Abstract. Nearest Mean Classifier (NMC) provides good performance for small sample training. However concatenate different features into a high dimensional feature vectors and process them using a single NMC generally does not give good results because dimensionality problem. Most methods used to address the dimensionality problem focuses on feature selection method, choosing a single feature subset, while ignoring the rest. Although there are several algorithms have been proposed, but there are drawbacks to using of feature selection method. The assumption that a large set of input features can be reduced to a small subset of relevant features is not always true. In some cases the target feature is actually affected by most of the input features and removing features will cause a significant loss of important information. Thus, the classifier may achieve a lower level of accuracy than the classifiers that accesses all the relevant features. In this method the feature set clusters into different feature subset. NMC ensembles constructed by assigning each individual classifier in the ensemble with a cluster of different feature subset. The advantage of this approach is that all of available information in the training set is used. There is no irrelevant feature in the training set are eliminated. Based on experimental results the new technique significantly improve the nearest mean classifier (NMC) with 95% confidence.

1. Introduction

Nearest mean classifier (NMC) was introduced by Fukunaga [1] as a classifier which uses the similarity between patterns to determine the classification. For each class, NMC computes the class mean (or centroid) of the training patterns. Similarity values obtained by calculate the Euclidean distance between the test patterns to the class mean of the training patterns. NMC classifies any test patterns (or unknown objects) to the class whose the class mean is closest to this test patterns. NMC has been successfully applied to many classification problems and showed good performance and very strong [2]. Furthermore NMC provides good performance for small training sample problem [3]. Small training sample problems are problems with the number of samples is much smaller than the number of features [4]. However concatenate different features into a high dimensional feature vectors and process them using a single NMC generally does not give good results because dimensionality problem. Most methods used to address the dimensionality problem focuses on feature selection method, choosing a single feature subset, while ignoring the rest. Although there are several algorithms have been proposed, but there are drawbacks to using of feature selection method. The assumption that a large set of input features can be reduced to a small subset of relevant features is not always true. In some cases the target feature is actually affected by most of the input features and removing features will cause a significant loss of important information. Thus, the classifier may achieve a lower level of accuracy than the classifiers that accesses all the relevant features [5].

Multiple classifier combination aims to obtain the final classification decision by integrating the output of several individual classifier [6]. The concept of multiple classifier system was first proposed by Suen et al. [7] in order to improve the results of character recognition. In the literature, this research area is defined by a number of different names, such as multiple classifier combination, combining classifiers, classifier ensembles, committees of learner, mixtures of experts, the consensus theory, hybrid methods, decision combination, multiple experts, cooperative agents, opinion pool, sensor fusion [8]. Regardless of the different names that have been defined, the multiple classifier system combine several classifiers to obtain the final classification result. Currently. Combining multiple classifier is considered as a new direction for pattern recognition. Multiple classifier system has been shown to be very helpful in improving the classification performance over single classifier approach [9].

One of approach that used to construct a diverse classifier ensemble is the manipulation of input features. This approach assigns different subset of features among individual classifier in the ensemble (usually, the same base classifier used). The main method of this approach is the random subspace method [10] which assigns a random subset of the original features to individual classifier (on the same training sample). Feature subsets can overlap, and their sizes are usually identical. Other methods that have similar idea with this method is the multiple feature subsets [11] and the attributes bagging [12]. All of these methods are similar in the way they assign features randomly to individual classifier in the ensemble. The differences are in the determination of subset and ensemble size. A new method that uses this approach is the feature subset partitioning. In this method the feature set clusters into different feature subset. Ensemble constructed by assigning each individual classifier in the ensemble with a cluster of different feature subset from the pool of available features. The advantage of this approach is that all available information in the training set is used. There is no irrelevant feature in the training set are eliminated. Irrelevant feature does not need to be eliminated in the combination of classifier, because this omitted feature may contain valuable information [13].

2. Proposed Method

In this method, a group of classifier built from the training data. Based on the original training data a disjoint feature subset decomposition was performed. Ensemble classifier is built based on the feature subset partition. Prediction class label of unknown pattern obtained by aggregating predictions using a combiner. Fig. 1 shows the general idea of this method.

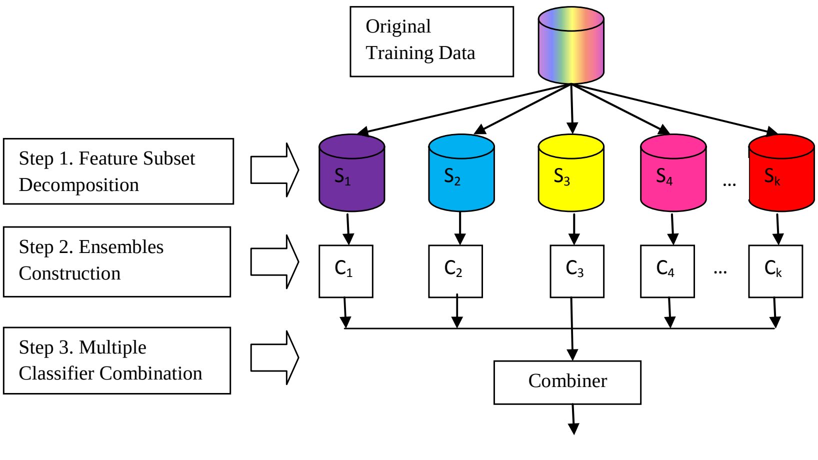

Figure 1. General idea of diversity-based feature clustering for classifier combination

Based on this idea an algorithm constructed to perform feature subset decomposition. Furthermore NMC ensemble constructed by projection of the feature subset of original training data. The pseudocode for this algorithm is as follows:

Input: The n features training set and the class labels

process:

1. Make two subset of features that provides the greatest diversity
2. Choose any of the remaining features
3. Create possible features partition
4. Select the feature partition that provides maximum diversity measure
5. Go to step 2 until all of features have been partitioned
6. Use the feature partition to construct NMC ensemble

Output: a classifier ensemble C *

Input training set and class labels are required inputs. The next step was built two feature subset that gives the maximum value of diversity in the ensemble. Diversity is measured based on support diversity measure which is more frequently an agreement among the individual NMC provides small value diversity. Furthermore disjoint feature set partitioning for all feature in such a way that provides maximum diversity in the NMC ensembles. The last step the feature subset used to construct NMC ensembles. Overall the steps as shown in Fig. 2.

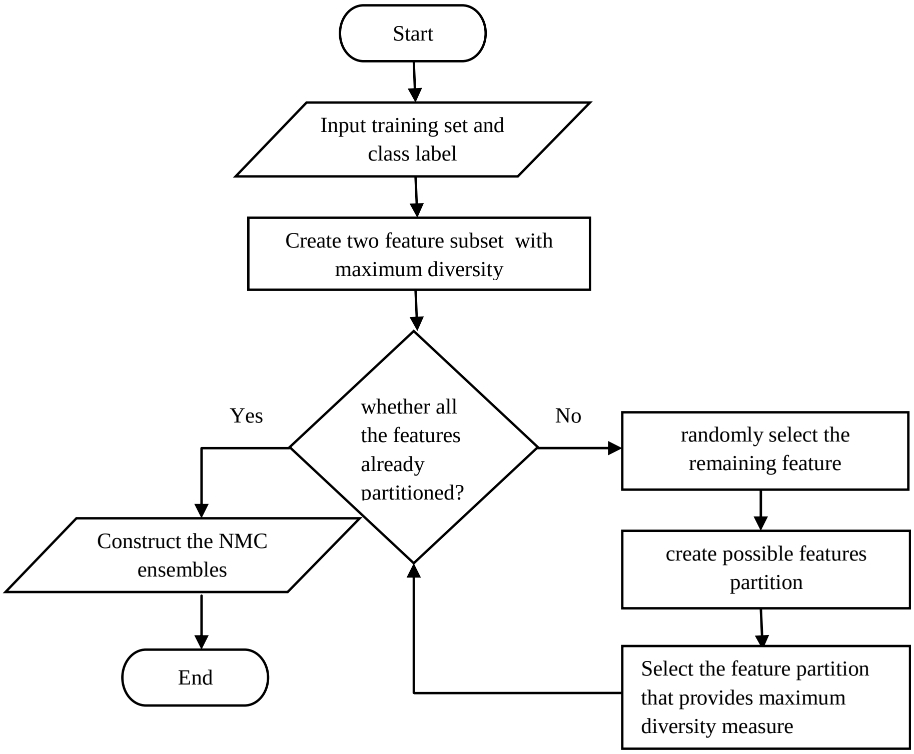

Figure 2. The flowchart of diversity-based feature clustering algorithm for NMC

3. Research Methodology

In order to evaluate the performance of this method hence multiple NMC combination constructed to test its ability to perform classification task. The method of research as follows: (1) NMC ensembles is designed using this new algorithm. (2) Applied the multiple NMC combination for classification task (3) Classification experiments using NMC combination performed using several datasets. (4) The results which obtained evaluated by compare this NMC combination with the original NMC. The steps of the research can be seen in Fig. 3.

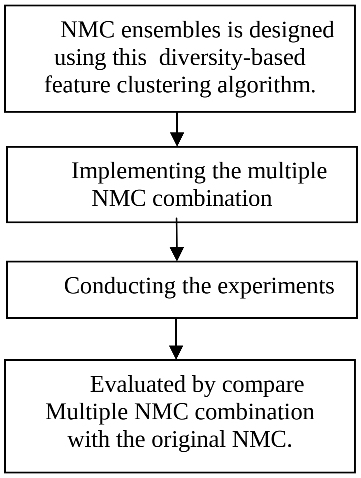

Figure 3. The steps of the research

4. Experiment Results

The results of individual nearest mean classifier accuracy using several datasets are presented in Table 1.

Table 1. The accuracy of individual nearest mean classifier

# Experiment	Fruit	Pima	Iris	Wine	Glass	Liver	Lenses	Statlog (heart)	Ionosphere	Soybean
1	53.57	63.02	92.00	71.91	45.79	55.07	66.67	64.44	69.23	75.24
2	52.38	62.89	91.33	72.47	44.86	55.94	70.83	62.96	69.80	74.59
3	50.00	63.41	92.67	72.47	45.33	54.20	62.50	62.22	70.66	75.90
4	53.57	63.15	92.67	72.47	43.93	54.49	70.83	64.07	71.79	75.24
5	53.57	63.67	92.00	72.47	44.39	53.91	58.33	64.44	70.09	74.59
6	52.38	62.89	92.00	72.47	44.86	56.23	66.67	64.07	68.66	75.57
7	48.81	63.41	92.67	73.03	44.39	55.94	75.00	63.70	69.80	76.22
8	52.38	63.28	92.00	73.03	44.86	55.36	54.17	64.07	70.37	75.24
9	54.76	63.67	91.33	71.35	45.33	55.07	75.00	63.70	70.09	73.94
10	51.19	63.54	92.00	73.03	43.46	55.65	70.83	64.07	70.94	73.62
Average	**52.26**	**63.29**	**92.67**	**72.47**	**44.72**	**55.19**	**67.08**	**63.78**	**70.14**	**75.02**
Standard deviation	1.81	0.30	0.49	0.53	0.70	0.79	6.93	0.69	0.88	0.83

The experiment results of multiple nearest mean classifier accuracy using the diversity based feature partitioning algorithm using several datasets are presented in Table 2.

Table 2. The accuracy of multiple nearest mean classifier combination

# Experiment	Fruit	Pima	Iris	Wine	Glass	Liver	Lenses	Statlog (heart)	Ionosphere	Soybean
1	95.24	67.06	87.33	95.51	37.85	53.33	75.00	79.26	80.06	75.57
2	96.43	67.71	86.67	93.26	48.60	55.07	62.50	82.59	76.92	76.55
3	97.62	68.49	88.00	93.82	47.20	52.75	75.00	84.44	76.35	75.90
4	92.86	68.23	87.33	92.70	47.66	54.49	75.00	84.81	73.79	72.64
5	96.43	67.84	86.00	92.13	48.60	49.57	87.50	85.93	78.35	75.57

6	86.90	67.71	87.33	95.51	50.00	55.36	70.83	82.22	79.49	74.59
7	94.05	67.45	86.00	93.26	50.00	53.04	58.33	82.22	75.50	71.34
8	97.62	67.32	86.67	92.70	48.60	56.23	66.67	82.22	79.20	81.11
9	97.62	68.10	86.67	94.38	47.66	53.91	54.17	85.19	74.07	73.29
10	96.43	67.58	87.33	93.82	50.00	54.49	66.67	82.59	79.49	76.55
Average	**95.12**	**67.75**	**86.93**	**93.71**	**47.62**	**53.83**	**69.17**	**83.15**	**77.32**	**75.31**
Standard deviation	3.29	0.43	0.64	1.15	3.58	1.85	9.66	1.96	2.33	2.68

Evaluation of the results is important to know the strengths and weaknesses of the new method. During the experiment the performance of multiple NMC which constructed by the new method compared with the performance of the original NMC. The student's t-test is used to compare average of classifier accuracy before and after combined by the proposed feature partitioning algorithm. The comparison between the new multiple NMC which using this feature partitioning and the original NMC shown in Table 3 and the the Line chart of comparison of Multiple NMC and Original NMC show in Fig. 4.

Table 3. Comparison of the new multiple NMC combination and original NMC

No	Dataset	Original NMC	Multiple NMC
1	Fruit	52.26	95.12
2	Pima	63.29	67.75
3	Iris	92.67	86.93
4	Wine	72.47	93.71
5	Glass	44.72	47.62
6	liver	55.19	53.83
7	lenses	67.08	69.17
8	statlog (heart)	63.78	83.15
9	Ionosphere	70.14	77.32
10	Soybean	75.02	75.31

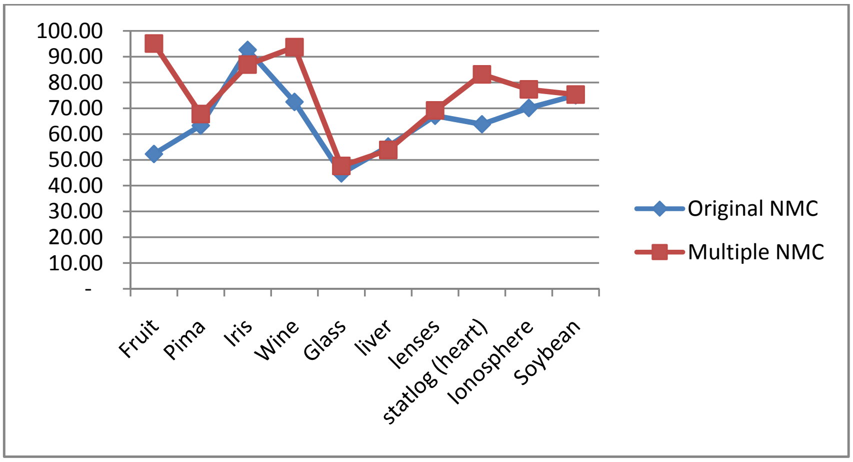

Figure 4. The line chart of comparison of multiple NMC with original NMC

Our hypothesis is NMC increased after applied the feature partitioning algorithm. In order to test this hypothesis paired sample t-test used. Paired samples had different treatment i.e. before applied feature partitioning algorithm to NMC and after applied this algorithm to NMC. One-tail t test was performed to know whether the average of the samples Multiple NMC (MNMC) larger than average of the sample NMC. Hypothesis for one-tail t test for paired two samples can be denoted :

H_o: $\boldsymbol{\mu_1} = \boldsymbol{\mu_2}$ (mean accuracy of original NMC with Multiple NMC is same)

H_1: $\boldsymbol{\mu_2} > \boldsymbol{\mu_1}$ (mean accuracy of Multiple NMC better than original NMC)

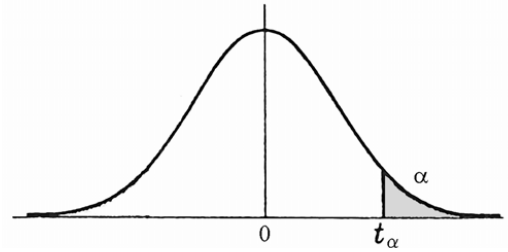

Figure 5. The student's t distribution for one-tail t-test with $\boldsymbol{H_1}$: $\boldsymbol{\mu_2} > \boldsymbol{\mu_1}$

In a one-way t-test with H_1: $\boldsymbol{\mu_2} > \boldsymbol{\mu_1}$ which called upper tail test, a series of t values on the right of the t_α boundary (the shaded region) called the critical region or rejection region (region of significance). The t values on the left of t_α called the acceptance region as shown in Fig. 5. The hypothesis was tested statistically using a paired t-test (one-tail t-test) and t*ested* at the 5% *significance level.* The results of paired sample test using SPSS are presented in Fig. 6.

T-Test

Paired Samples Statistics

		Mean	N	Std. Deviation	Std. Error Mean
Pair 1	MNC	65.6620	10	13.42646	4.24582
	MMNC	74.9910	10	15.82364	5.00387

Paired Samples Correlations

		N	Correlation	Sig.
Pair 1	MNC & MMNC	10	.514	.129

Paired Samples Test

		Paired Differences					t	df	Sig. (2-tailed)
					95% Confidence Interval of the Difference				
		Mean	Std. Deviation	Std. Error Mean	Lower	Upper			
Pair 1	MNC - MMNC	-9.32900	14.57591	4.60931	-19.75598	1.09798	-2.024	9	.074

Figure 6. The output of paired sample test using SPSS

Table "Paired Sample Statistics" indicates that the sample mean for the original NMC has a mean 65.6620 and Multiple NMC has a mean 74.99910, but whether significantly higher? According to the "Paired Samples Test", shows that two-tail probability value is 0.074. During SPSS always produce two-tailed p-value, we have to change the generated p-value to match a one-tail t-test by dividing it by 2. Thus, p-value = 0074/2 = 0.04 <0.05 (5%), thus MNMC is significantly higher in other word we reject the H_o and accept H_1 thus we can conclude that accuracy of NMC significantly increased with 95% confidence after implementation of the feature set partitioning on NMC to construct the Multiple NMC Combination.

5. Conclusion

We have presented a new algorithm for constructing disjoint feature set partitioning. The basic idea is to decompose the original set of features into several subsets, construct NMC for each projection, and then combine them. This paper examines whether the new algorithm can be useful for discovering the appropriate partitioning structure based on diversity measure. The algorithm was evaluated on several dataset. The results show that this algorithm outperforms original NMC. This experimentation leads us to conclude that the proposed algorithm can be used for creating more accurate NMC ensembles. Additional issue to be further studied is how the feature set clustering can be implemented with other classifier.

References

[1] K. Fukunaga, *Introduction to statistical pattern recognition*, 2nd ed. San Diego, CA, USA : Academic Press Professional Inc., 1990.

[2] D. Shin, and S. Kim, Nearest mean classifier via-one class SVM, *International Joint Conference on Computational Sciences and Optimization* vol. 01, pp. 593-596, 2009.

[3] C. J. Veenman, and D.M.J. Tax, A weighted nearest mean classifier for sparse subspaces, *Proceedings of Computer Vision and Pattern Recognition* vol. 2, pp. 1171-1176, 2005.

[4] A. K. Jain, and B. Chandrasekaran, *Dimensionality and sample size consideration in pattern recognition practice*, Handbook of Statistics, vol. 2, pp. 835-855, 1982.

[5] L. Rokach, Genetic algorithm-based feature set partitioning for classification problems, *Pattern Recognition*, vol. 41(5), pp. 1676-1700, 2008.

[6] D. Han, C. Han, and Y. Yang, Multiple classifiers fusion based on weighted evidence combination, *Proceedings of the IEEE International Conference on Automation and Logistics*, pp. 2138-2143, 2007.

[7] C. Y. Suen, C. Nadal, A. Mai, R. Legault, and L. Lam, Recognition of totally unconstrained handwritten numerals based on the concept of multiple experts, *Proceedings of the International Workshop on Frontiers in Handwriting Recognition*, pp. 131-143, 1990.

[8] H. Parvin, H. Alizadeh, and B.M. Bidgoli, A new method for constructing classifier ensem bles, *International Journal of Digital Content Technology and its Applications*, vol. 3(2), pp. 62-64, 2009.

[9] P. Du, H. Sun, and W. Zhang, Target identification from high resolution remote sensing image by combining multiple classifiers, *Proceedings of Multiple Classifier System*, pp. 408-417, 2009.

[10] T. K. Ho, The random subspace method for constructing decision forests. *IEEE Transactions on Pattern Analysis and Machine Intelligence*, vol. 20(8), pp. 832-844, 1998.

[11] S. D. Bay, Combining nearest neighbor classifiers through multiple feature subsets. *Proceedings of the 17th International Conference on Machine Learning*, pp. 37–45, 1998.

[12] R. Bryll, R.G. Osuna, and F. Quek, Attribute bagging: improving accuracy of classifier ensembles by using random feature subsets, *Pattern Recognition*, vol. 36, pp. 1291–1302, 2003.

[13] L-J. Wang, X-L. Wang, and Q-C. Chan, GA-Based feature subset clustering for combination of multiple nearest neighbors classifiers, *Proceedings of the 4th International Conference on Machine Learning and Cybernetics*, pp. 2982-2987, 2005.

ISSN 2163-4114 (Print)

Volume 3, Number 3
September, 2013

Information Engineering Letters

IERI Information Engineering Research Institute

DOAJ DIRECTORY OF OPEN ACCESS JOURNALS

ISSN: 2163-4114

IEL

Information Engineering Letters

Volume 3, Number 3, September, 2013

IERI INFORMATION ENGINEERING RESEARCH INSTITUTE,
USA
HTTP://WWW.IER-INSTITUTE.ORG

Information Engineering Research Institute
100 Continental Dr, Newark, DELAWARE 19713, United State, USA
http://www.ier-institute.org

ISSN: 2163-4114

List Price: $50.00

Distributed worldwide by

Information Engineering Research Institute
100 Continental Dr, Newark, DELAWARE 19713, United State, USA
E-mail: iel@ier-institute.org
Online: http://www.ier-institute.org/2163-4114.html

Volume 3, Number 3, September, 2013
Information Engineering Letters Contents

Information Engineering Letters, ISSN: **2163-4114**
Volume 3, Number 3, September, 2013

An Effective Way of Infrared Video Fatigue Detection Based on SoPC

Wang Xian-jun [a], Yuan Xiang-hui [b]

[1]Key Lab of Ministry of Education of Photoelectric Technique and System, Chongqing University, Chongqing, China

[a]wxj_cqun@sina.com, [b]yxh@cqu.edu.cn

doi.10.5729/iel.vol3.issue3.1

Keywords: SoPC, Infrared Video Fatigue Detection, PERCLOS, Difference of Gaussian Filter, Yawn, FPGA.

Abstract. A new high-speed infrared video-based fatigue detection system was developed using a system on a programmable chip (SOPC) in this study. Based on the limitations of PERCLOS, we merged the eyes and mouth fatigue related characteristics to improve detection accuracy, used a Difference of Gaussian (DoG) filter operator to detect human faces and to implement a driver fatigue detection method based on multi-feature fusion. The detection algorithm was produced using FPGA with a parallel processing structure and pipeline technology. This system is innovative and it can detect fatigued states efficiently and rapidly.

1. Introduction

Fatigue is a subjective feeling of tiredness and discomfort. However, fatigue is associated with objective effects such as a loss of activity or work capacity. Driver fatigue is one of the main causes of traffic accidents. Thus, real-time driver fatigue detection systems could have major practical benefits in detecting the states of drivers. Driver fatigue detection could elicit an alarm or alternative auxiliary driving measures if the level of fatigue reaches a certain level. Thus, such systems could increase safety greatly. Many researchers in various areas are developing systems for monitoring the physiological status and fatigue state of drivers in real-time.

Fatigue testing technology can be divided into two categories: subjective testing and objective testing. Since the development of computers and semiconductor science, practical objective testing has been the main focus. At present, driver fatigue detection devices based on PERCLOS (the abbreviations of Percentage of Eyelid Closure) are highly reliable. However, these methods have problems when the driver wears glasses or if they make head movements, so further improvements are necessary. It is generally acknowledged that people will yawn more frequently when they are tired or fatigued. The shape of the mouth when yawning differs greatly from that when it is open during a normal talking state. The opening of the mouth is much greater while yawning. In other states, the mouth is almost or completely closed. Thus, on the basis of PERCLOS method, we can analyze the state of a driver's mouth to determine their fatigue level using image processing and machine vision-based technology.

Driver fatigue detection systems must be real-time, miniaturized, non-contact, robust, lightweight, and have minimal impact on the driver. According to the requirements of PERCLOS, the system must work normally in all conditions. In this study, therefore, we developed an infrared video-based fatigue detection method using a system on a programmable chip (SOPC). Using difference of Gaussian (DoG) filter operators, the system detects the eyes and mouth characteristics, counts the number of nictations and yawns, and determines whether the driver is tired during a specific period.

At present, real-time driver fatigue detection systems are divided into two main categories: ordinary PC-based machine vision systems and video acquisition cards. The PC-based systems have advantages such as high processing speed and simplicity of development but they are not suitable for vehicle driver fatigue detection systems, mainly because of their high price, high energy consumption, large volume, and low reliability. By contrast, embedded systems are very small, expandable, and portable, so they have become a research focus for driver fatigue detection systems. In the present study, the driver fatigue detection system was designed based on FPGA and μC/OS – II. The system has the advantages of high reliability, low cost, and small volume, while it also provides a reliable platform that facilitates functional extension.

2. System implementation scheme

SOPCs are reconfigurable systems based on FPGA. The processor, memory, I/O modules, and related algorithm are integrated on the SOPC, which contains the logic functions of the entire system and it can be cut. These SOPCs have many advantages such as short data transmission link times, programming flexibility, convenience for upgrading, and a programmable hardware and software system. The data flow of our infrared video-based fatigue detection system was as follows. First, infrared radiation from an infrared focal plane array (IRFPA) is output as the infrared video data, which is pre-processed by denoising and filtering, before the image data is written to the SDRAM controller module via related modules. Second, the SDRAM controller modules perform storage and data operations. Finally, the module outputs to the display equipment and provides the appropriate failure alarm or service interruption in real-time. Fig.1 shows the overall scheme of the infrared video-based fatigue etection system.

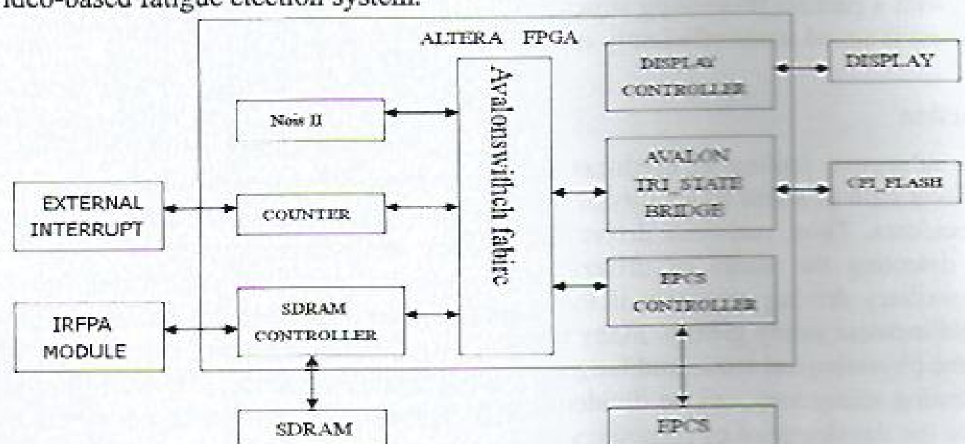

Fig.1 Overall scheme of near Infrared video-based fatigue detection system

In this system, the SOPC device uses an EP2C35F484 chip (Altera Company Cyclone II series). First, the FPGA starts the A/D module and the digital video image data from the front-end probe are input into the system, before the SDRAM controller module stores the image data in the SDRAM outside the FPGA chip. When a full frame of image data is ready, the controller produces a Nios II CPU read interrupt and the Nios II CPU reads the data from the SDRAM. Next, the CPU processes the image feature extraction algorithm in real-time. If the image features satisfy the set conditions during a specific cycle, the Nios II CPU triggers an external interrupt and runs the alarm interrupt service routine.

3. SoPC system customization and implementation

During the system design process, we loaded the Nios II core and the corresponding peripheral interface, the custom instructions, and interface, before synthesizing the design and downloading it onto FPGA chip. Finally, the hardware and software system was generated with a programmable function.

3.1 Customization of Nios II soft core processor

The NIOS II embedded processor with a Harvard structure; 32-bit instruction set is Altera Corporation's second generation on-chip programmable soft core processor. The NIOS II soft core processor has considerable flexibility, so it can be used in a variety of systems to achieve the aims of high performance, flexible features, and low cost. In this study, Uc/OS was used as the core operating system, which invoked the corresponding control interface and was connected to the SDRAM, FLASH, and display devices. Thus, the NIOS II soft core controlled the whole system.

3.2 The SDRAM controller

The SDRAM module is the core of the overall system circuit, which supports the following functions: asynchronous data processing from the interface, SDRAM memory control, image processing, and data display. It includes the five related modules shown in Table 1, which function as follows.

Table 1 Constitution of SDRAM controller module

Module name	Main function
SDRAM_FIFO	The asynchronous cache of SDRAM controller
SDRAM_SWITCH	Internal ping pong inplemention of SDRAM
DoG_IMAGE PROCESSING	DoG image edge feature extraction
LCD_TOP	LCD timing control
LCD_DISPLAY	Display image control

1) SDRAM_SWITCH: this component implements a two-bank ping-pong operation within the SDRAM bandwidth, which ensures that the input and output video streams do not have read-write conflicts. The process is shown in Fig.2.

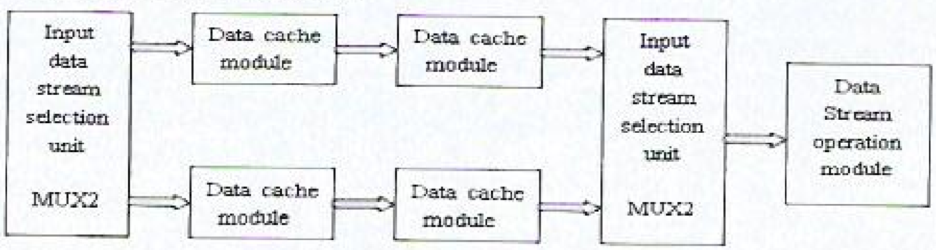

Fig.2 Flow chart of SDRAM_SWITCH

2) SDRAM_FIFO: this is the top-level module of the SDRAM controller. This component supports SDRAM initialization, SDRAM burst read and write operations, asynchronous clock domain data exchange, and synchronous communication with the VGA interface. The data flow of this module is shown in Fig.3.

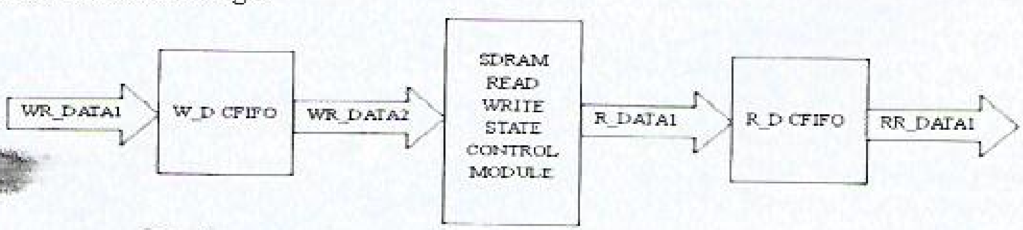

Fig.3 Flow chart of SDRAM_FIFO

3) DoG_IMAGE PROCESSING: this component is the core of the video image processing algorithm. This module supports video coding and decoding, image filtering, denoising, DoG image edge feature extraction algorithms, etc.

4)LCD_TOP: these are VGA or LCD display sequential circuits, which mainly drive the VGA or LCD.

5) LCD_DISPLAY: this is a VGA display control circuit, which mainly supports the choice of data flow, but also allows the display of subtitles, translucent operation, and other functions.

4. Fatigue detection algorithm based on the DoG

At present, the PERCLOS, as a feasible way to predict motorists driving fatigue, has been widely used. But the PERCLOS has the characteristics of oneness. It has limitations to the driver with glasses and head movements. This paper adopts a method based on Difference of Gaussian (DoG) filter. The method extract the driver's mouth state characteristics to judge whether the driver is yawning, determine whether the driver is fatigue based on yawn amount characteristics in a certain period. The flow chart is as shown in Fig.4:

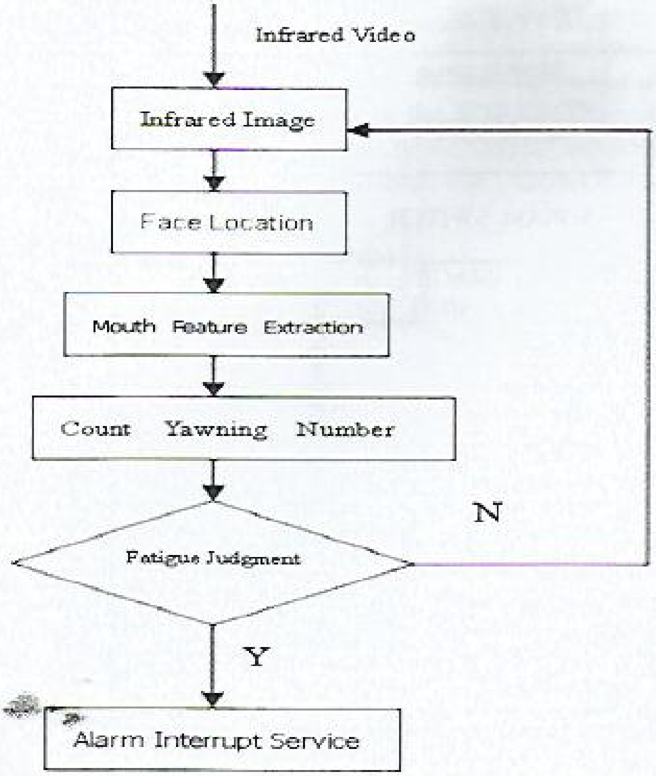

Fig.4 Flow chart of fatigue

4.1 Difference of Gaussian (DoG) filter

Edge detection is an important method of feature extraction, an important part of image recognition; image analysis.Commonly used detection operators have Prewitt operator, Sobel operator and LoG, etc. Because these operators are Difference gradient operator, they are sensitive to noise. Beacause the infrared video image is susceptible to noise interference, this paper puts forward a edge extraction algorithm based on Differenence of Gaussian filter operator.It can improve effectively reliability of the video of infrared image edge extraction and solve the problem that infrared video is susceptible to noise interference .

Differenence of Gaussian (DoG) filter is a kind of common filter in the field of computer vision and image processing. Because the filter can effectively approximate Laplacian of Gaussian (LoG) filter, thus is widely used in edge detection. It is composed of the subtraction of two different standard deviation's the Gaussian filter, its transfer function is the difference of two Gaussian functions with two different bandwidth. The equation of transfer function is as shown in Equ (1):

$$w_{DoG}[i, j]=\frac{1}{2\pi k^2\sigma^2}e^{-\frac{i^2+j^2}{2k^2\sigma^2}}-\frac{1}{2\pi\sigma^2}e^{-\frac{i^2+j^2}{2\sigma^2}} \quad (1)$$

In the Equ (1), k is the ratio of standard deviation of two filters. In this paper, we select Difference of Gaussian (DoG) filter as a band-pass filter. In the experiment, the response of the DoG is very close to the feeling of the human visual system when we choose k=1.5. So,it can effectively realize edge detection and has very good anti-interference ability.

4.2 Fatigue Judgment

After DoG operation, infrared image has been converted into mouth feature binary image. Then horizontal and vertical integral projections are respectively made in binary image. According to the horizontal and vertical integral projection image, we can accurately get width, height and horizontal position of the mouth. In order to avoid the image scale changes, a variable Opening_degree is proposed in the design to act as discriminant factor of fatigue. It is defined as a ratio of mouth width and height of the mouth surrounding area. The equation is as shown in Equ (2):

$$\text{Opening\_degree}=w/h \quad (2)$$

In Equ (2), Opening degree represents mouth openinging degree, w represents the width of the mouth surrounding area, h represents the height of the mouth surrounding area.

According to a large number of experimental data, we can assume yawn has occurred when the lasting time of Opening degree values between 0.8 and 2.0 is more than 0.5 seconds. In a certain period (The period is set to 2 minutes in the experiment) the detection system will determine the driver is in fatigue when yawn number is greater than 2. In the system, we implement the time and number count through the statistical number of video frames.

5. System test results and analysis

A near infrared video fatigue detection system is constituted based on SoPC by connecting the IRFPA, FPGA module, display equipment and alarm devices. Through joint debugging, we realize real time face edge detection, image display and fatigue detection. Fig.5 and Fig.6 are the facial features detection images which are photographed by author used mobile phone.

(a) "Talking" facial feature (b) "Yawning" facial feature (c) "Closing" facial feature

Fig.5 Three facial feature images in daytime

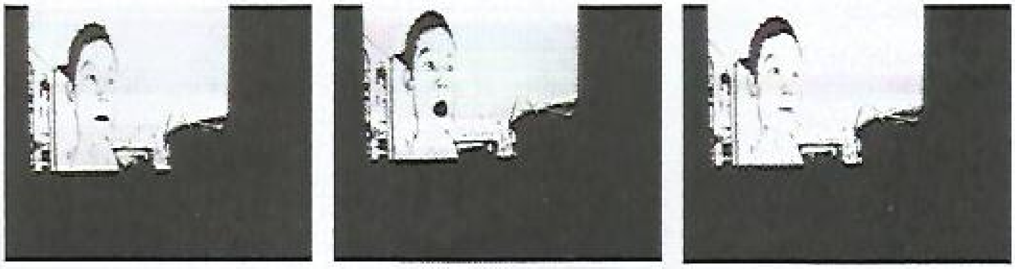

(a)

"Talking" facial feature (b) "Yawning" facial feature (c) "Closing" facial feature

Fig.6 Three facial feature images in night

FPGA has the inherent parallelism of hardware and the flexibility of the software. Its functions can be reprogrammed or reconfigured. Modern FPGA has enough resources, the whole application can be implemented on a single chip.So FPGA has become an ideal choice of embedded real-time visual system. Hardware and software are combined together in the infrared video fatigue detection system by using SoPC technology. Thus the system has characteristics of small volume, stable performance, high real-time performance and low power consumption, etc. The successful development of the system has important positive significance for the development of a practical, high-performance, real-time driver fatigue detection system.

Reference

[1] Ji. Q, Zhu. Z,W. Lan, Real-time nonintrusive monitoring and prediction of driver fatigue , IEEE Trans. Veh. Technol. 53(4), 1052–1068 (2004).

[2] Anneke H, Rainer G, Acacia A, Technologies for the Monitoring and Prevention of Driver Fatigue, Proceedings of the First International Driving Symposium on Human Factors in Driver , Training and Vehicle Design, 81-86, 2001.

[3] Damez, Lionel,Sieler, Loic, Landrault, Alexis, Dérutin, Jean Pierre, Embedding of a real time image stabilization algorithm on a parameterizable SoPC architecture a chip multi-processor approach, Journal of Real-Time Image Processing, v 6, n 1, p 47-58, 2011.

Information Engineering Letters, ISSN: **2163-4114**
Volume **3**, Number **3**, September, **2013**

Harvest Pulse-likeFootstep Energy on Pavement

Longhan Xie [a] and Mingjing Cai [b]
South China University of Technology, Guangzhou, China
[a]melhxie@scut.edu.cn, [b]calls.cai@163.com

doi.10.5729/iel.vol3.issue3.7

Keywords: Energy harvesting, Footstep motion, Electromagnetic conversion.

Abstract. In recent years great efforts have been made to reduce carbon emissions and power small electronic devices, for example sensor networks, without the need of batteries.It is known that human footstep contains rich mechanical energy which can be utilized. In this paper, an energy harvester for harnessing energy from human foot strike is developed, which uses spring-slider-crank mechanism to absorb footstep motion and gear train to accelerate the mechanical rotation. Electromagnetic conversion mechanism is developed to convert mechanical energy into electricity which is also rectified into DC voltage through rectifying circuit. A prototype was set up to validate the harvester. Experiments show that the harvester can harvest about 2 Watts under 1 Hz frequency of foot strike on the harvester.

1. Introduction

In recent years great efforts have been made to reduce carbon emissions and power small electronic devices, for example sensor networks, without the need of batteries. Therefore the energy forthose devices should be scavenged from environment. In this investigation, people's footstep can be utilized to convert some of kinetic energy from human body into electricity to power the sensor network or emergent lights.

Human walking is a main energy consumption activity which also has mechanical power to be exploited. It has been calculated that up to 67 Watts of power are available from heel strike during normal walking for a 68 kg person with the walking frequency at 2 step per second and heel moving 5 cm[1]. There are mainly twomethods to harvest the foot strike energy during human walking [2-4]. One is to use piezoelectric effect to convert the pressure generated when the foot strikes the ground to electricity[2]. Unfortunately, the energy density is very low (only 8.3mW at the heel and 1.3 mW at the toe). Another is to us electromagnetic induction to convert body motion to electricity. Chen [6] and Lakic [7] reported electromechanical generators to convert the foot step motion. However these designs are very complex with many parts, and can only harvest the press-down motion, which make these device is fragile, expensive and lower efficiency.

This paper is focused on how to harvest the mechanical energy from human foot strike on the energy harvester. Compared to the existing designs, the proposed harvesting apparatus in this paper will be simpler and stronger, and can harvest not only press-down motion but also the release-up motion. The rest of this paper is organized as follows. Section 2illustrates the design of the harvester. Section 3 will analyzes the performance of the harvester. Section 4 will give the estimation of the power output. Section 5 gives the experiment results, and section 6 contains the conclusions.

2. Design of the Harvester

The CAD model of the harvester is shown in Fig.1. The harvester mainly includes a fixed part and a moving part, where the moving part can glide relative to the fixed part guided by guiding poles. The springs around the guiding poles provide the rebound force. The harvester adopts the crank slider mechanism to transmit the motion of the moving board from foot strike to the gear train, and then the rotation motion is sped up via the gear train and finallyto the electromagnetic conversion mechanism. As shown in Fig.2(a), the moving board can drive two sets of slider-crank mechanisms, one of which can drive two set of gear train to accelerate the rotation and then run totally 16 sets of electromagnetic conversion mechanism to produce electricity.

Fig.2(b) shows the detail crank slider mechanism, where one end of the crank coupler is pinned to the moving board, and the other end is pinned to the crank wheel. In this mechanism, the moving board serves as the slider which is the driven motion, and the crank transmit the rotation to gear train. Fig.2(c) is the close view of the gear train mechanism.All the transmission parts are assembled in the gear box. There are four identical transmission mechanisms, each of which consists of driven gear, intermediate gear and pinion. All the gears are supported by shafts, which are fixed on the base through bearings. The fixed base and middle cover are screwed together to hold bearings.

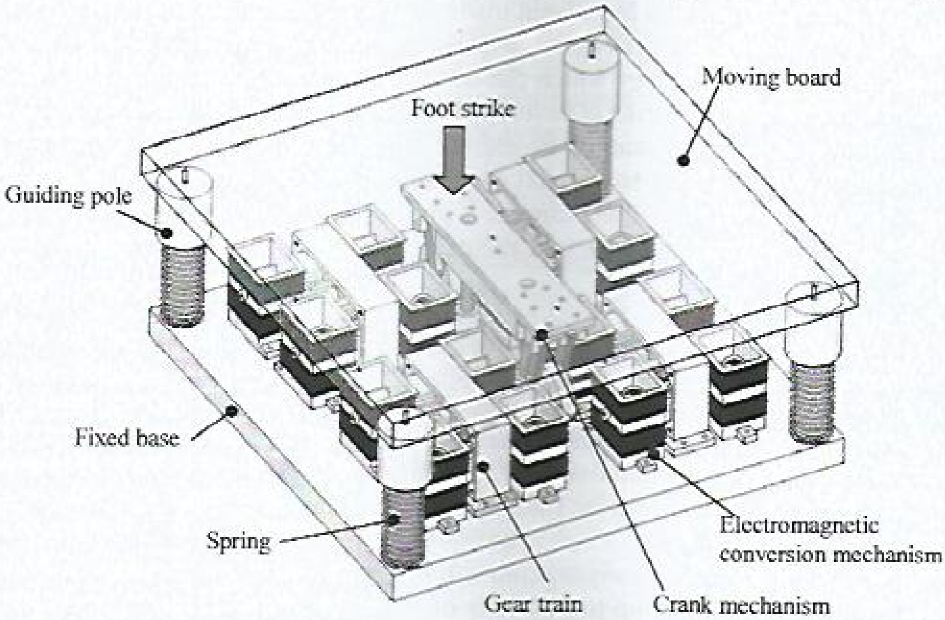

Fig.1: the CAD model of the harvester

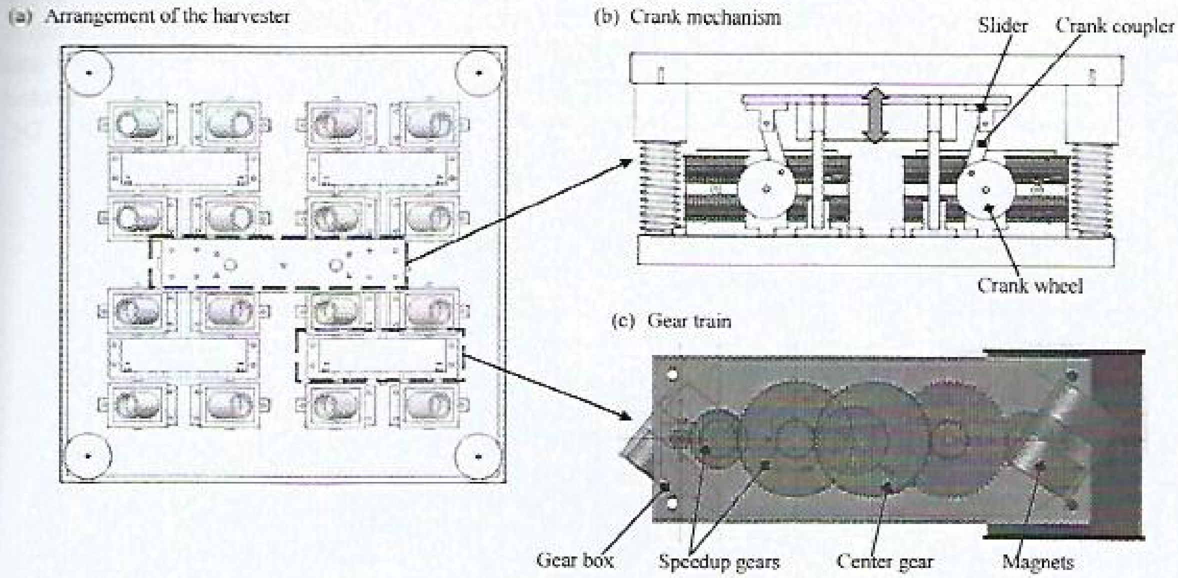

Fig.2: Detail structure of the harvester

The mechanical energy is converted into electricity through electromagnetic conversion mechanism. As shown in Fig.3, the high-speed rotation from gear train finally drives the permanent magnets, which are assembled in the magnet holder, to produce changing magnetic field. Electric coils are wounded around the coil holder, where electricity is generated due the changing magnetic field.

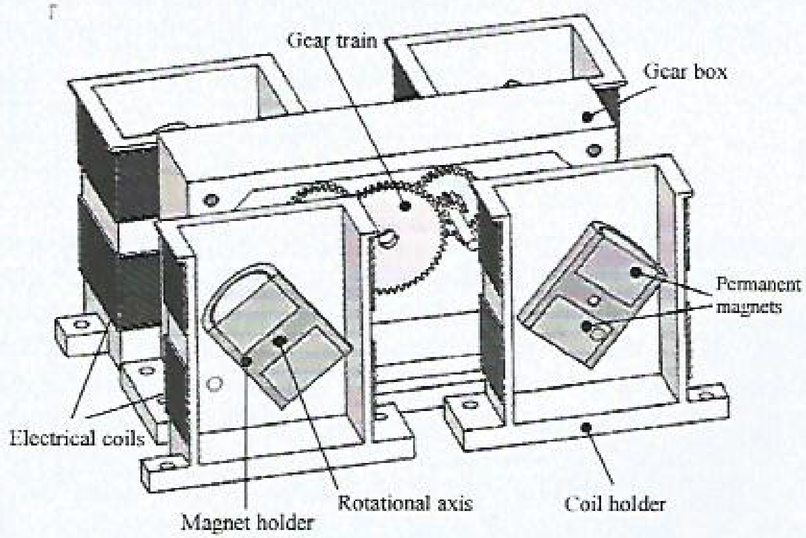

Fig.3: Details of the electromagnetic conversion mechanism

Generally speaking, the harvester adopts spring-crank-slider mechanism, gear train and electromagnetic conversion mechanism to harness pulse-like footstep motion. Fig.4 shows the schematic diagram of the harvester. First of all, the foot strike motion is up and down linear motion and the generator can only receive rotation, so the device uses a crank-slider mechanism to convert the linear motion into rotational one, which includes a slider, gear as the crank and their pin-jointed crank coupler. Secondly, in order to continuously drive the harvesting device, a recovery mechanism for the slider is needed. In this design, a spring, constrained around a cylinder pole, is used to provide the recovery function for continuous motion. When foot touches the harvester, the spring is pressed down; and the spring is released up when the foot pushes off the moving board of the harvester.

Thereforeduring the foot touches and releases the ground, springs provide reciprocating motion for the harvester. Usually the step frequency is low but the driving force is large enough, so a gear train is used to speed up the rotation. From the physical model, there are four transmission sets and generators, which share the same slider-spring mechanism and control circuit. Electricity generated by all electromagnetic conversion mechanism is connected to a control circuit to rectify into DC electricity and store in battery for use.

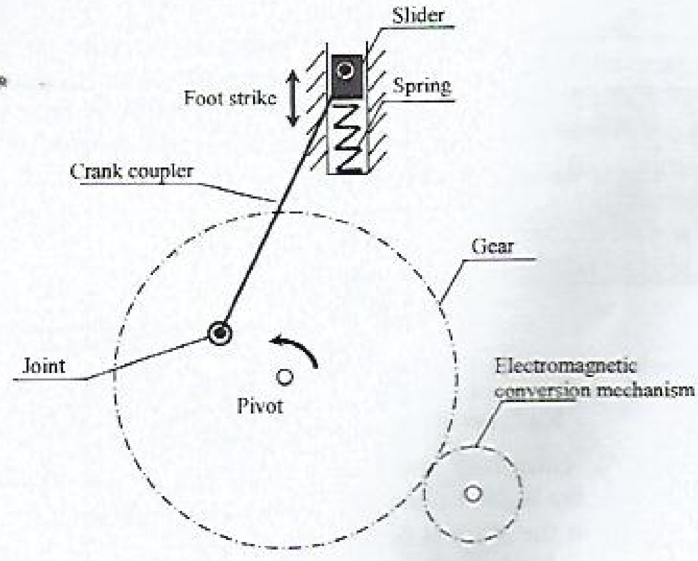

Fig.4: The schematic diagram of the harvester

3.Theoretical Analysis

Crank-slider mechanism is the most critical mechanism in this harvesting device. Extracted from the physical model, Fig.5 shows the schematic diagram of the offset crank-slider linkage, where the grounded pivot O of the crank does not lie on an extension of the line along which the pivot B is pin-jointed to slider. For a given set of linkage dimensions L_1, L_2, the offset distance L_0, and displacement of slider L_3, the following equations can be obtained by geometric and trigonometric relations. If the dimensions L_0, L_1 and L_2 are known, and the slider displacement L_3 is known too, then the angular displacement of the crank can be solved by these two equations.

$$L_1 \cos\theta_1 + L_2 \cos\theta_2 = L_3 \tag{1}$$

$$L_0 + L_1 \sin\theta_1 + L_2 \sin\theta_2 = 0 \tag{2}$$

For the offset crank slider mechanism, if the slider moves with constant velocity v_B from upper extreme point B^1 to lower extreme point B^2, then the crank rotates from position A^1 to position A^2 with the angle $\angle A^1OA^2 = \pi - \alpha$, however it will rotates with the angle $\angle A^2OA^1 = \pi + \alpha$ when the slider moves from B^2 to B^1. If both of time elapsed Δt are same, then the angular velocity of crank is different, which can be deduced from the following equation. Thus there is velocity fluctuation between the up stroke and the down stroke, which is not good to the generator. From the Fig.6, the angle α is related to the offset distance L_0, that is, the bigger offset distance L_0, the greater angle α under the condition that other variables are constant. Therefore, it is best to set the offset distance zero, *i.e.* in-line crank-slider mechanism.

$$TR = \frac{\omega_1}{\omega_2} = \frac{\angle A^1OA^2 / \Delta t}{\angle A^2OA^1 / \Delta t} = \frac{\pi - \alpha}{\pi + \alpha} \tag{3}$$

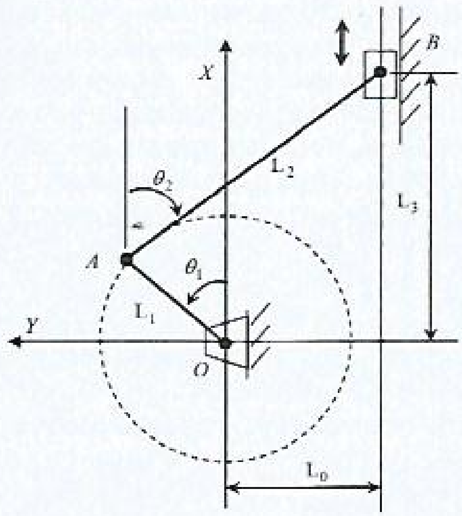

Fig.5: Offset crank-slider mechanism

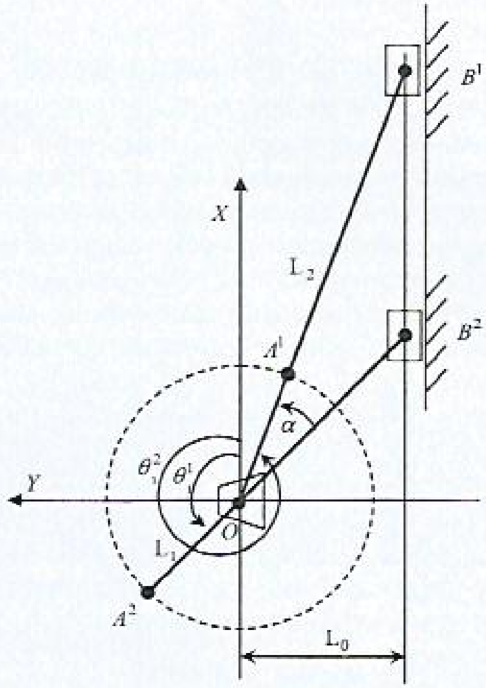

Fig.6: Extreme positions in offset crank slider linkage

For crank slider linkage, there is two deadlock points in the crank's cycle: one is at point A^1 where the angle between the crank and the crank coupler is 180°, and the other is at point A^2 where the angle is 0°. In order to avoid the deadlock problem, a "disturbed weight" is added to one end of the crank, as shown in Fig.7. For the initial conditionwhen the slider is pressed due to the heel strike, *i.e.* the linkage lies as Fig.7, there is a disturbed force from the disturbed weight because there is acceleration from the heel strike. Therefore, the crank can be driven even if the linkage lies at deadlock point. When the pressed spring is released and slider moves upwards, the linkage lies at the second deadlock point A^2. Because the gear train is rotating and the rotating inertia of moment from the disturbed weight, the linkage can easily pass this deadlock point.

There are four springs in the harvester, and assume that the total spring constant is $K = 4k_1$, where k_1 is the stiffness constant of each spring. If the spring has the deflection ΔS, then the spring force can be expressed as following according to the Hooke's Law.

$$f_s = K \cdot \Delta S \tag{4}$$

Usually the foot strike on the foot is about 1.5 times body weight. To relieve the strike on the foot, the harvester can be designed to absorb part of the body weight, *i.e.*:

$$f_s = K \cdot \Delta S = \beta \cdot mg \tag{5}$$

Where β is the absorption factor for the harvester, and m is the body weight. And the total spring deflection should be equal to the maximum displacement of the slider, *i.e.* $\Delta S = 2L_1$. Therefore, the total spring constant should be satisfactory with the following equation.

$$K = \frac{\beta \cdot mg}{2L_1} \tag{6}$$

If the slider position when all springs are in release is $x_B = 0$, and the position when springs are fully pressed down is $x_B = 2L_1$, then the deflection range of springs should be greater than $[0, 2L_1]$, *i.e.* when maximum deflection length of all springs should be greater than $2L_1$ so that the slider can move up and down at full range. When the slider, *i.e.* the moving board, is fully pressed down, the whole body weight and the impact force are all loaded onto the transmission components of the harvester, which is harmful to the harvester, some action should be taken to avoid such damage. If the lowest position of the slider is the point when springs are extremely pressed down, i.e. when spring wires are attached together, the springs can support most of the body weight. And the slider should be able to restore to the highest position, when there is not any other restoring force but the spring force, so at the highest slider position the springs are also pressed slightly to provide thrust to restore the slider.

The most popular calculating formula of helical springs with circular cross-sectional wire is given as following.

$$k = \frac{G \cdot d^4}{8n \cdot D^3} \tag{7}$$

Where, G is the shear modulus; d is the wire diameter, n is the effective number of coils; D is the mean coil diameter. Therefore, with Eqs.(6) and (7), given an absorption factor, the dimensions of springs can be determined.

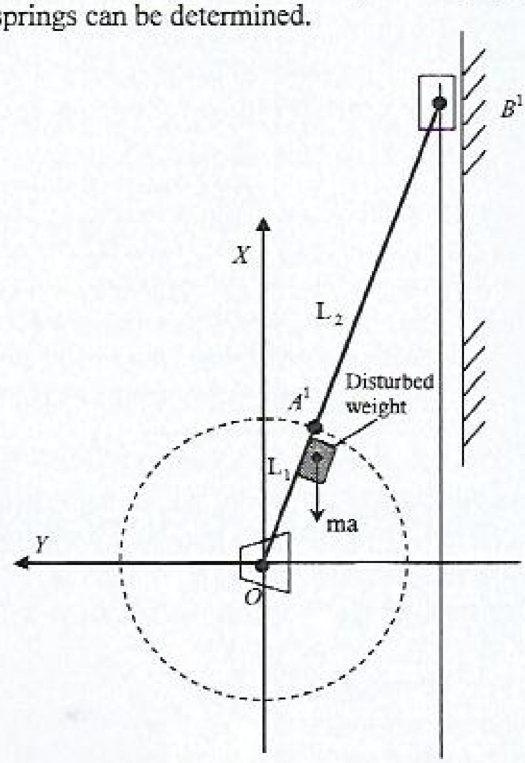

Fig.7: Solution for deadlock

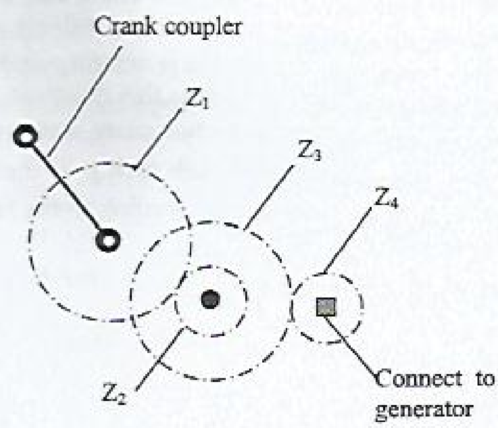

Fig.8: The gear train for each generator

4. Power Output Estimation

The harvester employs a set of gear train for each AC generator to speed up the rotation from the crank-slider mechanism, schematically shown in Fig.8. There are two gear pairs in the harvester, both of which are for acceleration. The total amplification ratio of the gear train can be expressed as following, where $Z_i, i=1,2,3,4$ is the tooth number for each gear. In this harvester, two gear pairs have the same gear ratio, *i.e.* $Z_1/Z_2 = Z_3/Z_4 = 20$, then the total amplification ratio is 400, which can greatly boost the rotation speed.

$$GR = \frac{Z_1}{Z_2} \cdot \frac{Z_3}{Z_4} \tag{8}$$

To estimate the power output, we can approximately use the work of springs to calculate the total input work W_{in} in a single period, as following, where K is the total spring constant, and $2L_1$ is the slider stroke distance.

$$W_{in} = 2 \cdot \frac{1}{2} K \cdot (2L_1)^2 = 4KL_1^2 \tag{9}$$

Considering the energy loss in transmission, including the crank-slider mechanism and gear train, and energy loss in mechanical-electrical conversion through the generator and electric circuit, which two efficiency factors are assumed as η_m and η_e, respectively, then the total output energy can be expressed as following.

$$E_{out} = 4\eta_m \eta_e K L_1^2 \tag{10}$$

Let the footstep frequency is f, then because every 2 steps has once heel strike, i.e. the working period of the harvester is two times that of footstep. So the average power output can be calculated by the following expression.

$$\overline{P}_{out} = \frac{E_{out}}{2T} = 2f \cdot \eta_m \eta_e \cdot K L_1^2 \tag{11}$$

The mechanical efficiency and electrical conversion efficiency of such kind of harvester are estimated to be 90% and 70%, respectively. Let the absorption factor for the harvester is $\beta = 0.5$, and there is 2 steps per second on the harvester, then the input energy for each step is 6J by Eq.(9). And the average power output can be calculated by Eqs.(5) and (11). The estimated average power output is about 2 watts for the harvester with the slider stroke length 10mm. The electricity generated by all electric coils is rectified by the circuit as shown in Fig.9.

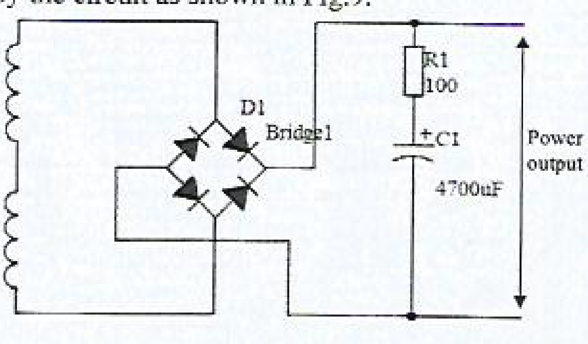

Fig.9: the rectifying circuit

5. Experiments

A prototype of the above-discussed harvester was made to validate the performance of harvesting human footstep kinetic energy on pavement. As shown in Fig.10, according to the CAD model in Fig.1, the prototype is 40cmX40cm and includes eleven sets of electromagnetic conversion mechanism and a rectifying circuit.

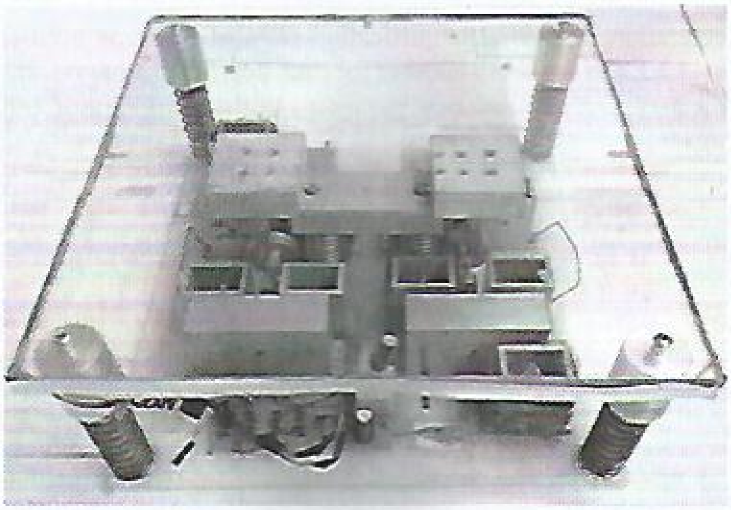

Fig.10: Prototype of the harvester

During testing, all generators are connected in parallel to the rectifying circuit, and an external resistance is used as load which voltage is measured by anUTD2052CLoscillograph. The external resistance is 3Ω, which is equal the internal resistance of all generators in parallel. The test duration is 60 seconds, during which the number of foot strikes on the harvester are counts.Table 1 shows the testing data, where the average power output is calculated according the voltage on the external resistance. Fig.11 shows the average power output with respect to number of foot strike during one minute. From the testing data, the power output increases when the frequency of foot strikes speeds up.

Tab. 1: testing data

No. of Foot Strikes	Voltage（V）	Average Power（W）
55	2.19	1.60
56	2.21	1.63
57	2.27	1.72
58	2.26	1.70
59	2.28	1.73
60	2.30	1.76
61	2.31	1.78
62	2.35	1.84
63	2.37	1.87
64	2.40	1.92
65	2.41	1.94

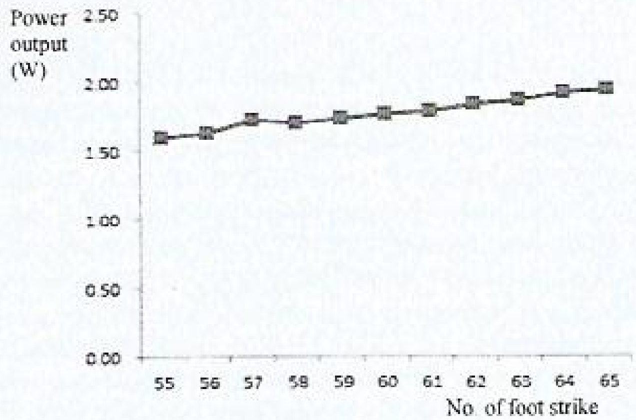

Fig.11: Average power output

6. Conclusions

Base on the above discussions, the following conclusions can be made.

(1) An energy harvester is developed to harness footstep motion by using a slider crank mechanism, which is more effective to collect footstep mechanical energy.

(2) The slider crank mechanism was analyzed and optimized, which gives the optimized parameters for prototype manufacturing.

(3) A prototype was set up to test the harvester. Experiments show that the harvester can produce around 2 watts of power under 1 Hz frequency of foot strike on the harvester.

Acknowledgements

This work is supported by the Fundamental Research Funds for the Central Universities (Grant No. 2012ZP00008), and National Natural Science Foundation of China(Grant No. 51105146).

References

[1] T. Starner and J.Paradiso. Low-Power Electronics Design, Chapter 45, CRC Press, New York, 2004.

[2] N.Shenck, J.Paradiso. Energy Scavenging with shoe-mounted pizoelectrics, IEEE Micro, Vol. 21(3), pp30-42, 2001.

[3] R.D.Kornbluh.Electroelastomers: applications of dielectric elastomer transducers for actuation, generation, and smart structures, Smart Structures and Materials 2002: Industrial and Commercial Applications of Smart Structures Technologies, vol.4698, pp.254-270, 2002.

[4] L.Rome. Generating electricity while walking with loads, Science, Vol. 309, pp.1725-1728, 2005.

[5] J.Donelan. Biomechanical energy harvesting: generating electricity during walking with minimal user effort, Science, Vol.319, pp.807-810, 2008.

[6] S. H.Chen. Dynamoelectric shoes, US Patent No.5495682, 1996.

[7] N.Lakic. Inflatable boot liner with electrical generator and heater, US Patent No.4845338, 1989.

Information Engineering Letters, ISSN: 2163-4114
Volume 3, Number 3, September, 2013

Diversity-based Feature Partitioning for Combination of Nearest Mean Classifier

Abdullah

Dept. of Information System, Universitas Islam Indragiri, Tembilahan 29200, Indonesia

abdialam@yahoo.com

doi.10.5729/iel.vol3.issue3.16

Keywords: Nearest mean classifier, Feature partitioning, Multiple classifier combination

Abstract. Nearest Mean Classifier (NMC) provides good performance for small sample training. However concatenate different features into a high dimensional feature vectors and process them using a single NMC generally does not give good results because dimensionality problem. Most methods used to address the dimensionality problem focuses on feature selection method, choosing a single feature subset, while ignoring the rest. Although there are several algorithms have been proposed, but there are drawbacks to using of feature selection method. The assumption that a large set of input features can be reduced to a small subset of relevant features is not always true. In some cases the target feature is actually affected by most of the input features and removing features will cause a significant loss of important information. Thus, the classifier may achieve a lower level of accuracy than the classifiers that accesses all the relevant features. In this method the feature set clusters into different feature subset. NMC ensembles constructed by assigning each individual classifier in the ensemble with a cluster of different feature subset. The advantage of this approach is that all of available information in the training set is used. There is no irrelevant feature in the training set are eliminated. Based on experimental results the new technique significantly improve the nearest mean classifier (NMC) with 95% confidence.

1. Introduction

Nearest mean classifier (NMC) was introduced by Fukunaga [1] as a classifier which uses the similarity between patterns to determine the classification. For each class, NMC computes the class mean (or centroid) of the training patterns. Similarity values obtained by calculate the Euclidean distance between the test patterns to the class mean of the training patterns. NMC classifies any test patterns (or unknown objects) to the class whose the class mean is closest to this test patterns. NMC has been successfully applied to many classification problems and showed good performance and very strong [2]. Furthermore NMC provides good performance for small training sample problem [3]. Small training sample problems are problems with the number of samples is much smaller than the number of features [4]. However concatenate different features into a high dimensional feature vectors and process them using a single NMC generally does not give good results because dimensionality problem. Most methods used to address the dimensionality problem focuses on feature selection method, choosing a single feature subset, while ignoring the rest. Although there are several algorithms have been proposed, but there are drawbacks to using of feature selection method. The assumption that a large set of input features can be reduced to a small subset of relevant features is not always true. In some cases the target feature is actually affected by most of the input features and removing features will cause a significant loss of important information. Thus, the classifier may achieve a lower level of accuracy than the classifiers that accesses all the relevant features [5].

Multiple classifier combination aims to obtain the final classification decision by integrating the output of several individual classifier [6]. The concept of multiple classifier system was first proposed by Suen et al. [7] in order to improve the results of character recognition. In the literature, this research area is defined by a number of different names, such as multiple classifier combination, combining classifiers, classifier ensembles, committees of learner, mixtures of experts, the consensus theory, hybrid methods, decision combination, multiple experts, cooperative agents, opinion pool, sensor fusion [8]. Regardless of the different names that have been defined, the multiple classifier system combine several classifiers to obtain the final classification result. Currently. Combining multiple classifier is considered as a new direction for pattern recognition. Multiple classifier system has been shown to be very helpful in improving the classification performance over single classifier approach [9].

One of approach that used to construct a diverse classifier ensemble is the manipulation of input features. This approach assigns different subset of features among individual classifier in the ensemble (usually, the same base classifier used). The main method of this approach is the random subspace method [10] which assigns a random subset of the original features to individual classifier (on the same training sample). Feature subsets can overlap, and their sizes are usually identical. Other methods that have similar idea with this method is the multiple feature subsets [11] and the attributes bagging [12]. All of these methods are similar in the way they assign features randomly to individual classifier in the ensemble. The differences are in the determination of subset and ensemble size. A new method that uses this approach is the feature subset partitioning. In this method the feature set clusters into different feature subset. Ensemble constructed by assigning each individual classifier in the ensemble with a cluster of different feature subset from the pool of available features. The advantage of this approach is that all available information in the training set is used. There is no irrelevant feature in the training set are eliminated. Irrelevant feature does not need to be eliminated in the combination of classifier, because this omitted feature may contain valuable information [13].

2. Proposed Method

In this method, a group of classifier built from the training data. Based on the original training data a disjoint feature subset decomposition was performed. Ensemble classifier is built based on the feature subset partition. Prediction class label of unknown pattern obtained by aggregating predictions using a combiner. Fig. 1 shows the general idea of this method.

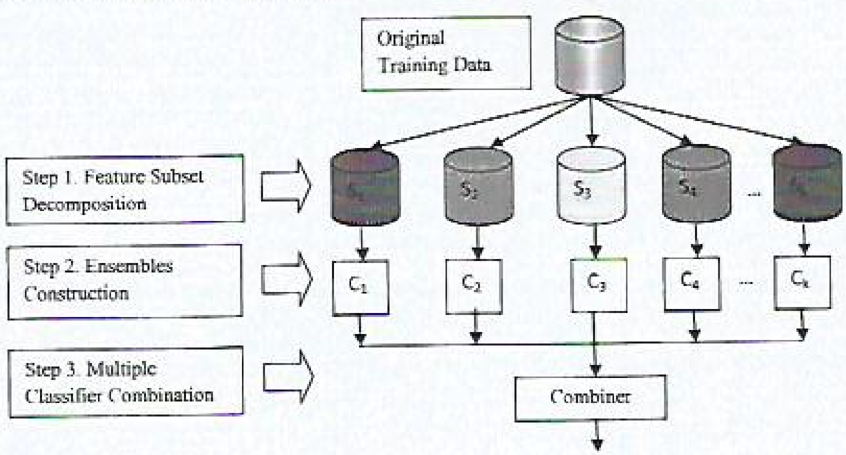

Figure 1. General idea of diversity-based feature clustering for classifier combination

Based on this idea an algorithm constructed to perform feature subset decomposition. Furthermore NMC ensemble constructed by projection of the feature subset of original training data. The pseudocode for this algorithm is as follows:

Input: The n features training set and the class labels

process:

1. Make two subset of features that provides the greatest diversity
2. Choose any of the remaining features
3. Create possible features partition
4. Select the feature partition that provides maximum diversity measure
5. Go to step 2 until all of features have been partitioned
6. Use the feature partition to construct NMC ensemble

Output: a classifier ensemble C *

Input training set and class labels are required inputs. The next step was built two feature subset that gives the maximum value of diversity in the ensemble. Diversity is measured based on support diversity measure which is more frequently an agreement among the individual NMC provides small value diversity. Furthermore disjoint feature set partitioning for all feature in such a way that provides maximum diversity in the NMC ensembles. The last step the feature subset used to construct NMC ensembles. Overall the steps as shown in Fig. 2.

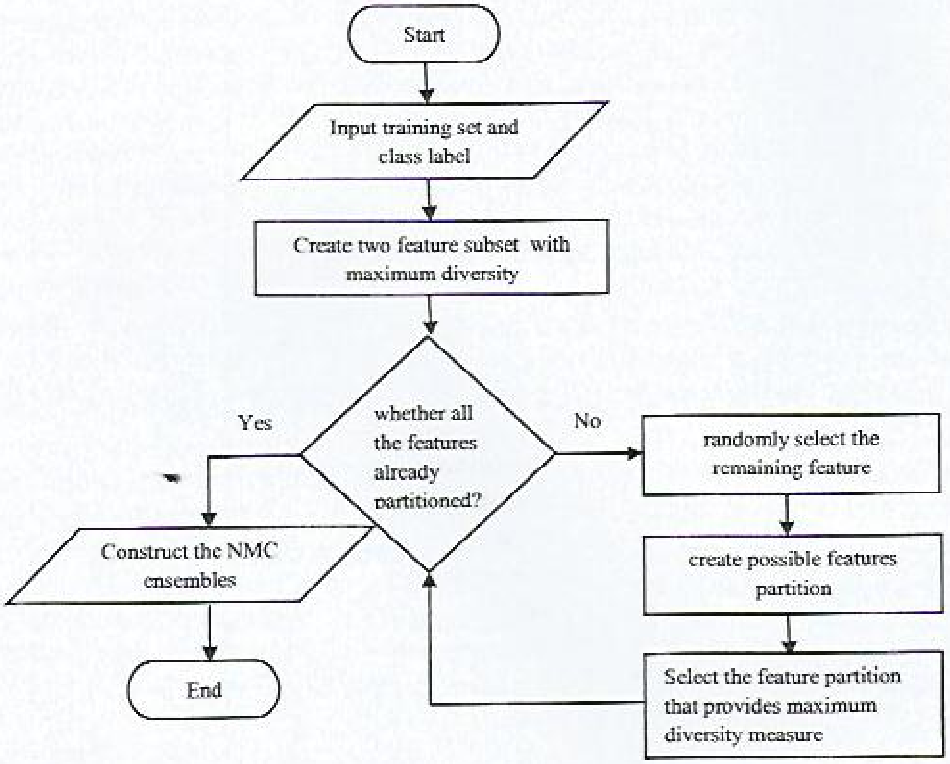

Figure 2. The flowchart of diversity-based feature clustering algorithm for NMC

3. Research Methodology

In order to evaluate the performance of this method hence multiple NMC combination constructed to test its ability to perform classification task. The method of research as follows: (1) NMC ensembles is designed using this new algorithm. (2) Applied the multiple NMC combination for classification task (3) Classification experiments using NMC combination performed using several datasets. (4) The results which obtained evaluated by compare this NMC combination with the original NMC. The steps of the research can be seen in Fig. 3.

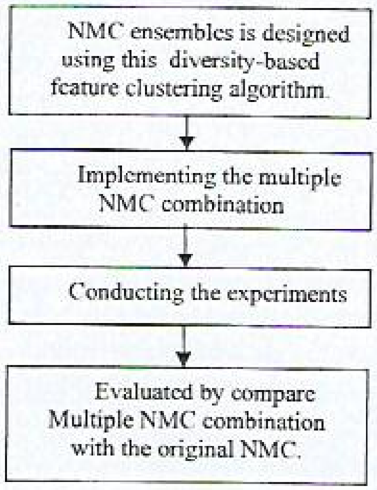

Figure 3. The steps of the research

4. Experiment Results

The results of individual nearest mean classifier accuracy using several datasets are presented in Table 1.

Table 1. The accuracy of individual nearest mean classifier

# Experiment	Fruit	Pima	Iris	Wine	Glass	Liver	Lenses	Statlog (heart)	Ionosphere	Soybean
1	53.57	63.02	92.00	71.91	45.79	55.07	66.67	64.44	69.23	75.24
2	52.38	62.89	91.33	72.47	44.86	55.94	70.83	62.96	69.80	74.59
3	50.00	63.41	92.67	72.47	45.33	54.20	62.50	62.22	70.66	75.90
4	53.57	63.15	92.67	72.47	43.93	54.49	70.83	64.07	71.79	75.24
5	53.57	63.67	92.00	72.47	44.39	53.91	58.33	64.44	70.09	74.59
6	52.38	62.89	92.00	72.47	44.86	56.23	66.67	64.07	68.66	75.57
7	48.81	63.41	92.67	73.03	44.39	55.94	75.00	63.70	69.80	76.22
8	52.38	63.28	92.00	73.03	44.86	55.36	54.17	64.07	70.37	75.24
9	54.76	63.67	91.33	71.35	45.33	55.07	75.00	63.70	70.09	73.94
10	51.19	63.54	92.00	73.03	43.46	55.65	70.83	64.07	70.94	73.62
Average	**52.26**	**63.29**	**92.67**	**72.47**	**44.72**	**55.19**	**67.08**	**63.78**	**70.14**	**75.02**
Standard deviation	1.81	0.30	0.49	0.53	0.70	0.79	6.93	0.69	0.88	0.83

The experiment results of multiple nearest mean classifier accuracy using the diversity based feature partitioning algorithm using several datasets are presented in Table 2.

Table 2. The accuracy of multiple nearest mean classifier combination

# Experiment	Fruit	Pima	Iris	Wine	Glass	Liver	Lenses	Statlog (heart)	Ionosphere	Soybean
1	95.24	67.06	87.33	95.51	37.85	53.33	75.00	79.26	80.06	75.57
2	96.43	67.71	86.67	93.26	48.60	55.07	62.50	82.59	76.92	76.55
3	97.62	68.49	88.00	93.82	47.20	52.75	75.00	84.44	76.35	75.90
4	92.86	68.23	87.33	92.70	47.66	54.49	75.00	84.81	73.79	72.64
5	96.43	67.84	86.00	92.13	48.60	49.57	87.50	85.93	78.35	75.57

6	86.90	67.71	87.33	95.51	50.00	55.36	70.83	82.22	79.49	74.59
7	94.05	67.45	86.00	93.26	50.00	53.04	58.33	82.22	75.50	71.34
8	97.62	67.32	86.67	92.70	48.60	56.23	66.67	82.22	79.20	81.11
9	97.62	68.10	86.67	94.38	47.66	53.91	54.17	85.19	74.07	73.29
10	96.43	67.58	87.33	93.82	50.00	54.49	66.67	82.59	79.49	76.55
Average	**95.12**	**67.75**	**86.93**	**93.71**	**47.62**	**53.83**	**69.17**	**83.15**	**77.32**	**75.31**
Standard deviation	3.29	0.43	0.64	1.15	3.58	1.85	9.66	1.96	2.33	2.68

Evaluation of the results is important to know the strengths and weaknesses of the new method. During the experiment the performance of multiple NMC which constructed by the new method compared with the performance of the original NMC. The student's t-test is used to compare average of classifier accuracy before and after combined by the proposed feature partitioning algorithm. The comparison between the new multiple NMC which using this feature partitioning and the original NMC shown in Table 3 and the the Line chart of comparison of Multiple NMC and Original NMC show in Fig. 4.

Table 3. Comparison of the new multiple NMC combination and original NMC

No	Dataset	Original NMC	Multiple NMC
1	Fruit	52.26	95.12
2	Pima	63.29	67.75
3	Iris	92.67	86.93
4	Wine	72.47	93.71
5	Glass	44.72	47.62
6	liver	55.19	53.83
7	lenses	67.08	69.17
8	statlog (heart)	63.78	83.15
9	Ionosphere	70.14	77.32
10	Soybean	75.02	75.31

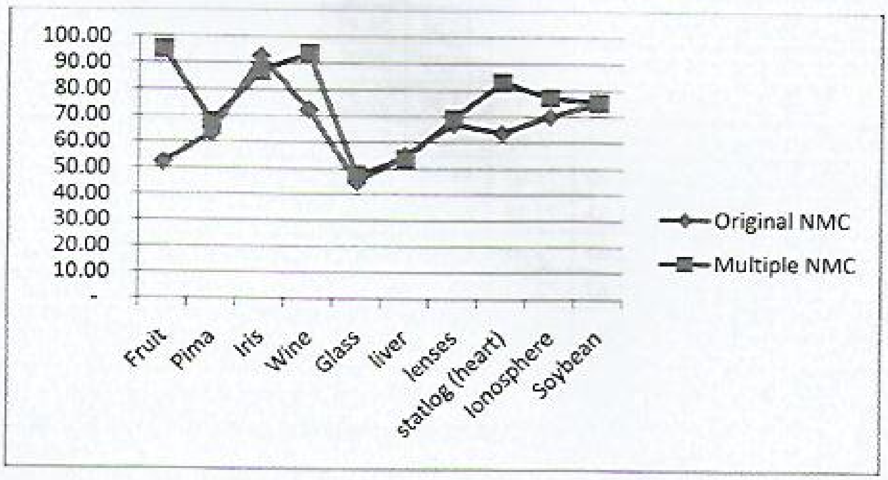

Figure 4. The line chart of comparison of multiple NMC with original NMC

Our hypothesis is NMC increased after applied the feature partitioning algorithm. In order to test this hypothesis paired sample t-test used. Paired samples had different treatment i.e. before applied feature partitioning algorithm to NMC and after applied this algorithm to NMC. One-tail t test was performed to know whether the average of the samples Multiple NMC (MNMC) larger than average of the sample NMC. Hypothesis for one-tail t test for paired two samples can be denoted :

$H_o\colon \boldsymbol{\mu_1} = \boldsymbol{\mu_2}$ (mean accuracy of original NMC with Multiple NMC is same)

H_1: $\mu_2 > \mu_1$ (mean accuracy of Multiple NMC better than original NMC)

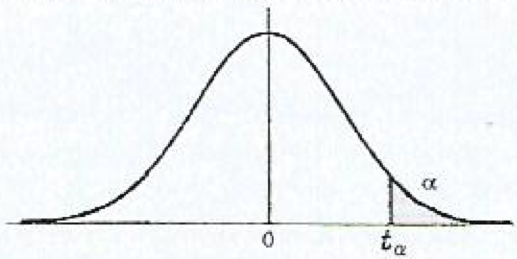

Figure 5. The student's t distribution for one-tail t-test with $H_1: \mu_2 > \mu_1$

In a one-way t-test with $H_1: \mu_2 > \mu_1$ which called upper tail test, a series of t values on the right of the t_α boundary (the shaded region) called the critical region or rejection region (region of significance). The t values on the left of t_α called the acceptance region as shown in Fig. 5. The hypothesis was tested statistically using a paired t-test (one-tail t-test) and *tested* at the *5% significance level.* The results of paired sample test using SPSS are presented in Fig. 6.

T-Test

Paired Samples Statistics

		Mean	N	Std. Deviation	Std. Error Mean
Pair 1	MNC	65.6620	10	13.42545	4.24582
	MMNC	74.9910	10	15.82364	5.00387

Paired Samples Correlations

		N	Correlation	Sig.
Pair 1	MNC & MMNC	10	.514	.129

Paired Samples Test

		Paired Differences					t	df	Sig. (2-tailed)
					95% Confidence Interval of the Difference				
		Mean	Std. Deviation	Std. Error Mean	Lower	Upper			
Pair 1	MNC - MMNC	-9.32900	14.57591	4.60931	-19.75598	1.09798	-2.024	9	.074

Figure 6. The output of paired sample test using SPSS

Table "Paired Sample Statistics" indicates that the sample mean for the original NMC has a mean 65.6620 and Multiple NMC has a mean 74.99910, but whether significantly higher? According to the "Paired Samples Test", shows that two-tail probability value is 0.074. During SPSS always produce two-tailed p-value, we have to change the generated p-value to match a one-tail t-test by dividing it by 2. Thus, p-value = 0074/2 = 0.04 <0.05 (5%), thus MNMC is significantly higher in other word we reject the H_o and accept H_1 thus we can conclude that accuracy of NMC significantly increased with 95% confidence after implementation of the feature set partitioning on NMC to construct the Multiple NMC Combination.

5. Conclusion

We have presented a new algorithm for constructing disjoint feature set partitioning. The basic idea is to decompose the original set of features into several subsets, construct NMC for each projection, and then combine them. This paper examines whether the new algorithm can be useful for discovering the appropriate partitioning structure based on diversity measure. The algorithm was evaluated on several dataset. The results show that this algorithm outperforms original NMC. This experimentation leads us to conclude that the proposed algorithm can be used for creating more accurate NMC ensembles. Additional issue to be further studied is how the feature set clustering can be implemented with other classifier.

References

[1] K. Fukunaga, *Introduction to statistical pattern recognition*, 2nd ed. San Diego, CA, USA : Academic Press Professional Inc., 1990.

[2] D. Shin, and S. Kim, Nearest mean classifier via-one class SVM, *International Joint Conference on Computational Sciences and Optimization* vol. 01, pp. 593-596, 2009.

[3] C. J. Veenman, and D.M.J. Tax, A weighted nearest mean classifier for sparse subspaces, *Proceedings of Computer Vision and Pattern Recognition* vol. 2, pp. 1171-1176, 2005.

[4] A. K. Jain, and B. Chandrasekaran, *Dimensionality and sample size consideration in pattern recognition practice*, Handbook of Statistics, vol. 2, pp. 835-855, 1982.

[5] L. Rokach, Genetic algorithm-based feature set partitioning for classification problems, *Pattern Recognition*, vol. 41(5), pp. 1676-1700, 2008.

[6] D. Han, C. Han, and Y. Yang, Multiple classifiers fusion based on weighted evidence combination, *Proceedings of the IEEE International Conference on Automation and Logistics*, pp. 2138-2143, 2007.

[7] C. Y. Suen, C. Nadal, A. Mai, R. Legault, and L. Lam, Recognition of totally unconstrained handwritten numerals based on the concept of multiple experts, *Proceedings of the International Workshop on Frontiers in Handwriting Recognition*, pp. 131-143, 1990.

[8] H. Parvin, H. Alizadeh, and B.M. Bidgoli, A new method for constructing classifier ensem bles, *International Journal of Digital Content Technology and its Applications*, vol. 3(2), pp. 62-64, 2009.

[9] P. Du, H. Sun, and W. Zhang, Target identification from high resolution remote sensing image by combining multiple classifiers, *Proceedings of Multiple Classifier System*, pp. 408-417, 2009.

[10] T. K. Ho, The random subspace method for constructing decision forests. *IEEE Transactions on Pattern Analysis and Machine Intelligence*, vol. 20(8), pp. 832-844, 1998.

[11] S. D. Bay, Combining nearest neighbor classifiers through multiple feature subsets. *Proceedings of the 17th International Conference on Machine Learning*, pp. 37–45, 1998.

[12] R. Bryll, R.G. Osuna, and F. Quek, Attribute bagging: improving accuracy of classifier ensembles by using random feature subsets, *Pattern Recognition*, vol. 36, pp. 1291–1302, 2003.

[13] L-J. Wang, X-L. Wang, and Q-C. Chan, GA-Based feature subset clustering for combination of multiple nearest neighbors classifiers, *Proceedings of the 4th International Conference on Machine Learning and Cybernetics*, pp. 2982-2987, 2005.

Information Engineering Letters, ISSN: **2163-4114**
Volume **3**, Number **3**, September, **2013**

Integer Programming Models for Finding Optimal Part-Machine Families

Cynthia A. Mason[1,a], and Anthony Vannelli[2,b]

[1] C. A. Mason, School of Engineering, University of Guelph, Guelph, ON, N1G 2W1 Canada.

[2] A. Vannelli, School of Engineering, University of Guelph, Guelph, ON, N1G 2W1 Canada.

[a] cmason01@uoguelph.ca, [b]vannelli@uoguelph.ca

doi.10.5729/iel.vol3.issue3.23

Keywords: Integer Programming, Clustering, Cellular manufacturing, Group Technology, Disaggrega-tion.

Abstract. In this paper, we develop integer programming models which find the optimal part-machine family solutions, that disaggregate a factory process at the lowest cost. The groupings created using the methods presented in this paper can then act as the basis for the application of Group Technology, which include machine placement, job scheduling, and part routing. Three exact 0−1 Linear Programming techniques are developed and presented. The first 0−1 Linear Programming technique only focuses on part subcontracting as a means to disaggregate, and the second only focuses on machine duplication to disaggregate, and the final method yields part-machine family disaggregation through simultaneous part subcontracting and machine duplication. Once these methods are applied to example problems, the results provide the exact solutions, which have not been found in previous work.

1. Introduction

Ever since the cost efficiencies and value of product mass production have been realized, issues relating to plant layout and machine cell partitioning have been encountered. Group technology (GT) has been introduced to deal with such issues. GT can be defined as the concept of identifying and exploiting the similarities between the components in a manufacturing process in order to group them in such a way that will improve the manufacturing process at every stage [1]. Companies with flexible manufacturing systems repeatedly seek to partition machine processes so that groups/cells may be independently located in an area that best meets the companies' financial goals; an example may include subcontracting a portion of a process overseas due to lower labor costs. Should an optimal (or near optimal) cell formulation be achieved, work-in-progress inventory can be reduced, along with shortened throughput times, shorter set up times, providing better quality products, and simplified product changeover [2], [3], [4], [5], [6].

This paper uses integer linear programming (ILP) as a basis in order to construct models that provide completely disaggregated part-machine cells/families for the manufacturing processes by "optimally" minimizing the appropriate cost objective. Previous approaches use "heuristic" methods to find "approximate" solutions to the disaggregation problem [7], [8]. Three approaches are developed and discussed in this paper:

1) part subcontracting to achieve disaggregated part-machine families,
2) machine duplication to achieve disaggregated part-machine families, and
3) part subcontracting with machine duplication to achieve disaggregated part-machine families.

Each of these models will be developed separately and applied to a small scale example for illustrative purposes.

Fig. 1: Visual representation of Test_Problem.

		15	*1*	*3*	*10*
		p_1	**p_2**	**p_3**	**p_4**
15	**m_1**	1	1	0	0
1	**m_2**	1	1	1	0
3	**m_3**	0	1	1	1
10	**m_4**	0	0	1	1

Table 1: *Test_Problem* in matrix form. Costs and part/machine numbers are in italic and bold, respectively.

The small scale example that will be used throughout this paper to aid in illustrating models and concepts discussed, is illustrated in Fig. 1. This example will be hereafter referred to as the *Test_Problem*. In this example the costs to duplicate machines (depicted by a square shape with an m_i inside) are provided above each machine symbol, and the costs to subcontract parts (depicted by a circular shape with a p_i inside) are provided below each part symbol. The *Test_Problem* can also be presented as a matrix. This matrix is illustrated in Table 1, with the cost in italics and the part indices in bold for the machine and parts. The columns represent the parts and the rows represent the machines; any position in which a 1 is present represents a connection between the part and machine, whereas a 0 indicates none.

In the following section the methods will be discussed and outlined. This section will develop and construct the three aforementioned novel models. The next section will provide the results of applying the models to a well known problem. The paper is then completed with a conclusion section which includes suggestions for future work of these methods.

2. Methods

The models presented in this section are constructed to find the best partitioning of a manufacturing process with respect to the desired cost objective. Each model will be constructed in detail, with each objective function and constraints discussed separately. The complete model will then be presented along with its solution to the *Test_Problem* (Fig. 1), presented in the Introduction.

2.1 Part Subcontracting.

The first model identifies the most cost effective partition of a manufacturing process using only part subcontracting as a means of process disaggregation. In the model, part i is said to be "manfucatured or not subcontracted" and placed in cell j if it is given a value of one, i.e. $p_{i,j} = 1$. If part i is subcontracted, it will be represented by a value of zero for all values of j, i.e. $p_{i,j} = 0$. The entire set of parts is provided by P. The cost to subcontract, c_i, is related to its respective part by it's subscript i, and it is assumed that the costs are the same irrespective of which cell the part is manufactured in.

To begin this model's construction, we begin by defining the objective function. The objective function minimizes the total cost spent on parts subcontracted in order to achieve complete disaggregation into k cells. This objective is created by summing the total cost to subcontract all of the parts and subtracting the costs of the parts not subcontracted. The objective function operates by actually maximizing the cost of the parts not subcontracted. In either case the final result provides the total cost to subcontract the parts which provide complete cell/family disaggregation. This function is illustrated as follows:

$$\min\left(\sum_{i=1}^{|P|} c_i - \sum_{i=1}^{|P|}\sum_{j=1}^{k} c_i p_{i,j}\right). \tag{1}$$

The variable $m_{i,j}$ indicates whether or not machine i is placed on cell j. Should machine i be placed in cell/family j, $m_{i,j} = 1$, otherwise $m_{i,j} = 0$. In order to ensure that every machine exists and is not duplicated, the following set of constraints are constructed for each machine in the machine set M:

$$\sum_{j=1}^{k} m_{i,j} = 1, i = 1, 2, \ldots, |M|.$$

The previous constraints do not restrict all the machines from being in a single cell, therefore a set of constraints must be constructed to prevent such an event. By setting a maximum number of machines allowed per cell (based on a near equipartition of costs), the following constraint may be constructed for each cell up to and including k:

$$\sum_{i=1}^{|M|} d_i m_{i,j} \leq \frac{\sum_{i=1}^{|M|} d_i}{k}(1+\varepsilon), j = 1, 2, \ldots, k$$

A *threshold* variable (ε) is included to allow the user to implement an upper bound on cell size to allow for asymmetrical cell sizes to occur. Note that the cost to disaggregate decreases as the threshold (ε) increases, due to the further increase in the solution space. The cost of each machine i is indicated by d_i.

The model must be constructed in such a way that the relationships between the parts and machines are accounted for. This is done by the construction of constraints which allow a part to be completely manufactured in cell j if and only if machines that process the part are also placed in cell j. For each part the total number of these constraints must be equal to the number of related machines times the total number of cells k. First we will define the machine element required to construct the constraint:

$$m_{p_{i(\alpha)},j} \triangleq \text{set of machines } (\alpha) \text{ attached to part i, e.g. } p_{2(k)} = \{1, 2, 3\}. \tag{2}$$

Now the constraints can be provided as follows:

$$p_{i,j} \leq m_{p_{i(\alpha)},j}, i = 1, 2, \ldots, |P| \text{ and } j = 1, 2, \ldots, k \tag{3}$$

The last set of constraints ensure that all machine variables are kept binary. The binary nature of these variables reinforce the aforementioned constraints.

$$m_{i,j} \in \{0,1\}, i = 1, 2, \ldots, |M| \text{ and } j = 1, 2, \ldots, k$$

Note that the part variable $p_{i,j}$ does not need to be a binary variable. This significantly reduces the problem's complexity while still providing a 0–1 solution. This is due to the relational constraints (Eq. 3) which restrict $p_{i,j}$ to binary values since the objective function maximizes the part variables to their upper bound determined by the binary machine variables. The resulting part subcontracting model is represented as follows:

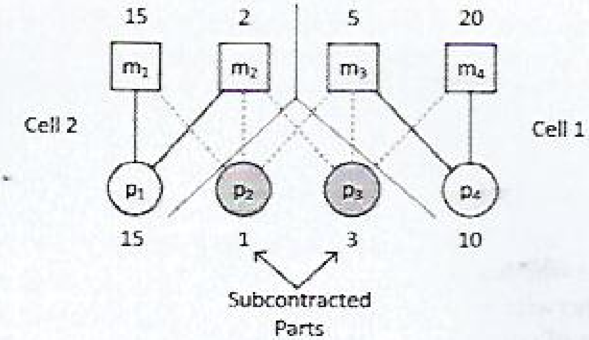

Fig. 2: Optimal subcontracting solution for *Test_Problem*.

$$\min\left(\sum_{i=1}^{|P|} c_i - \sum_{i=1}^{|P|}\sum_{j=1}^{k} c_i p_{i,j}\right) \triangleq \text{Minimizing Total Part Subcontracting Cost,}$$

$$\text{Subject to } \sum_{j=1}^{k} m_{i,j} = 1, i = 1,2,\ldots,|M|,$$

$$\sum_{i=1}^{|M|} d_i m_{i,j} \le \frac{\sum_{i=1}^{|M|} d_i}{k}(1+\varepsilon), j = 1,2,\ldots,k \tag{4}$$

$$p_{i,j} \le m_{p_{i(a)},j}, i = 1,2,\ldots,|P| \text{ and } j = 1,2,\ldots,k,$$

$$m_{i,j} \in \{0,1\}, i = 1,2,\ldots,|M| \text{ and } j = 1,2,\ldots,k.$$

Applying the model outlined in Eq. 4 with $\varepsilon = 0.5$ to the *Test_Problem* (Fig. 1), the solution illustrated in Fig. 2 is found as the optimal part subcontracting solution. It is clear that this is the most logical choice for complete disaggregation using part subcontracting at the lowest cost.

2.2 Machine Duplication.

The second model to be presented identifies the most cost effective partition of a manufacturing process using only machine duplication as a means to disaggregate. In this model, machine i is placed in cell j if it's respective variable is given a value of one; i.e., $m_{i,j} = 1$. If machine i is placed in more than one cell, then that will represent machine duplication. The entire set of machines is provided by M. The cost to duplicate a machine, d_i, is related to its respective machine by it's subscript i, and it is assumed that the costs are the same irrespective of which cell the machine is placed in.

To begin this model's construction we begin by defining the objective function. The objective function minimizes the total cost spent on machines duplicated in order to achieve complete disaggregation into k cells. This objective is created by summing the negative of the total costs to duplicate all of the machines and adding the costs of the machines duplicated. The objective function operates by minimizing the net cost spent on machines. This function is illustrated as follows:

$$\min\left(-\sum_{i=1}^{|M|} d_i + \sum_{i=1}^{|M|}\sum_{j=1}^{k} d_i m_{i,j}\right). \tag{5}$$

The first constraint is set to encourage the use of duplicate machines if necessary, should they lower the overall cost. If the solution suggests that a machine be placed in two separate cells simultaneously, this will represent machine duplication and the cost will be picked up in the aforementioned objective equation. This constraints assume each part is assigned to only one cell:

$$\sum_{j=1}^{k} m_{i,j} \geq 1, i = 1,2,...,|M|.$$

In order to ensure that parts are not processed in multiple cells (suggesting part process duplication) and no subcontracting is allowed, a constraint must be created to ensure that a part appears in only one cell/family. The following constraint provides this:

$$\sum_{j=1}^{k} p_{i,j} = 1, i = 1,2,...,|P|.$$

The previous constraints do not restrict all the parts from being in a single cell, therefore a set of constraints must be constructed to prevent such an event. By setting a maximum number of machines allowed per cell (based on a near equipartition of costs), the following constraint may be constructed for each cell up to and including k:

$$\sum_{i=1}^{|P|} c_i p_{i,j} \leq \frac{\sum_{i=1}^{|P|} c_i}{k}(1+\varepsilon), j = 1,2,...,k$$

Similar to the part subcontracting model, this model must also be constructed in such a way that the relationships between the parts and machines are accounted for. The same set of constraints will be used here, however will be discussed again for the sake of completeness. The part-machine relationships are created through the construction of constraints which allow a part to be completely manufactured in cell j if and only if all of its respective machines are also placed in cell j. For each part the total number of this type of constraint must be equal to the number of related machines times the total number of cells k. The definition for the $m_{p_{i(\alpha)},j}$ variable is provided in Eq. 2. The generalized relationship constraints are provided as follows:

$$p_{i,j} \leq m_{p_{i(\alpha)},j}, \quad i = 1,2,...,|P| \text{ and } j = 1,2,...,k.$$

The last set of constraints ensure that all machine variables are kept binary. The binary nature of these variables reinforce the aforementioned constraints.

$$m_{i,j} \in \{0,1\}, i = 1,2,...,|M| \text{ and } j = 1,2,...,k.$$

Again note that the part variable $p_{i,j}$ does not need binary constraints, therefore significantly reducing the problem's complexity while still providing a 0–1 solution. The resulting machine duplication model is represented as follows:

$$\min\left(-\sum_{i=1}^{|M|} d_i + \sum_{i=1}^{|M|}\sum_{j=1}^{k} d_i m_{i,j}\right) \triangleq \text{Minimizing Total Machine Duplication Cost,}$$

$$\begin{aligned}
\text{Subject to } & \sum_{j=1}^{k} m_{i,j} \geq 1, i = 1,2,...,|M|, \\
& \sum_{j=1}^{k} p_{i,j} = 1, i = 1,2,...,|P|, \\
& \sum_{i=1}^{|P|} c_i p_{i,j} \leq \frac{\sum_{i=1}^{|P|} c_i}{k}(1+\varepsilon), j = 1,2,...,k, \\
& p_{i,j} \leq m_{p_{i(\alpha)},j}, i = 1,2,...,|P| \text{ and } j = 1,2,...,k, \\
& m_{i,j} \in \{0,1\}, i = 1,2,...,|M| \text{ and } j = 1,2,...,k.
\end{aligned} \tag{6}$$

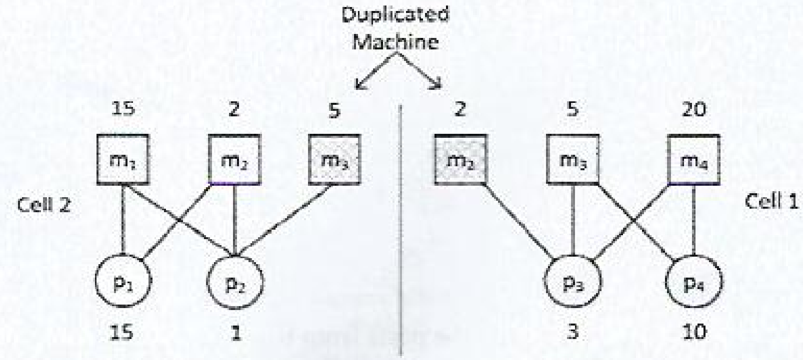

Fig. 3: Optimal machine duplication solution for *Test_Problem*.

Applying the model outlined in Eq. 6 with $\varepsilon = 0.5$ to the *Test_Problem* (Fig. 1), the solution illustrated in Fig. 3 is found as the optimal machine duplication solution. It is clear that this is the most logical choice for complete disaggregation using machine duplication at the lowest cost.

2.3 Part Subcontracting with Machine Duplication.

The third model to be presented identifies the most cost effective partition of a manufacturing process using both part subcontracting with machine duplication as a means to disaggregate. In the model, part and machine variables and costs are defined exactly as done in the previous two subsections.

To begin this model's construction we begin by defining the objective function. The objective function minimizes the total cost spent on parts subcontracted plus the total cost spent on machines duplicated in order to achieve complete disaggregation into k cells. This objective is created by adding the two objective functions described in Eq. 1 and 5. This function is illustrated as follows:

$$\min \left(\sum_{i=1}^{|P|} c_i - \sum_{i=1}^{|P|} \sum_{j=1}^{k} c_i p_{i,j} - \sum_{i=1}^{|M|} d_i - \sum_{i=1}^{|M|} \sum_{j=1}^{k} d_i m_{i,j} \right)$$

As in the Machine Duplication section, the first constraint is set to encourage the use of duplicate machines if necessary, should they lower the overall cost. If the solution suggests that a machine be placed in two separate cells simultaneously, this will represent machine duplication and the cost will be picked up in the aforementioned objective equation. This constraint is described as follows:

$$\sum_{j=1}^{k} m_{i,j} \geq 1, i = 1, 2, \ldots, |M|.$$

In order to ensure that parts are not processed in multiple cells (suggesting part process duplication) a constraint must be created to ensure that a part appears in at most one cell/family. This allows a part to not be placed at all, therefore representing part subcontracting. The following constraint provides this:

$$\sum_{j=1}^{k} p_{i,j} \leq 1, i = 1, 2, \ldots, |P|.$$

Similar to the first two models, cell sizes need to be controlled in order to prevent all the parts from being in a single cell. By setting a maximum number of machines allowed per cell (based on a near equipartition of costs), the following constraint may be constructed for each cell up to and including k:

$$\sum_{i=1}^{|P|} c_i p_{i,j} \leq \frac{\sum_{i=1}^{|P|} c_i}{k} (1 + \varepsilon), j = 1, 2, \ldots, k$$

Just as in both the part subcontracting model and the machine duplication model, this model must also be constructed in such a way that the relationships between the parts and machines are accounted for. The same set of constraints will be used here, however they will be presented again for the sake of completeness. The part-machine relationships are created through the construction of constraints which allow a part to be completely manufactured in cell j if and only if all of its respective machines are also placed in cell j. For each part the total number of this type of constraint must be equal to the number of related machines times the total number of cells k. The definition for the $m_{P_{i(\alpha)},j}$ variable is provided in Eq. 2. The generalized relationship constraints are provided as follows:

$$p_{i,j} \le m_{P_{i(\alpha)},j},\ \ i = 1,2,...,|P| \text{ and } \ j = 1,2,...,k.$$

The last set of constraints ensure that all part and machine variables are kept binary. The binary nature of these variables reinforce the aforementioned constraints. The machine and part binary constraints are provided by:

$$p_{i,j} \in \{0,1\}, i = 1,2,...,|P| \text{ and } j = 1,2,...,k, \text{and}$$
$$m_{i,j} \in \{0,1\}, i = 1,2,...,|M| \text{ and } j = 1,2,...,k.$$

The complete compilation of these constraints is provided as follows:

$$\begin{aligned}
&\min \left(\sum_{i=1}^{|P|} c_i - \sum_{i=1}^{|P|}\sum_{j=1}^{k} c_i p_{i,j} - \sum_{i=1}^{|M|} d_i + \sum_{i=1}^{|M|}\sum_{j=1}^{k} d_i m_{i,j} \right) \\
&\text{Subject to } \sum_{j=1}^{k} m_{i,j} \ge 1, i = 1,2,...,|M|, \\
&\sum_{j=1}^{k} p_{i,j} = 1, i = 1,2,...,|P|, \\
&\sum_{j=1}^{|P|} c_i p_{i,j} \le \frac{\sum_{i=1}^{|P|} c_i}{k}(1+\varepsilon), j = 1,2,...,k, \\
&p_{i,j} \le m_{P_{i(\alpha)},j}, i = 1,2,...,|P| \text{ and } j = 1,2,...,k, \\
&p_{i,j} \in \{0,1\}, i = 1,2,...,|P| \text{ and } j = 1,2,...,k \\
&m_{i,j} \in \{0,1\}, i = 1,2,...,|M| \text{ and } j = 1,2,...,k.
\end{aligned} \tag{7}$$

Applying the model outlined in Eq. 7 with $\varepsilon = 0.5$ to the *Test_Problem* (Fig. 1), the solution illustrated in Fig. 4 is found as the optimal machine duplication solution. It is clear that this is the most logical choice for complete disaggregation using part subcontracting with machine duplication at the lowest cost.

	Hall [7] Part Subcontracting	Hall [7] Machine Duplication	0 − 1 Part & Machine LP (Eq. 7) (ε)	Minimum Improvement
manf1 (unweighted) [9]	\$8	\$4	\$2 (0.03)	50%
manf1 (weighted) [9]	\$239	\$153	\$14 (0.03)	91%
manf2 [10]	\$16	\$4	\$2 (0.07)	50%
manf3 [11]	\$15	\$30	\$7 (0.19)	53%

Table 2: Comparing previously found solutions to *0 − 1 Part & Machine LP* solutions.

Machine	Machine Cost (\$)	Processed Part(s)	Machine	Machine Cost (\$)	Processed Part(s)
1	2	10 31 32 33 39 41	16	35	6 28
2	13	11 12 18 32 33 39 41	17	29	7 16 27 36
3	34	12 23 31 32 39 40	18	28	14 16 27 34
4	5	7 15 24 25 28 35	19	21	1 3 21 22 30
5	7	5 17 34 36	20	20	1 3 21 22
6	9	6 26	21	33	10 12 31 32 33 40
7	22	16 27 34 36	22	6	10 12 23 31 32 39 40
8	32	1 8 9 14 29	23	5	2 12 23 31 39
9	40	3 13 21	24	2	38
10	17	2 12 20 23 39	25	22	4
11	15	10 33 39 41	26	39	16 27 34 36
12	3	11 12 19 20 23 24 39 40	27	12	8 15
13	10	19 25 38	28	19	8 29 35
14	11	4 5 18 26 37	29	16	1 3 9 13 21 30
15	23	17 37	30	36	1 3 21 22
Part Costs (\$) in Ascending Order	15, 50, 19, 71, 68, 48, 47, 380, 26, 165, 232, 229, 22, 33, 121, 132, 34, 39, 48, 166, 21, 25, 80, 18, 91, 45, 69, 110, 47, 42, 49, 55, 249, 44, 60, 41, 35, 48, 116, 54, 52				

Table 3: Hall's *manf1* problem [7].

Processor, W3550 3.07 GHz and 3.06 GHz), the results strongly support further investigation and application.

Future work for the models presented here includes factoring in floorspace and load balance con-straints. These constraints may be included in the cell size constraints. Since the models run so quickly for each of these models shop scheduling may be a valuable extension.

Acknowledgment

Part of the research of A. Vannelli is supported by a National Sciences and Engineering Research Counsel (NSERC) Discovery Grant.

References

[1] J. Wang, and A. Kusiak: Computational Intelligence In Manufacturing Handbook. Advanced Topics in Mechanical Engineering Series. Taylor & Francis. (2010)

[2] N. Gaither: Productions and Operations Management. Fort Worth, TX HBJ. (1992)

[3] N. Hyer: The Potential of Group Technology for U.S. Manufacturing. Journal of Operations Management Vol. 4 (1984), p. 183192.

[4] N. Hyer, and U. Wemmerlov: Group Technology and Productivity. Harvard Business Review Vol. July-Aug. (1984), p. 140149.

[5] N. Suresh, and J. Meredith: Achieving Factory Automation Through Group Technology Principles. Journal of Operations Management Vol. 5 (1985), p. 151167.

[6] H. Wang, B. Alidaee, F. Glover, and G. Kochenberger: Solving group technology problems via clique partitioning. International Journal of Flexible Manufacturing Systems Vol. 18 (2006), p. 7797.

[7] R.G. Hall: Mathematical Programming Approaches for Finding Part-Machine Families. Master's thesis. University of Waterloo. (1991)

[8] A. Kusiak, A. Vannelli, and K.R. Kumar: Grouping problem in scheduling flexible manufacturing systems. Robotica Vol. 3 (1985), p. 245-252.

[9] K. Kumar, and A. Vannelli: Strategic subcontracting for efficient disaggregated manufacturing. International Journal of Production Research Vol. 25 (1987), p. 17151728.

[10] J.R. King: Machine-component grouping in production flow analysis: an approach using a rank order clustering algorithm. International Journal of Production Research Vol. 18 (1980), p. 213-232.

[11] J.R. King, and V. Nakornchai: Machine-component group formation in group technology: review and extension. International Journal of Production Research Vol. 20 (1982), p. 117–133.

Information Engineering Letters, ISSN: **2163-4114**
Volume **3**, Number **3**, September, **2013**

Semi-empirical Model for Broadband Powerline Communication Channels

Chrispin T. Mulangu[a], Thomas J.O. Afullo[b], Nelson.M. Ijumba[c]

School of Electrical, Electronic & Computer Engineering, University of KwaZulu-Natal, Durban 4041, South Africa

[a]mulangu@ukzn.ac.za, [b]afullot@ukzn.ac.za, [c]ijumban@ukzn.ac.za

doi.10.5729/iel.vol3.issue3.34

Keywords: Powerline communication, Multipath, Scatterers

Abstract. Impedance discontinuities in the indoors powerline communication channels (PLC) lead to the multipath propagation phenomenon. Impedance of the electrical loads and the branching are the main causes of impedance discontinuities in PLC networks. The significance of the impact of the impedance discontinuity on the transmit signal may only be revealed by having an exact knowledge of the impedances at the corresponding discontinuity locations.Possession of this information is very unlikely considering the variety of electrical loads with different impedance characteristics that can be connected to the medium as well as the differences in PLC network topologies leading to different branching structures. Therefore, statistical approachseems to be appropriate for PLC networks.The model is based on the validation of the assumption of a randomly spread multitude of scatterers in the vicinity of the channel that only required a sufficient number impedance discontinuity points. We consider the line as one single element, and its length was divided into a grid of small areas with dimensions range from 0.5 to 3 mm. Thus, each small area transmits an echo and the forward scattered response get to receiver. With this approach, specific attenuation along the line can be determined using 3 as the minimum number of branching nodes$x$, hence a and b can assume in order tomake sure that a branching in a branching node takes placeand finally, the transfer function is derived.

1. Introduction

Powerline communication (PLC) channel exhibits unfavorable transmission properties. It is characterized by a frequency selective transfer function; attenuation that increases with length and frequency, and severe narrowband interference [1]. In order to overcome these difficulties, a lot of effort has been undertaken to characterize the modelling of the power line channel [2]-[3]. An understanding of complete behaviour of broadband PLC channel is important [4] when setting up PLC transmission lines [5], and simulating the performance of advanced communication technologies [6, 7]. Several models have been proposed for characterizing the (PLC) [8]-[9] channel. An interesting approach describes the PLC by its multipath behaviour [10, 11].

The multipath propagation of the power-line communication channel (PLC) arises from the presence of several branches and impedance mismatches that cause multiple reflections. Each path comprises of scattering points that are reflected at specific number of times at specific points of discontinuityalong its routes. Scattering points are located where impedance mismatch occurs. In such models, not only the desired signal, but also one or more delayed and attenuated versions of it get to the receiver. In [12], there is a discussion of scattering points' spatial allocation, by which path amplitude distributions and path arriving time distributions are proposed to follow the lognormal distribution for different number of branches. In [13], the investigation carried out that the first arriving path is distinguishablefrom the other paths in the sense that it experiences lessreflection and less attenuation along its propagation path, givingit a favorable position regarding detectability. In his study, statisticsof the first arriving path are initially investigated. It is shownthat the first arriving path can be defined with log-Normal probabilitydensity function. It is seen that the mean of the approximatinglog-Normal variable decreases with an increasing numberof branches between transmitter and receiver while its varianceincreases. The same finding is also observed when the maximumnumber of branches that extend out a branching node is increased.In this paper, the first arriving path is investigated and the the line as one single element, and its length was divided into a grid of small areas with dimensions range from 0.5 to 3 mm where, each small area transmits an echo and the forward scattered response get to receiver. Assuming small area is spherical, and then Mie scattering is applied to it in order to determine attenuation based on forward scattering.

2. PLC network analysis

Considering that transmission of an impulse $\delta(t)$ through a multipath environment with L paths results in a train of delayed impulses [12]

$$H(\tau_d, t) = \sum_{i=1}^{L} r_i e^{j\theta_i} \cdot e^{-\alpha l_i} \cdot \delta(t - \tau_{di}) \tag{1}$$

where,

$$\tau_{di} = \frac{l_i}{v} = \frac{l_i}{\omega/\beta} \tag{2}$$

($r_i e^{j\theta_i}$) is reflection factor of ith path, given by:

$$r_i e^{j\theta_i} = \prod_{k=1}^{M_1} T_{ik} \prod_{n=1}^{M_2} \Gamma_{in} \tag{4}$$

where M *and* k present the number of reflection and transmission coefficients included in path, l_i is the path's length and$v$ is the group velocity of propagation.T *and* Γ represent transmission and reflection coefficients.With this observation, its characterization along the direct path$(i = 0)$is essential for understanding the first arriving path.

Note that the reflection factor of the first arriving path is composed of only the transmission coefficients experienced along the direct path stemming from the impedance discontinuities at the branching nodes. So, calculating is sufficient in order to characterize the reflection factor of the first arriving path.

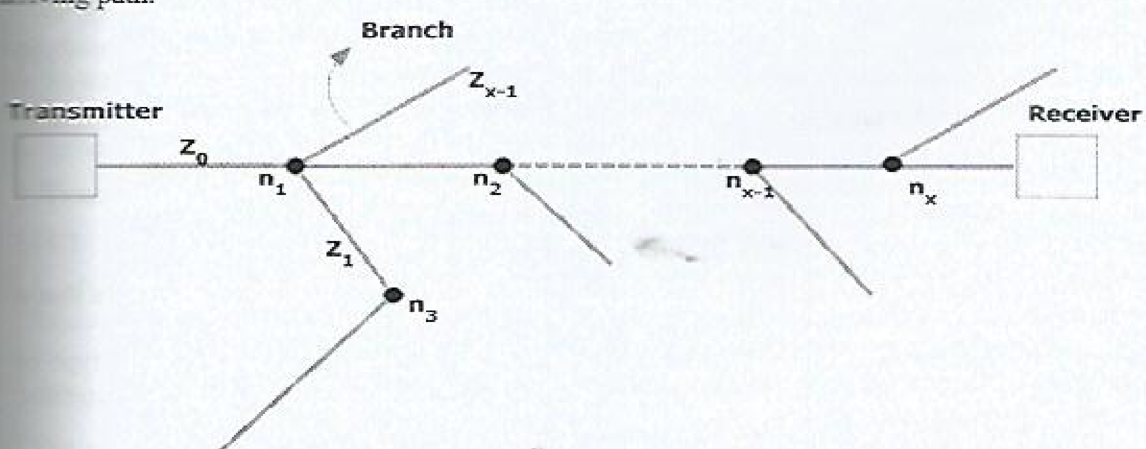

Fig. 1. PLC network analysis

Also we can have it in equivalent frequency response, is expressed as:

$$H(f) = \sum_{i=1}^{L} r_i e^{j\theta_i} \cdot e^{-\alpha l_i} \cdot e^{-j\omega\tau_{di}}$$

$$= \sum_{i=1}^{L} r_i e^{j\theta_i} \cdot e^{-\gamma l_i} \quad (5)$$

where, γ is the propagation coefficient.

Fig. 1, shows the direct propagation path between transmitter and receiver operating on a PLC system consists of several branching nodes denoted by n_i. These branches extending from each branching node may be terminated by an electrical load or lead to another branching node depending upon the network structure.

According to transmission line theory, reflection and transmission coefficients at a branching node are expressed by considering parallel connections of extended branches as follows [2]:

$$\Gamma = \frac{(Z_1//Z_2 ...//Z_z) - Z_0}{(Z_1//Z_2 ...//Z_z) + Z_0}; \qquad T = \Gamma + 1 \quad (6)$$

where Z_0 is characteristic impedance of the incident signal and Z_z or characteristic impedance of branching node.

If all branches is equal to each other (Z_0), Eq. 6 can be expressed as:

$$\Gamma = \frac{2 - z}{z}; T = \frac{2}{z} \quad (7)$$

where z refers to the total number of branches extending from a particular branching node.

Referring back to Fig. 1, assuming that the transmitter and receiver are matched to the impedance of the corresponding characteristic impedance of the cable for the sake of simplicity, is composed of multiplication of x transmission coefficients as follows:

$$r_0 e^{j\theta_0} = \frac{2}{n_1}\frac{2}{n_2} \cdots \frac{2}{n_x} = \frac{2^x}{n_1 * n_2 * \cdots * n_x} \quad (8)$$

where $n_i (i = 1, 2, ..., x)$ is the number of paths extending from a branching node, including the path on which the incident signal propagates. Note that the phase term $\theta$of the reflection factor is 0 for this particular case since n_i cannot be a complex number ($r_0 e^{j\theta_0} = r_0$).

The eq.8 can be expressed as:

$$Y = \ln(|r_0|) = x\ln 2 - \sum_{i=0}^{x} \ln n_i \quad (9)$$

Y is an RV with the following mean, μ and variance, σ^2:

$$\mu = x\ln 2 - \sum_{i=0}^{x} [\ln(n_i)] \; and \; \sigma^2 = \sum_{i=0}^{x} Var[\ln(n_i)] \quad (10)$$

where n is used to refer both the branching node itself and the number of the branches extending from it.

If n_i are assumed to be identically uniformly distributed discrete RV over $[a, b]$, then

$$\mu = \frac{-x}{b - a + 1} ln \frac{b!}{(a - 1)!} + x\ln 2 \quad (11)$$

Note that 3 is the minimum number that a, hence$a$ and b can assume in order make sure that a branching in branching node takes place, [13].

Having a homogeneous PLC medium is physically very difficult even though the same type of cable is used throughout the network due to the variety of factors that affect the characteristic impedance.

If we were to continue with the homogeneity assumption, a deviation term which implies the minor changesof impedances across the branching nodes can be considered to be more practical. This way, the impedance of a branch which was assumed to equal Z_0can now be assumed to be $Z_0 + d_e$,where d_e denotes the deviation from Z_0 . Similar to the previouscase, several assumptions can be made regarding the characteristicsofd_e. Treating as an uniformly distributed RV over a range which can be considered as a very small fraction ofZ_0guarantees reflection factor $|r_0|$to be a continuous RV.

Base on Monte Carlo simulations, [13],show the mean and variance of (logarithm of the reflection factor) when and are assumed to be 50Ω and uniformly distributed over$[-25\Omega, 25\,\Omega]$, respectively. This corresponds to a PLC in which the characteristic impedance of the cables takes some value between $25 - 75\,\Omega$ according to uniform distribution. Note that impedance characteristic varies slightly with frequency from $50.25\ \Omega$ at 0.1 GHz to$49.95\ \Omega$ at 20 GHz, [13].

The mean and variance of are related to the number of branching nodes with the following twoequations:

$$\mu = -0.822x - 9.23 \times 10^{-5} \qquad (12)$$
$$\sigma^2 = 0.086x - 0.00237$$

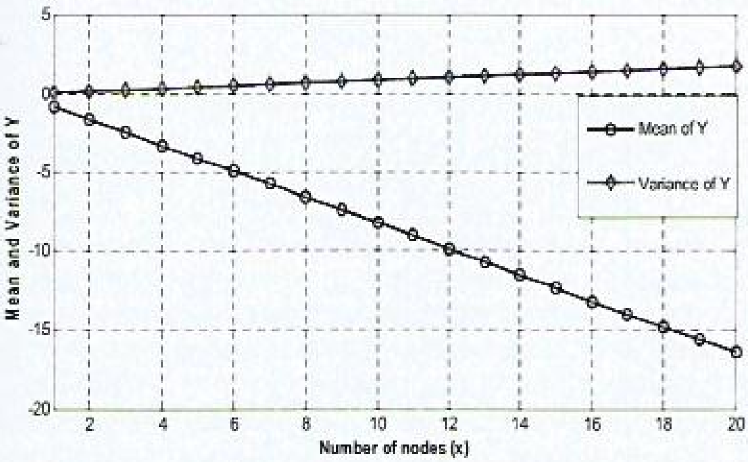

Fig.2. Variance and mean of Y with$Z_o = 50\Omega$ and $d_e = U[-25\Omega, 25\Omega]$

3. Model and Limitation

The model is based on the validation of the assumption of a randomly spread multitude of scatterers in the vicinity of the channel that only required a sufficient number impedance discontinuity points [13].

We consider the line as one single element, and its length was divided into a grid of small areas with dimensionsrange from 0.5 to 3 mm as in Fig. 3. Thus, each small area transmits an echo and the forward scattered response get to receiver. With this approach, specific attenuation can be determined as the attenuation due to rain. In this case, the number of branching nodes is considered like rain rate and raindrops are presented by small areas.

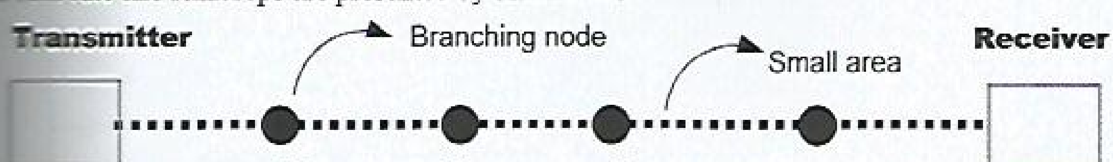

Fig.3. Indoor PLC model

The amplitude of an electromagnetic wave travelling through a volume, containing N identical scattering particles with diameter D, at any distance l, decreases by the amount of $e^{-\gamma l}$. The attenuation coefficient $A = NQ_{ext}(D)$. The attenuation of the wave is then given in dB as follows:

$$A_{dB} = 10\log\frac{1}{e^{-Al}} = 4.343Al. \quad (13)$$

$$A_s[dB/m] = 4.343\int_0^{\infty} N(D)Q_{ext}(D)dD. \quad (14)$$

where $N(D)$ is the small area scattering, and $Q_{ext}(D)$ is the extinction coefficient in mm^2.

The mathematical development to simulate attenuation of the signal is based on Mie scattering approach as in Fig. 6.In [12-13], the estimation of the path amplitude distributions, authors used lognormal distribution with two parameters, μ and σ. While in this model, we included the third parameter N_t as in equation below.

$$N(D_i) = \frac{N_t}{\sigma\sqrt{2\pi}}\exp\frac{-(\ln(D_i) - \mu_i)^2}{2\sigma_i^2} \quad (15)$$

where N_t is the number impedance discontinuity points. The independent input, D_i the mean diameter of the small area. The input parameters $N_t, \mu,$ and σ are obtained by using Monte Carlo simulations with corresponding branching nodes $(x)$to yield:

$$N_t = a_o x^{b_o}$$
$$\mu = A_\mu + B_\mu \ln(x) \quad (16)$$
$$\sigma^2 = A_\sigma + B_\sigma \ln(x)$$

where $a_o, b_o, A_\mu, B_\mu, A_\sigma$ and B_σ all represent the regression coefficients of input parameters corresponding to the lognormal model.Table 1 shows the applied regression fittings for the lognormal proposed model according to their input parameters for the number of branching nodes as described in (15). We note that the fitted results of the values N_t show dependency to the number of branching nodes (x). Figures 4-5 show the Small areas scattering distributions models developed for PLC channel for different number of branching nodes (x): $x = 4$ *and* 10.

Table 1: Model parameters

a_o	b_o	A_μ	B_μ	A_σ	B_σ
73.1	0.285	-0.479	0.003	0.072	0

The Small areas scattering distribution and probability density distribution in the indoor single-phase networks show that there are more scattering points at lower diameter sizes where the mean peak diameter is about 0.8 mm. That is implied more reflections of signal in this range of diameters. The results show that the distributions do not dependents on indoor network topology.

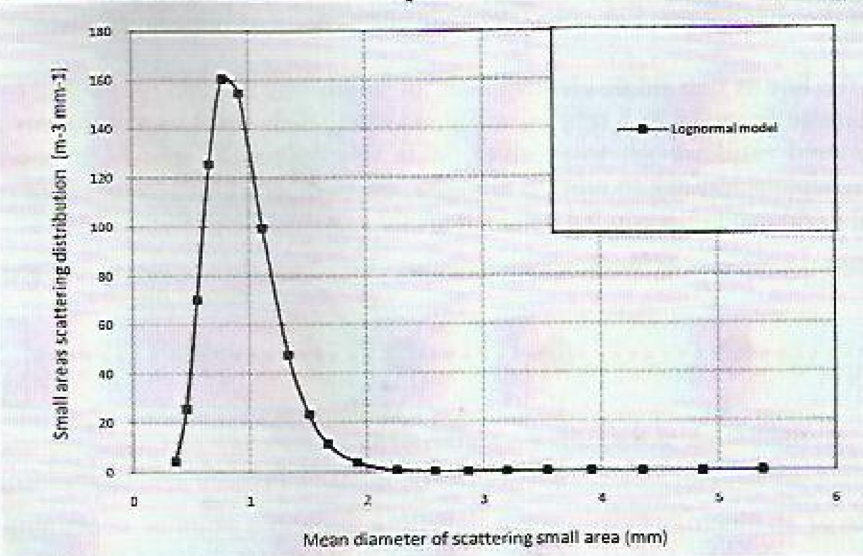

Fig. 4. Small areas scattering distribution for PLC channel with four branching nodes

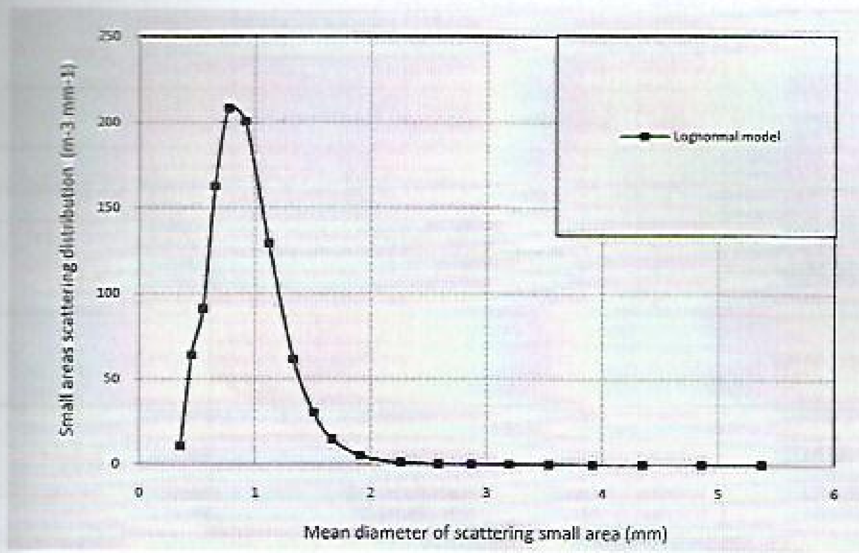

Fig. 5.Small areas scattering distribution for PLC channel with ten branching nodes

Based on Mean got in [13] as a function of the requirement to have existence branching within a and b branching node interval, the Mean (**μ**) in Eq.12 is modified andgiven by

$$\mu = -0.0479 + 0.003 \times \frac{-x}{b-a+1} ln \frac{b!}{(a-1)!} \tag{17}$$

4. Channel parameters

Referring to attenuation equation in Eq. 13, based on Eq. 14 and 15, we set the range of 10 - 100 MHz. Having in mind that the indoor PLC has high number of branching nodes (x_i), we fix $x_i = 4$, and as interval$a = 3$ and $b = 5$.

Then,in Fig. 6, the specific attenuations is plotted and the power law model was suggested where the attenuation parameters are carried out by regression. The specific attenuation is then expressed as

$$A_s = \alpha_0 + \alpha_1 f^k \tag{18}$$

Hence the attenuation parameters are given as $k = 2.4$, $a_o = 3 \times 10^{-21} m^{-1}$, $a_1 = 0\, s/m$. Tables 2-5, summarize the attenuation parameters for different frequency ranges.

Table 2: Attenuation parameters for four nodes.

Frequency	Model	umber of branching nodes 4	Coeff. of goodness R^2
10 - 100 MHz	a_0	$4x10^{-21}$	1
	k	2.4	
	a_1	0	
100-200 MHz	a_0	$2x10^{-23}$	1
	k	2.7	
	a_1	0	
200- 300 MHz	a_0	$3x10^{-9}$	0.99
	k	0	
	a_1	-0.219	
300 - 500 MHz	a_0	$9x10^{-10}$	0.98
	k	0	
	a_1	0.297	
0.5 - 1GHz	a0	$5x10^{-10}$	0.99
	k	0	
	a_1	0.516	

1 - 3GHz	a_0	$2x10^{-10}$	0.99
	k	0	
	a_1	0.80	

Table 3: Attenuation parameters for fifteen nodes

Frequency	Model	umber of branching nodes 15	Coeff. Of goodness R^2
10 - 100 MHz	a_0	$7x10^{-21}$	1
	k	2.4	
	a_1	0	
100- 200 MHz	a_0	$8x10^{-9}$	1
	k	0	
	a_1	-0.625	
200- 300 MHz	a_0	$4x10^{-9}$	0.98
	k	0	
	a_1	0.359	
300 - 500 MHz	a_0	$2x10^{-9}$	1
	k	0	
	a_1	0.866	
0.5 - 1GHz	a_0	$9x10^{-10}$	0.99
	k	0	
	a_1	1.324	
1 - 3GHz	a_0	$4x10^{-10}$	1
	k	0	
	a_1	1.774	

Table 4: Attenuation parameters for ten nodes

Frequency	Model	Number of branching nodes 10	Coeff. Of goodness R^2
10 - 100 MHz	a_0	$5x10^{-21}$	1
	k	2.4	
	a_1	0	
100- 200 MHz	a_0	$6x10^{-9}$	1
	k	0	
	a_1	0.49	
200- 300 MHz	a_0	$3x10^{-9}$	0.98
	k	0	
	a_1	0.092	
300 - 500 MHz	a_0	$1x10^{-9}$	1
	k	0	
	a_1	0.654	
0.5 - 1GHz	a0	$7x10^{-10}$	0.99
	k	0	
	a_1	0.1	
1 - 3GHz	a_0	$3x10^{-10}$	1
	k	0	
	a_1	1.4	

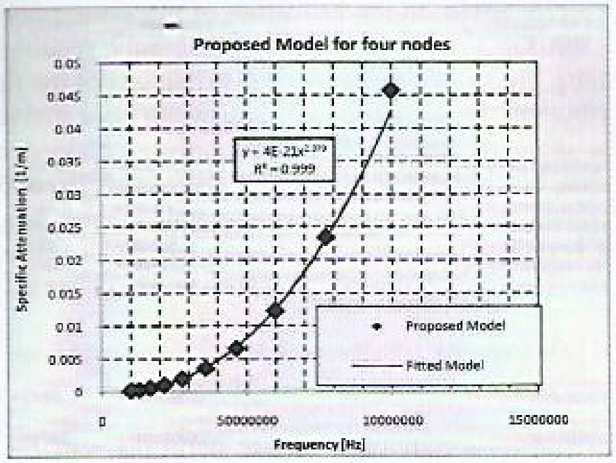

Fig. 6. Proposed Specific attenuation model in powerline for x = 4branching nodes at 10- 100 MHz.

Considering a transmission line of length d and characteristic impedance Z_0, terminated at the load end (position $Z = d$) with impedance Z_L and excited by a signal generator with impedance Z_g at the other end ($Z = 0$), voltage signals at the line's ends are related as follows:

$$H(f) = \frac{V(d)}{V(0)} = \frac{e^{-\gamma d}(1+\rho_L)}{1-\rho_L e^{-\gamma d} e^{-j\beta d}} \tag{19}$$

where γ the attenuation constant, β the phase-angle constant, $H(f)$ the line's transfer function from $Z = 0$ to $Z = d$and $\rho_L$the reflection coefficient at $Z = d$.

For low-loss line, β is given by:

$$\beta = \frac{2\pi f\sqrt{\varepsilon_r}}{c_o} \tag{20}$$

where $c_o = 3 \times 10^8\ m/s$

Then the transfer function can be expressed as:

$$H(f) = \frac{e^{-\gamma d}(1+\rho_L)}{\sqrt{(1+\rho_L e^{-2\gamma d}\cos{(2\beta d)})^2+(\rho_L e^{-2\gamma d}\sin{(2\beta d)})^2}} \tag{21}$$

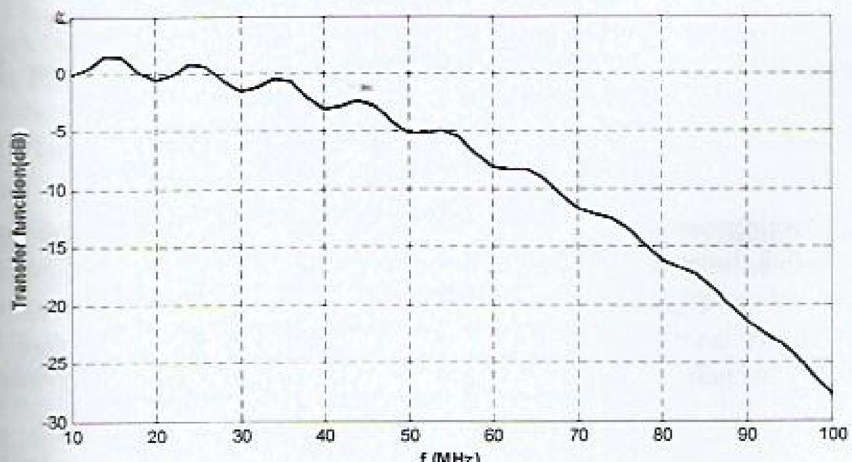

Fig. 7. Channel Transfer function

5. Conclusion

This paper shows that the transmission line can be modelled as one single element, and its length was divided into a grid of small areas, where each small area transmits an echo and the forward scattered response get to receiver based on the validation of the assumption of a randomly spread multitude of scatterers in the vicinity of the channel that only required a sufficient number impedance discontinuity points. By knowing amplitude distributions of the first path in the network, as followed lognormal distribution, the scatterers distribution has been derived as it's also followed lognormal distribution. The input parameters $N_t, \mu,$ and σ were obtained by using Monte Carlo simulations with corresponding branching nodes (x). The attenuation over the line is determined by threeinput parameters corresponding to 3 as the minimum number that x, hence a and b can assume in order tomake sure that a branching in a branching node takes place.Based on that, the transfer function is also determined. The measurements are still to be done in order to compare the suggested model.

References

[1] P. A. Brown, "High frequency conditioned power networks," in *UTC Annu. Conf. Proc.*, July/Aug. 1995.

[2]Göran Lindell, "On Coding and Modulation for the Power-line Communication Channel", *Proceeding of ISPLC 2001*, Sep., 2001, pp. 14-17.

[3] Markus Sebeck and Gerd Bumiller, "A Network Management System for Power-line Communication and its Verification by Simulation", *Proceeding of ISPLC 2000, Limerick, Ireland*, April, 2000, pp.225-232.

[4] K. Dostert, "Telecommunications over power distribution grid: Possibilities and limitations," *ISPLC'1997,* Essen Germany, 1997.

[5] M. Zimmermann, K. Dostert, "A multi-path signal propagation model for the powerline channel in the high frequency range," *ISPLC'1999*, pp.45-51, Lancaster U.K., 1999.

[6] T. Esmailian, P.G. Gulak, and F.R. Kschischang, "A discrete multitone power line communications system," *Proc. of ICASSP'00, vol. 5, pp. 2953-2956*, Jun. 2000.

[7] E. Liu, Y. Gao, G. Samdani, Omar Mukhtar, and T. Korhonen, "Broadband powerline channel and capacity analysis," *ISPLC 2005, pp.7-11*, April. 2005.

[8] H. Philipps, "Modeling of Power Line Communications Channels", *ISPLC'99, Lancaster*, UK, April 1999.

[9] O.G. Hooijen, "On the Relation Between Network Topology and Power Line Signal Attenuation", *ISPLC'98, Tokyo, Japan*, March 24-26, 1998.

[10] M. Zimmermann, K. Dostert, "A Multipath Model for the Power Line Channel", *IEEE Trans. Commun.*, vol. 50, no. 4, pp.553-559, April 2002.

[11] H. Philipps, "Development of a Statistical Model for Power Line Communications Channels", ISPLC'00, Limerick, Ireland, April 2000.

[12] Papaleonidopoulos, I.C., C.N. Capsalis, C.G. Karagiannopoulos and N.J. Theodorou, "Statistical Analysis and Simulation of Indoor Single-Phase Low Voltage Power-Line Communication Channels on the basis of Multipath Propagation," *IEEE Trans. Consumer Electronics*, Vol.49, No. 1,pp. 89-99, February 2003.

[13] Sabih Güzelgöz, Hasan Basri Çelebi, and Hüseyin Arslan, " Statistical Characterization of the Paths in Multipath PLC Channels", *IEEE Trans. On Power Delivary, vol.26, No.1*, January 2011.

[14] Papaleonidopoulos, I.C., C.N; C.G. Karagiannopoulos and N.J. Theodorou" Modelling Of Indoor Low Voltage Powerline Cables In The High Frequency Range", in *Proc. Int. Symp. Power-lines Comm.*, Athens, Greece, 2002.

Information Engineering Letters, ISSN: **2163-4114**
Volume **3**, Number **3**, September, **2013**

Radar ReflectivityParameters along Radio Links

Chrispin T. Mulangu[1,a], Senzo J. Malinga[2,b], Thomas J.O. Afullo[3,c]

Department of Electrical Engineering, Mangosuthu University of Technology, Umlazi, KwaZulu-Natal, 4031, South Africa

School of Electrical, Electronic & Computer Engineering, University of KwaZulu-Natal, Durban 4041, South Africa

[a]mulangu@mut.ac.za, [b]senzo@mut.ac.za, [c]afullot@ukzn.ac.za

doi.10.5729/iel.vol3.issue3.43

Keywords: Backscattering, Attenuation, Raindrop

Abstract. Radiowave propagating through a rain zone, will be scattered, depolarized, absorbed and delayed in time. All these effects of rain on the wave propagation are related to the frequency at which the signal is transmitted and polarization of the wave as well as to the rain rate, which influences the form and size distribution of the raindrop. The average power received by the bistatic radar is proportional to the product of reflectivity and attenuation. For rainfall intensity above about 10 mm/h, the diameters of raindrops are in the order of the wavelength, so backscattering is predominantly due to Mie scattering law where the average backscattering cross section depends weakly on raindrop diameter. Since the raindrop diameter D appears as the sixth power, it follows that in any raindrop size distribution, the small number of large drops will contribute the largest amount of received echo power of the rain. These can be measured in practice but sometime there is need to determine them separately. In order to determine radar reflectivity, backscattering coefficient needs to be estimated. This study makes predictions about backscattering coefficient caused by hydrometers along terrestrial radio links, operated at wide bandwidth of 10-140 GHz frequencies. The scattering properties of the spherical raindrop are calculated for different sizes of raindrops. From the scattering properties, the back cross-sections for the spherical raindrops are determined for different frequencies. These are integrated over different established raindrop-size distribution models to formulate radar reflectivity and fitted to generate power-law models.

1. Introduction

Terrestrial links operating at frequencies higher than 10*GHz* suffers degradation due to rain. Rain attenuation modeling on earth-space path has been conducted by many researchers and number of rain attenuation prediction models has been developed. Currently, ITU-R models are recommended models used to predict rain attenuation since, on average, they are simplified and have better accuracy [1]. However, to predict the signal degradation that will result from a rain event, the knowledge of the scattering cross section as well as the extinction properties are of importance [2]. A number of different techniques have been employed in seeking solutions to this problem. Spherical drops have been analysed by the use of the Mie Theory but other shapes may require a more complex analysis [2]. Among the methods which have been used in treating non-spherical raindrops are perturbation analysis [3,4,5], point matching techniques [5,6] and integral equation formulations of the problem [7].

In this study, results for backscatter cross section and attenuation are calculated with a Mie scattering code for spherical drops at 19, 60 and 140 GHz, . Result from the scattering algorithm is applied to the drop size distribution measured by Afullo in Durabn, South Africa, [8], thereafter, the relationship between rainfall and radar reflectivity is derived.

2. Raindrop Distribution

The lognormal raindrop size distribution is expressed as:

$$N(D_i)=\frac{N_t}{\sigma\sqrt{2\pi}}\exp\frac{-(\ln(D_i)-\mu_i)^2}{2\sigma_i^2} \tag{1}$$

whereN_t is the scattering point diameter density. The independent input, D_i the mean diameter of the scattering point which can be obtained directly from measurement. The input parameters $N_t, \mu,$ and σ are obtained by regression fitting procedures to yield:

$$\begin{aligned} N_T &= a_o R^{b_o} \\ \mu_{\ln} &= A_\mu + B_\mu \ln R, \\ \sigma_{\ln}^2 &= A_\sigma + B_\sigma \ln R, \end{aligned} \tag{2}$$

where $a_o, b_o, A_\mu, B_\mu, A_\sigma$ and B_σ all represent the regression coefficients of input parameters corresponding to the lognormal distribution, using the MoM. They were presented as [8];

$$\begin{aligned} N_T &= 544.4R^{0.1145} \\ \mu_{\ln} &= -0.6369+0.298\ln R, \\ \sigma_{\ln}^2 &= 0.2887-0.041\ln R, \end{aligned} \tag{3}$$

3. Reflectivity

Mie scattering is applied in this approach to determine the radar reflectivity. The backscattering coefficient Q_b is integrated over the drop size distribution $N(D)$as suggested in [8], which leads to the radar reflectivity given by [9,10]:

$$\eta = \int_0^{N_{max}} Q_b(D)N(D)dD \quad (mm^2 mm^{-3}) \tag{4}$$

The backscattering coefficient computations are performed under Mie theory. Fig. 1 shows the backscattering coefficient of spherical raindrops as function of raindrop diameter and signal incidences for 19.5, 60 and 140 GHz frequencies.

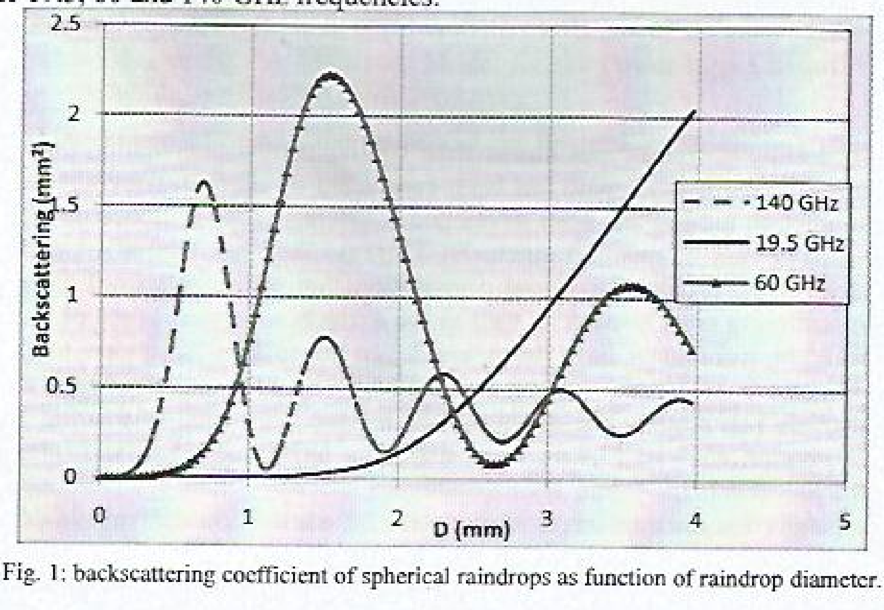

Fig. 1: backscattering coefficient of spherical raindrops as function of raindrop diameter.

The exponential characteristic of the Q_b is observed for the entire raindrop range and the characteristic oscillations of resonance backscattering are also observe at for $D > 0.6\,mm$ at 140 GHz and $D > 1.5\,mm$ at 60 GHz.

According to Laws and Parsons [11, 12], a very large fraction of raindrops are larger than 0.5 mm at rainfall intensities $R \geq 2.5\,mm/h$. Therefore based on the scattering matrixby Bohren and Huffman [13], the angular diagrams for Mie scattering on raindrops at 19.5 GHz, T = 293 ^0K in Ibadan will appear as shown in Fig.2. Mie scattering intensities $|S_1|^2$ and $|S_2|^2$ as a function of $\cos\theta$, and the result as a polar diagram of θ on the upper part of the curves ($0 < \theta < \pi$) are for polarization perpendicular to the scattering plane. The lower part of the curves ($\pi < \theta < 2\pi$) are for polarization parallel to the scattering plane, and both functions are symmetric with respect to two half circles.

For raindrop diameter equal to 1 mm there is little change in intensity with angle in the upper part while the lower part strongly changes and reaches the maximum at 0 ^0C. For a diameter equal to 3 mm or size parameter ($x = ka$), equal 0.63, scattering in the backward hemisphere is much larger than in the forward hemisphere. Although a diameter equal to *4 mm* or size parameter ($x = ka$) equal 0.84, $|S_1|^2$ and $|S_2|^2$ have large amplitudes in backward direction at $\theta = \pi$. At diameter equal to 6 mm or size parameter ($x = ka$) equal to 1.26, $|S_1|^2$ and $|S_2|^2$ have much larger amplitudes in the forward direction at $\theta = 0$.

The Mie backscattering efficiency variation with raindrop size, Q_b (Fig.1) shows different maxima according to raindrop diameter. While the monostatic radar signal from rain is not directly influenced by the changing diagram, the modeling of microwave transmission signals depends on the angular diagram, i.e. on the phase function [Ishimaru, 1978].

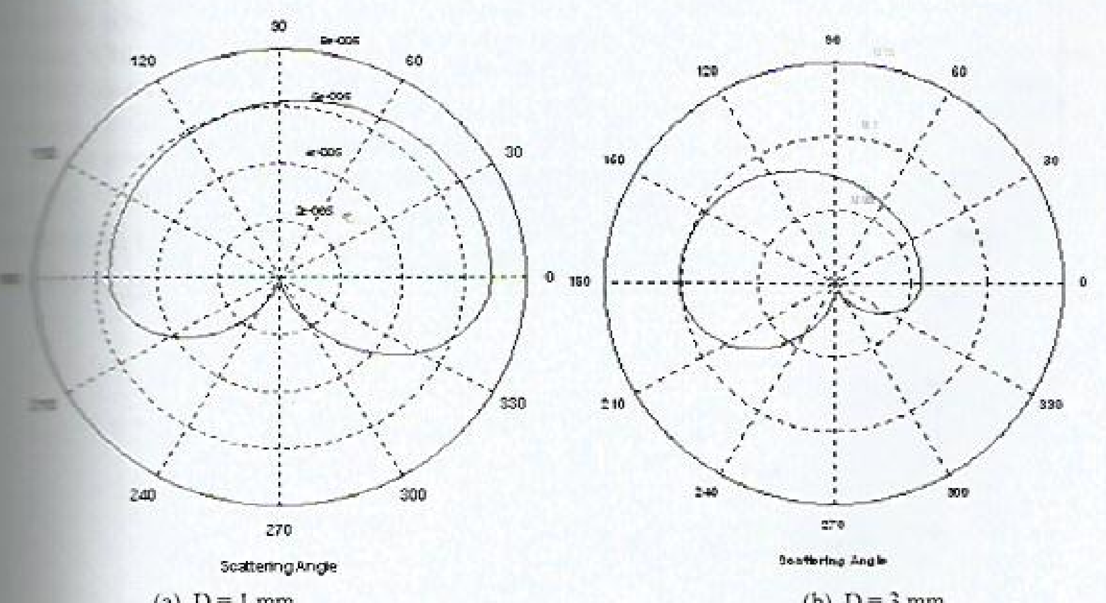

(a) D = 1 mm

(b) D = 3 mm

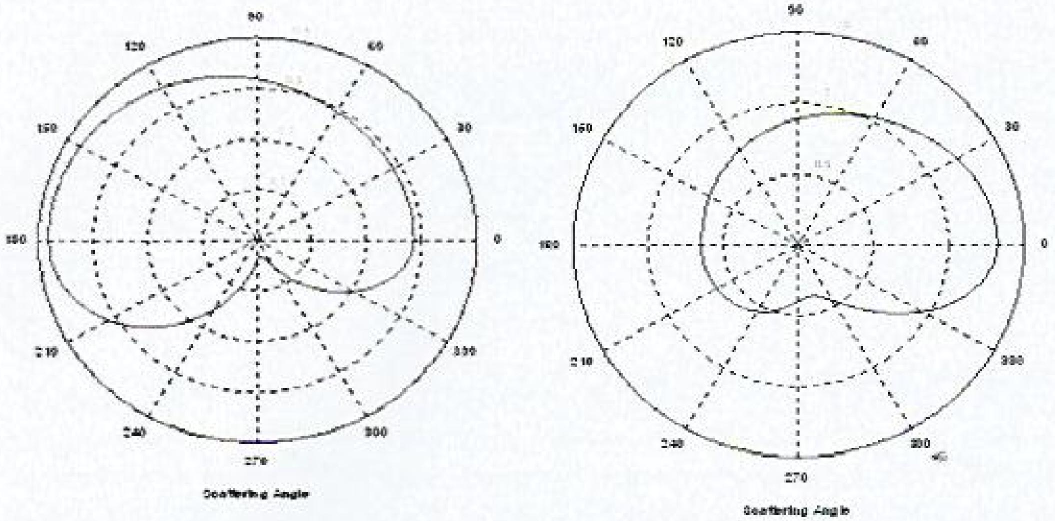

(c) D = 4 mm (d) D = 6 mm

Fig.2 a, b, c, d: Polar plots for magnitudes of Mie scattering on raindrops at f=19.5 GHz, T= 293K for different diameters.

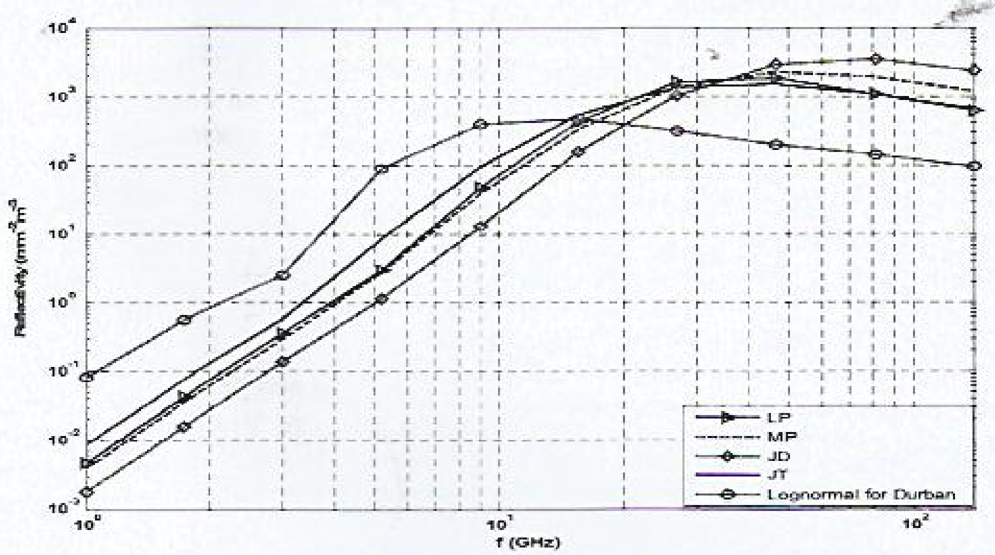

Fig. 3: Reflectivity at rain rate 5 mm/h

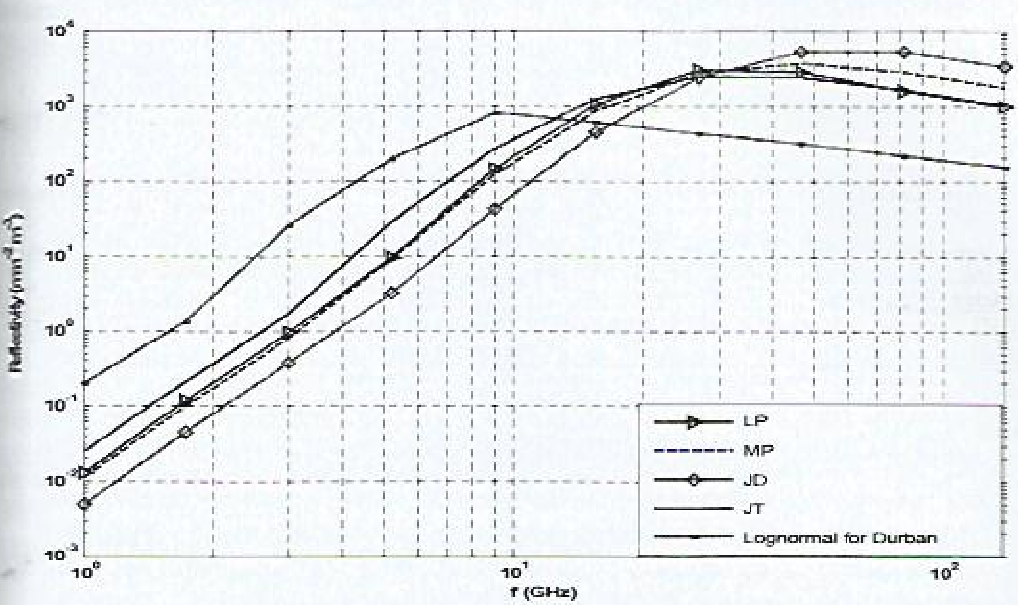

Fig. 4: Reflectivity at rain rate 120 mm/h

The reflectivity in equation (4) is calculated using Durban lognormal distribution and Mie theory as shows in Figure 3-4 and compared with MP, JD, JT and LP drop size distributions. The results show that MP, JD, JT and LP drop size distributions underestimated the reflectivity at the frequencies below 15 GHz and overestimated the values of reflectivity at frequencies above 15 GHz.

Fig. 5 shows reflectivity as a function of rainfall rate obtained using the lognormal drop size distribution (DSD) for 19, 60 and 140 GHz frequencies. The reflectivity at 19.5 GHz is greater than at 60 and 140 GHz for the entire rainfall rate range. This can be explained by observing the reflectivity as a function of frequencies (Fig. 3). For lognormal Durban distribution, after attaining a pick about 10 GHz, the reflectivity is decreasing while the frequency is increasing. As results, η at 19.5 GHz is greater than η at 60 and 140 GHz. It is can also be explain from Fig.1. For the raindrop bigger that 1.5 mm Q_b at 60 GHz is greater than Q_b at 140 GHz, also, at $D > 3mm$, Q_b at 19.5 GHz is greater than Q_b at 140 GHz. These observations mean that there are more contributions for radar reflectivity of bigger raindrops at lower frequencies.

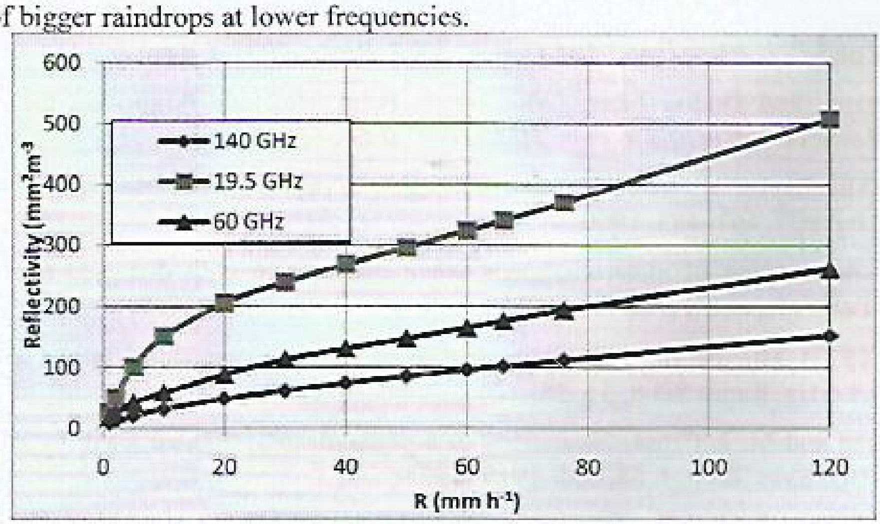

Fig. 5 Radar reflectivity as a function of rainfall rate using the Durban lognormal drop size distribution

4. Power Law Model

In order to estimate radar reflectivity (η), we employ an empirical scaling relationship expressed as:

$$\eta = \alpha R^{\beta} \tag{5}$$

where α and β are coefficients to be determined and R is the rainrate.

The obtained results of the parameters α and β are shown in Table 1. It has been observed that the fitted model has a high coefficient of goodness (R^2) indicating a good fit to proposed model.

Table 1: Power law relaship between Radar Reflectivity and rainrate obtained using Durban lognormal raindrop distribution for spherical model.

F (GHz)	α	β	R^2
19.5 GHz	33.802	0.5677	0.981
60 GHz	16.721	0.5624	0.9988
120 GHz	8.269	0.5624	0.999

5. Conclusion

In this study, radar reflectivity is calculated using Durban lognormal distribution and Mie theory and compared with MP, JD, JT and LP drop size distributions. The results show that MP, JD, JT and LP drop size distributions underestimated the reflectivity at the frequencies below 15 GHz and overestimated the values of reflectivity at frequencies above 25 GHz. It was also observed that the reflectivity at 19.5 GHz is greater than at 60 and 140 GHz for the entire rainrate range. This can be explained by observing the reflectivity as a function of frequencies. For lognormal Durban distribution, after attaining a pick about 10 GHz, the reflectivity is decreasing while the frequency is increasing. As results, η at 19.5 GHz is greater than η at 60 and 140 GHz. Finally, the empirical scaling relationship has be employed for practical engineering application to estimate the parameters in order to predict radar reflectivity. For rainfall intensity above about 10 mm/h, the diameters of raindrops are in the order of the wavelength, so backscattering is predominantly due to Mie scattering law where the average backscattering cross section depends weakly on raindrop diameter. Since the raindrop diameter D appears as the sixth power, it follows that in any raindrop size distribution, the small number of large drops will contribute the largest amount of received echo power of the rain. Then there is a reduction of the signal-to-noise ratio and the radar can lose the target.

References

[1] Zhao Zhenwei , Lin Leke and Liu Yumei, "A prediction model of Rain attenuation along Earth-space path ", *IEEE, AP and EM Theory, 2003. Procs. 2003*, China.

[2] Dirk Klugmann, and Ondrej Fiser, "Mie versus Point Matching Algorithm for Radar Rain Properties Retrieval", *IGARSS 4, page 1002-1005. IEEE, (2008)*.

[3] Oguchi T., Attenuation of electromagnetic wave due to rain with distorted raindrops. J. Radio Res. Labs. (Japan)7, 467–485, 1960.

[4] Oguchi, T., Attenuation of electromagnetic wave due to rain with distorted raindrops, 2, J. Radio Res. Labs. (Japan), 11, 19–44, 1964.

[5] Oguchi T. (1973) Attenuation and phase rotation of radio waves due to rain: Calculations at 19.3 and 34.8 GHz. Radio Sci.8, 31–38.

[6] J. A. Morrison and M. J. Cross, "Scattering of a plane electromagnetic wave by axisymmetric raindrops," Bell Syst. Tech. J. 53, 995–1019 (1974).

[7] Holt, A. R., N. K. Uzunoglu, B. G. Evans, An integral equation solution to the scattering of electromagnetic radiation by dielectric spheroids and ellipsoids, *IEEE Trans. Antennas Propag.*, AP-265, 706–712, 1978.

[8] T. J. O. Afullo, "Raindrop Size Distribution Modeling For Radio Link Design Along The Eastern Coast Of South Africa," *Progress In Electromagnetics Research B*, Vol. 34, 345{366, 2011.

[9] Aydin K. and Y. Lure, "Millimeter wave scattering and propagation," *Radio Sci.*, 34:1103-1124, 1991.

[10] Mulangu C. T., Malinga S. J. and Afullo, T. J. O. "Impact of Rain on Microwave Radars", ICEAA, IEEE APWC, EEIS, Cape Town, South Africa, 2-7 September 2012.

[11] Mulangu,C.T., and T.J. Afullo, Effet of Rain on Microwave Remote Sensing Systems and Ground-Based Radars Use in Durban, *Proceedings of SATNAC*, ISBN No. 978-0-620-41696-2, Eastern Cape, South Africa, pp. 53-58, 2008.

[12] Alfred, J., and J. Bogush, *Radar and the Atmosphere*, Artech House, Inc., MA, 1989.

[13] Bohren, C.F., and D.R. Huffman, *Absorption and Scattering of Light by Small Particles,* John Wiley: New York, NY, 1983.

[14] Ishimaru, A. , Wave Propagation and Scattering in Random Media, *volume 1 and 2. Academic Press*, New York, 1978.

Information Engineering Letters, ISSN: 2163-4114
Volume 3, Number 3, September, 2013

A Tablet based Hands Free Interface to Nurse Communication in the Standard Hospital Room for Limited Mobility Patients

Kimberly E. Newman[1, a], Elisa Hobbs[2,b] and Michael Blei[3,c]

[1]ORISE Fellow, Functional Performance and Device Use Laboratory, Food and Drug Administration

Assistant Professor Adj., Electrical, Computer, and Energy Engineering, University of Colorado Boulder, USA

[2]Discovery Learning Apprentice, Computer Science, University of Colorado Boulder , USA

[3]Associate Professor, University of Colorado, Chief of Rehabilitative Services, Denver Health Medical Center, USA

[a]Kimberly.Newman@colorado.edu, [b]Elisa.Hobbs@colorado.edu, [c]Michael.Blei@dhha.org

doi.10.5729/iel.vol3.issue3.50

Keywords: Remote control hospital room interface, Tablet based interface, Instant messaging, Camera based facial tracking.

Abstract. The goal of this project is to integrate off-the-shelf devices into a tablet for remote control of the standard hospital room environment by individuals with limited mobility. The standard hospital room interface for control of communication and entertainment devices assumes a patient has the ability to hold and press mechanical switches. If the patient does not have these abilities, then the patient must wait for a nurse to walk by the room to ask for help. A mobile device with an adaptable user input device that accommodates the limitations of a patient removes access barriers to communicate and control the hospital room environment.

1. Introduction

There is a significant population of acutely hospitalized patients that lack the functional capacity to effectively utilize standard hospital room communication and local environmental controls. In 2007, the three leading mechanisms of injury in the US are falls, struck by or against accidents and motor vehicle traffic [1]. Five categories are listed that include fractures, contusions and superficial injuries, sprains and strains, open wounds, and other injuries. Many of these injuries are combined into what is called a polytrauma event where mobility is limited in the short term while healing and potentially long term due to paralysis [2].

As individuals progress through the care process from the ICU to the step-down and eventually to the standard hospital room, the ability and desire to communicate changes. However, the interfaces for communication as well as control of the local environment are not customized and may be inaccessible. If a patient is sent to a rehabilitation hospital, the potential for interaction with engineer who will fit an interface to the individual is likely but this is not the case in the standard room.

In order to instill confidence in the patient and have them actively engage in the healing process, a remotely controlled system that allows for control of environmental parameters, entertainment systems as well as communication with care providers and a social network is necessary for the well-being and quality of life of the patient to reduce the risk of dissonance and depression [3][4].

A system that can automate these tasks for individuals has the potential to improve patient satisfaction with care as well as shorten the duration of stay. An initial PC based solution was developed through support from the National Science Foundation as a proof of concept and was evaluated using the COGTOOL user simulation tool [5]. However, the cost of implementation of this solution at 2,000 – 3,000 dollars per unit was prohibitive.

Light weight mobile devices with Bluetooth and Wi-Fi connectivity provide a more cost effective solution. Devices of this type with the appropriate room interfaces can be used to create a solution in the 1,000 – 1,500 dollar range for off-the-shelf components.

2. Background and Significance

Over the last year, the leading options for the system described above were evaluated in the Functional Performance and Device Usability (FPDU) laboratory at the FDA and a Discovery Learning Apprentice at CU Boulder investigated software for implementation a facial feature tracker on an Android tablet. This system is a continuation of an initial prototype that was a Windows based system created through a Research to Aid Persons with Disabilities grant from the National Science Foundation [6].

The evaluation of solutions for a tablet based implementation is based on analysis of the overlapping constraints of the patient with activity limitations, the patient care environment, and off-the-shelf devices available for communication and control. An optimal solution should address the limitations of the patient, fit within the constraints of the patient care environment, and be an off-the-shelf (OTS) solution for communication and control. This solution fits within the intersection of all three circles as shown in Fig. 1 and provides an adaptable communication system.

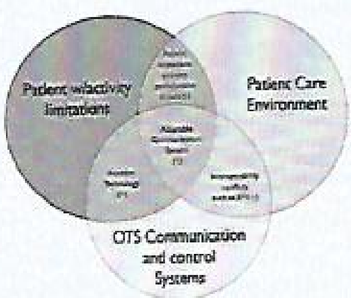

Figure 1. Domain of interest for smart hospital room

In order for this to provide a solution that will benefit the patient a discussion of human factors as it relates to medical devices is appropriate.

3. Human Factors for Medical Devices

The top three considerations from the Human Factors (HF) guidance [7] for the development of medical devices are shown in Fig 2. Proper understanding and incorporation of users needs, customization to the use environment, and adoption of accessible interfaces in the device create a scenario for device use that leads to safe and effective solutions. Hazards emerge when device use is inconsistent with expectations or intuition as well as when devices are used in ways that are inappropriate and for which adequate controls are not applied.

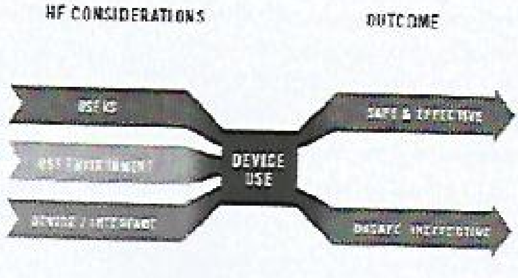

Figure 2. Interactions among Human Factors (HF) and usability engineering (UE) considerations resulting in either safe and effective use or unsafe or ineffective use.

In the context of the users of the smart room, individuals with limited mobility require a solution that does not require them to lift or press a button with significant force. Device use should not require physical, perceptual, or cognitive abilities that exceed the ability of the user. For example, there are off-the-shelf mounting brackets that can be purchased for mounting near the bed to alleviate this limitation. Additionally, the selection of a touch screen for patient interaction does not require significant force to be applied and can be adapted to other methods of interfacing based on the mobility of the patient.

The use environment of the system is a hospital room so it is important to incorporate the needs of the patient and the care providers into the creation of a solution. The system configuration on a tablet controls a reading lamp, television, and fan. Interfaces are provided through apps that communication with wireless devices through IR, bluetooth, and Wi-Fi. Setup and use of these external devices should be intuitive to the care providers and easily maintained in the hospital room. Interoperability with other medical devices is necessary to reduce hazards. The guidance from the FDA for evaluation of the wireless footprint provides methods for analysis of communication links [8]. The bluetooth and Wi-Fi signals are operating in the ISM band so there is potential for interference in a hospital setting if these devices are not properly characterized and controlled by the smart phone. IR communication is used in some medical devices such as infusion pumps so it is important to block in appropriate access.

4. Nurse Communication Systems

The focus of this paper is on the implementation of a nurse communication system that uses instant messaging clients from the hospital room to the nursing station. The nurse call interface utilized in this study is part of a patient room control interface that is used to send requests to the nursing station. These devices are typically wired into the wall of the room through a bed user interface (BUI) that connects to the hospital system at a central location. A patient must be able to hold the device and press a button which makes access difficult for individuals with limited mobility.

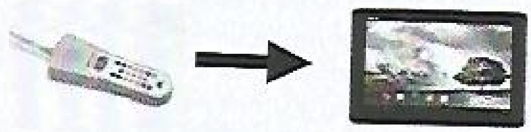

Figure 3. Transition from handheld room control to tablet with option for hands free user access

As shown in Fig. 3, the tablet can be used to replace the buttons and can also be mounted near the hospital bed to enable hands free use with tracking of facial features with the integrated front facing camera.

5. Tablet Based Solution

The solution proposed for hands free operation involves the creation of a hands free interface to a tablet device with wireless interfaces to the devices in the room. The new control unit can be mounted on a stand near the hospital bed for access by a limited mobility patient. This application to the hospital environment complements the study recently published by Hreha and Snowdon for enhanced access to cell phones for individuals with spinal cord injury [9]. These researchers studied the current accessibility options for several cell phones and determine they were lacking for individuals who required hand free interfaces.

Our approach is to use the emerging support for facial tracking on smart phones to create a mouse interface that can be used to select applications and enter information for communication. This is similar to the camera mouse that works on Windows based computers developed by James Gips for limited mobility access [10]. However, our approach is implemented in the Android Operating System [11]. The new contribution to the smart room system capabilities is the incorporation of open source instant messaging software that runs on the Android OS as well as the Open Computer Vision libraries for feature detection and tracking [12]. For the nurse communication system, we are evaluating open source XMPP based server client configurations [13] otherwise known at Jabber. This is described in the following section along with the current progress on the facial tracking mouse interface.

6. Open Source Instant Messaging

There are a variety of servers and clients applications that allow the configuration of interfaces to XMPP format. The ones selected for this evaluation were on the list provided by the XMPP Standards Foundation [14] and were compatible with the OS used for the evaluation.

The server that was very easy to configure is Openfire and it works on Windows as well as Mountain Lion for Apple [15]. My configuration is using the internal database on the Mountain Lion OS. For evaluation purposes the server can be setup for local access on the network. This provides additional security for the patient communication since it is not transmitted outside of the LAN.

Initial testing can be performed on the same machine to show proof of concept. The Macbook Pro with Mountain Lion OS comes with an instant messenger application called Messages [16] that can be configured to use the XMPP server. I made the following users for testing: fluffyhen@kims-macbook-pro.local is using Messages which is installed as a default application; rml202@kims-macbook-pro.local is using Adium [17]; and mobiletest@kims-macbook-pro.local is using Spark [18] on a Windows 7 computer. The dialog boxes for message exchange are shown in Figure 4.

In order to connect to the server using Spark it is necessary to write down the IP address which can be found in the network settings. The Windows computer is on the same local area network as the Apple computer so it can find the server and communicate.

One observation during the initial testing is the variability in the user interface from client to client. For individuals with limited mobility is it is beneficial to have controls that are easy to select by hovering over the icon so that dwell time clicking can be used.

Additionally, a keyboard interface that can be controlled on the screen is necessary since typing on the computer is not possible. The ability to send images is also helpful to express needs in a rapid manner.

There are mobile apps that can also connect to the Openfire server. The one that I am currently using for testing on the tablet is Jabiru [19]. Voice control is supported on this IM client so this makes it much easier to enter a custom request.

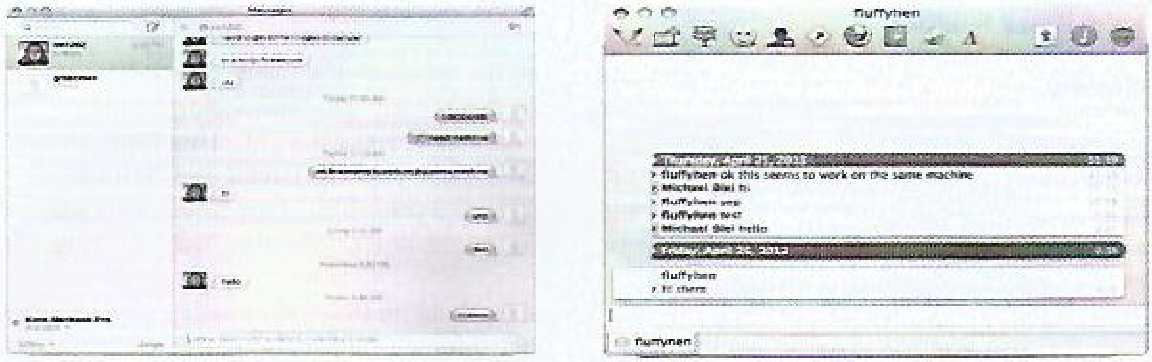

(a) (b)

Figure 4. Chat windows for testing of server interfaces (a) Messages chat window instant messenger (IM) on Apple (b) Adium chat window IM on Apple – downloaded and installed to communicate on local machine for testing.

7. OpenCV Facial Tracking

The integration of facial recognition into smart phones for facial recognition is already occurring and shows the potential for use of facial features tracking for a remote control interface. The sample projects for OpenCV 2.4.2 support facial tracking on the Android operating system and can be implemented after configuration of the programming environment to run the native code. Changing from the rear facing to front facing camera requires a slight modification to the code. There is also an issue with mirroring of the image that requires the use of an 3x3 Eigenmatrix. The sample program has a limitation in the frames per second (FPS) as well as the ability to detect faces at angles. Performance is also very slow in the 2-5 FPS range. The sensitivity to the tilt angle of the face is also variable as shown in Fig. 5. The loss of the tracking is shown below in Fig. 5(a) and it picks up again in Fig. 5(b). Angles are basically the same offset from center but the detector is more sensitive to the tilt toward the camera than away from the camera.

(a) (b)

Figure 5. Face tracking using OpenCV on the front facing camera of a smart phone. (a) Image is lost due to the tilt of the head. (b) Image is captured but lost if the angle is increased beyond this point.

8. Next Steps for System Design

Version 2.4.4 of OpenCV has new algorithms with faster FPS and there is also support for eye tracking. Demo code was found and implemented on the front facing camera with mirror cancellation. Further evaluation of the code is required before statements can be made. Additional tasks to complete this portion of the system configuration are listed as follows:

- Implementation of pose estimation for the face that allows a greater angle of tilt
- Implementation of a mouse pointer
- Incorporation of icon based menu into an IM for selection of urgent needs.

9. Conclusion

A system that uses open source software to enable limited mobility patients to access the nurse communication systems in a standard hospital room is described. Implementation of the system is described and analysis is performed on the capabilities of the interfaces from a human factors perspective. Information is provided for evaluation of the safety and effectiveness of these interfaces from a regulatory perspective. This work is still in the early stages but it does demonstrate the capability of smart phones and tablets to implement a hands free interface for communication in the hospital environment.

10. Acknowledgment

The effort of Kimberly Newman was supported through an ORISE Fellowship at the FDA. The effort of Lisa Hobbs was supported through NSF REU stipend number 1229929 for her appointment as a Discovery Learning Apprentice at CU Boulder.

11. Disclaimer

The mention of commercial products, their sources, or their use in connection with material reported herein is not to be construed as either an actual or implied endorsement of such products by the Department of Health and Human Services.

References

[1] Injury in the United States: 2007 Chartbook, U.S. Department of Health and Human Services, Centers for Disease Control and Prevention, National Center for Health Statistics.

[2] Strasser, D.C., Uomoto, J.M., Smits, S.J. The Interdisciplinary Team and Polytrauma Rehabilitation: Prescription for Partnership. Archives of Physical Medicine and Rehabilitation, 89, 1 (2008), 179-181.

[3] Friedemann-Sánchez, G., Sayer, N.A., Pickett, T. Provider Perspectives on Rehabilitation of Patients with Polytrauma. Archives of Physical Medicine and Rehabilitation, 89, 1, (2008), 171-178.

[4] Jha, A.K., Oray, J., Zheng, J., and Epstein, A.M. Patient's Perception of Hospital Care in the United States. The New England Journal of Medicine, 359, (2008), 1921-31.

[5] Agyei-Ntim, F., Shah, T., Mudugal, S., Osadebe, T., and Newman, K. System Configuration and Simulated User Evaluation of enRICH. In Second International Symposium on Quality of Life Technology, (2010).

[6] Newman, K.E., Osadebe, T., Al-Khalidi, K., Zawawi, A., and Tanaka, M.,enRICH: A Remote Controlled Hospital Room Interface for Limited Mobility Patients. In First AMA-IEEE conference on Individualized Medicine (2010).

[7] Draft Guidance for Industry and Food and Drug Administration Staff: Applying Human Factors and Usability Engineering to Optimize Medical Device Design. http://www.fda.gov/downloads/MedicalDevices/DeviceRegulationandGuidance/GuidanceDocuments/UCM259760.pdf

[8] Guidance for Industry: Wireless Medical Telemetry Risk and Recommendations, http://www.fda.gov/downloads/MedicalDevices/DeviceRegulationandGuidance/GuidanceDocuments/ucm070921.pdf

[9] Hreha, K., Snowdon, L., We All Can Call: Enhancing Accessible Cell Phone Usage for Clients With Spinal Cord Injury. Assistive Technology: The Official Journal of RESNA, 23, 2 (2011) 76-80.

[10] Betke, M., Gips, J., Fleming, P., The Camera Mouse: Visual Tracking of Body Features to Provide Computer Access for People with Severe Disabilities. IEEE Transactions on Neural Systems and Rehabilitation Engineering, 10, 1 (2002) 1-10.

[11] Android Developers. http://developer/android.com/index.html

[12] Every, S.V. Pro Android Media: Developing Graphics, Music, Video, and Rich Media Apps for Smartphones and Tablets. Apress, USA, 2009.

[13] Saint-Andre, P., Smith, K., TronCon, R., XMPP: The Definitive Guide: Building Real-Time Applications with Jabber Technologies.O-Reilly Media, Inc,, Sebastopol, CA, 2009.

[14] XMPP Standards Foundation. http://xmpp.org/

[15] Ignite Realtime Openfire server. http://www.igniterealtime.org/projects/openfire/

[16] Apple OS X Mountain Lion – Messages. http://www.apple.com/osx/whats-new/

[17] Adium IM download http://adium.im/

[18] Spark IM client for Openfire http://www.igniterealtime.org/projects/spark/

[19] Jabiru IM client for Android https://play.google.com/store/apps/details?id=net.mzet.jabiru&hl=en

Information Engineering Letters, ISSN: **2163-4114**
Volume **3**, Number **3**, September, **2013**

Full Band Recursive Digital Integrators and Differentiators

DHARMENDRA Kumar Upadhyay

Division of ECE, NSIT, Sector-3, Dwarka, New Delhi, India

upadhyay_d@rediffmail.com

doi.10.5729/iel.vol3.issue3.57

Keywords: Digital differentiator, Digital integrator, Full band, Linear phase, Pole-zero optimization, Recursive.

Abstract. In this paper, firstly a general transfer function is defined to include a suitable pole-zero pair in the transfer function of existing recursive digital integrator. Then a new recursive digital integrator is obtained by optimizing the pole-zero locations of defined transfer function using linear programming approach. Thereafter, a new recursive digital differentiator is designed by inverting the transfer function of proposed minimum phase digital integrator. Now, the zero-reflection approach is applied over the transfer functions of proposed digital integrator and differentiator to obtain the suitable phase responses. The beauty of all proposed recursive digital integrators and differentiators is that they have maximum percentage relative errors of 0.38% in magnitude responses over the full Nyquist band (including $\omega = 0$ and $\omega = \pi$) with the ideal ones and also provide the choice of suitable phase response. Therefore, the proposed designs are more useful in real time applications.

1. Introduction

The digital integrators are used to determine the time integrals of discrete-time signals, while the digital differentiators are used to determine the time derivatives of discrete-time signals. These systems have several applications in the fields of speech processing, image processing, bio-medical engineering, radar engineering, control systems etc. The frequency response of an ideal integrator is given by $1/j\omega$ and that of a differentiator is given by $j\omega$, where ω is the angular frequency in radians per second.

Initially, a series resistor-capacitor circuit is used as an integrator or differentiator system for continuous-time signals. Further, these circuits in conjunction with operational amplifiers are developed to design integrator or differentiator system of more bandwidth [1]. Later, several techniques have been evolved to design digital integrators and differentiators by using recursive or non-recursive systems, which are helpful in obtaining good accuracy over improved bandwidth. In general, the recursive digital differentiators are obtained by inverting the transfer functions of derived recursive digital integrators with suitable modifications [2]. Initially, the recursive digital integrators have been derived by performing a linear interpolation between the magnitude responses of classical recursive digital integrators [3-6]. Further, a linear programming optimization technique has developed to design recursive digital integrators [7]. Thereafter, Ngo has designed the full band digital integrator and differentiator using third-order recursive systems, which are based on Newton-Cotes integration rule [8]. These designs have no more than 4.6% relative error in magnitude responses over the full Nyquist band (including $\omega = 0$ and $\omega = \pi$) with the ideal ones. It is interesting to note that Ngo integrator and differentiator have maximum absolute phase errors (MAPEs) of 39.4^0 and 12.2^0 in phase responses over the full Nyquist band with the ideal linear phase responses. Further, Gupta-Jain-Kumar (GJK) have obtained the recursive digital integrator and differentiator of third-order systems for maximum percentage relative errors (MPREs) of 3.16% in magnitude responses over the full Nyquist band with the ideal ones [9]. The GJK integrator and differentiator have MAPEs of 35.3^0 and 12^0 in phase responses over the full Nyquist band with the ideal linear phase responses. Thereafter, Upadhyay has proposed recursive digital differentiators of second-order systems for MPREs of 2% in magnitude responses with the ideal one over the full Nyquist band except the Nyquist frequency near to $\omega = 0$ [10].

In recent developments, Al-Alaoui has designed a class of recursive digital integrators and differentiators by applying the interpolation and simulated annealing optimization technique [11]. Further, Upadhyay-Singh (US) have designed the recursive digital integrator and differentiator by optimizing the pole-zero locations of existing recursive digital differentiator [12]. These designs have no more than 0.48% relative errors in magnitude responses with the ideal ones over the Nyquist frequency range of $0 \le \omega \le 0.94\pi$. Thereafter, Jain-Gupta-Jain (JGJ) have proposed recursive digital integrator and differentiator designs for MPREs of 0.3% in magnitude responses with the ideal ones over the Nyquist frequency range of $0 \le \omega \le 0.95\pi$ [13]. Later, a class of recursive digital integrators and differentiators has obtained by applying the coefficients and pole-zero optimizations over a generalized fourth-order recursive digital filter [14]. These designs are useful according to the importance of accuracy, phase linearity and the system bandwidth.

It is observed that the US [12] and JGJ [13] designs of second-order systems have almost 4.2% and 3.5% relative errors in magnitude responses near to $\omega = \pi$. Moreover, it is observed that the JGJ designs have large amount of relative errors in magnitude responses with the ideal ones near to $\omega = 0$. It can be easily seen that the recently published Upadhyay digital integrator and differentiator of fourth-order systems have almost 10% relative errors in magnitude responses near to $\omega = \pi$ [14]. However, these designs have MPREs of only 0.048% in magnitude responses with the ideal ones over the frequency range of $0 \le \omega \le 0.84\pi$. These observations clear that the recently published US [12], JGJ [13] and Upadhyay [14] designs are not useful for higher band applications. Moreover, JGJ designs are not useful for extremely lower band applications (near to $\omega = 0$). Therefore, there is the need to design recursive digital integrator and differentiator, which can accurately approximate the ideal ones over the full Nyquist band (including the extremes $\omega = 0$ and $\omega = \pi$).

In this paper, new recursive digital integrator and differentiator of third-order systems are proposed for MPREs of 0.38% in magnitude responses over the full Nyquist band with the ideal ones. Further, the zero-reflection approach is used to obtain the choice of suitable phase response.

2. Full Band Recursive Digital Integrators and Differentiators

Recently, Jain-Gupta-Jain (JGJ) have designed the recursive digital integrator of second-order system by applying the Genetic Algorithm optimization technique [13]. The transfer function of JGJ integrator is given below in factorized form.

$$H_{ji}(z) = \frac{T(0.8647)(z+0.1066)(z+0.5871)}{(z-0.997)(z+0.5158)}. \quad (1)$$

It is observed that the magnitude response of JGJ digital integrator $H_{ji}(z)$ has large amount of relative error near to $\omega = 0$ and almost 3.5% relative error near to $\omega = \pi$ in magnitude response with the ideal integrator. These observations clear that the JGJ integrator is not useful for extremely lower band and as well as for higher band applications. These limitations of JGJ integrator may be overcome by applying the following steps:

Step I. It can be easily seen that the digital integrator should have at least one pole exactly at $z = 1$ to satisfy the magnitude requirement of an ideal integrator at $\omega = 0$ as in [8, 9, 12]. However, the JGJ [13] integrator $H_{ji}(z)$ has one out of two poles at $z = 0.997$ i.e., nearer to unity. Hence, the location of this pole may be shifted to exactly at $z=1$ for obtaining ideal magnitude at $\omega=0$. The transfer function of recursive system thus obtained is given in Eq. (2).

$$H_{mi}(z)=\frac{T(0.8647)(z+0.1066)(z+0.5871)}{(z-1)(z+0.5158)}. \tag{2}$$

Step II. Now the aim is to modify the transfer function $H_{mi}(z)$ i.e., given in (2) in such a way, so that the modified transfer function should satisfy the magnitude requirement of an ideal integrator at $\omega=0$ and $\omega=\pi$ with maintaining the merits of JGJ integrator [13]. Firstly, it is computed that the magnitude of $H_{mi}(z)$ is 0.3294 at $\omega=\pi$. However, the magnitude of an ideal integrator should be $1/\pi$ or 0.3183 at $\omega=\pi$. Therefore, the transfer function $H_{mi}(z)$ is modified to include an additional pole-zero pair in such a way, so that the magnitude of resultant general transfer function should always be $1/\pi$ at $\omega=\pi$. The realizable and stable transfer function is defined in Eq. (3), which satisfies the magnitude requirements of an ideal integrator at both extremes $\omega=0$ and $\omega=\pi$ for any real pole location $z=\alpha$ $(-1\le\alpha\le 1)$.

$$H(z)=\frac{T(0.8647)(z+0.1066)(z+0.5871)\left(z+1-\dfrac{(1+\alpha)}{(0.3294\pi)}\right)}{(z-1)(z+0.5158)(z-\alpha)}. \tag{3}$$

Step III. Finally, the magnitude response of H(z) i.e., defined in Eq. (3) is optimized to minimize the maximum percentage relative error (PRE) over the full Nyquist band by using α as an optimization parameter with suitable scaling. This optimization is based on the linear programming approach [7]. The PRE is defined in Eq. (4) as in [8, 9, 10, 12, 13, 14]. The result of such optimization is that the $\alpha=-0.9445$ accurately approximate an ideal integrator over the full Nyquist band (including extremes $\omega=0$ and $\omega=\pi$). The transfer function of recursive digital integrator thus obtained is given in Eq. (5).

$$PRE=100\times\frac{\left|(1/\omega)-\left|H(e^{j\omega})\right|\right|}{(1/\omega)}. \tag{4}$$

$$H_{i1}(z)=\frac{T(0.8655)(z+0.1066)(z+0.5871)(z+0.9464)}{(z-1)(z+0.5158)(z+0.9445)}. \tag{5}$$

It is noticed that the designed recursive digital integrator $H_{i1}(z)$ i.e., given in (5) has three non-unity real zeros. Therefore, seven other integrator designs are obtained by reflecting one or more zeros of $H_{i1}(z)$ as in [14]. These additional designs have same magnitude responses as of the original design $H_{i1}(z)$ but having the different phase responses. The transfer functions of recursive digital integrators thus obtained are given in Eqs. (6)-(12):

$$H_{i2}(z)=\frac{T(0.0923)(z+9.381)(z+0.5871)(z+0.9464)}{(z-1)(z+0.5158)(z+0.9445)}. \tag{6}$$

$$H_{i3}(z)=\frac{T(0.5081)(z+0.1066)(z+1.7033)(z+0.9464)}{(z-1)(z+0.5158)(z+0.9445)}. \tag{7}$$

$$H_{i4}(z)=\frac{T(0.8191)(z+0.1066)(z+0.5871)(z+1.0566)}{(z-1)(z+0.5158)(z+0.9445)}. \quad (8)$$

$$H_{i5}(z)=\frac{T(0.0542)(z+9.381)(z+1.7033)(z+0.9464)}{(z-1)(z+0.5158)(z+0.9445)}. \quad (9)$$

$$H_{i6}(z)=\frac{T(0.481)(z+0.1066)(z+1.7033)(z+1.0566)}{(z-1)(z+0.5158)(z+0.9445)}. \quad (10)$$

$$H_{i7}(z)=\frac{T(0.0873)(z+9.381)(z+0.5871)(z+1.0566)}{(z-1)(z+0.5158)(z+0.9445)}. \quad (11)$$

$$H_{i8}(z)=\frac{T(0.0513)(z+9.381)(z+1.7033)(z+1.0566)}{(z-1)(z+0.5158)(z+0.9445)}. \quad (12)$$

The transfer function of proposed recursive digital integrator $H_{i1}(z)$ i.e., given in Eq. (5) has all zeros inside the unit circle. It signifies that the design $H_{i1}(z)$ satisfies the minimum phase criterion. Therefore, the transfer function of corresponding recursive digital differentiator is obtained by inverting the transfer function of minimum phase design $H_{i1}(z)$. The transfer function of recursive digital differentiator thus obtained is given in Eq. (13).

$$H_{d1}(z)=\frac{(z-1)(z+0.5158)(z+0.9445)}{T(0.8655)(z+0.1066)(z+0.5871)(z+0.9464)}. \quad (13)$$

It is noticed that the proposed minimum phase recursive digital differentiator design $H_{d1}(z)$ i.e., given in Eq. (13) has two non-unity real zeros. Therefore, three other designs are obtained by reflecting one or more zeros of differentiator design $H_{d1}(z)$ as in [14]. These additional designs have same magnitude responses as of the original differentiator design $H_{d1}(z)$ but having the different phase responses. The transfer functions of recursive digital differentiators thus obtained are given in Eqs. (14)-(16):

$$H_{d2}(z)=\frac{0.5158(z-1)(z+1.9387)(z+0.9445)}{T(0.8655)(z+0.1066)(z+0.5871)(z+0.9464)}. \quad (14)$$

$$H_{d3}(z)=\frac{0.9445(z-1)(z+0.5158)(z+1.0588)}{T(0.8655)(z+0.1066)(z+0.5871)(z+0.9464)}. \quad (15)$$

$$H_{d4}(z)=\frac{0.4872(z-1)(z+1.9387)(z+1.0588)}{T(0.8655)(z+0.1066)(z+0.5871)(z+0.9464)}. \quad (16)$$

3. Comparisons

It is noticed that the recently published Upadhyay integrator and differentiator designs of fourth-order systems have nearly ideal magnitude responses over $0 \le \omega \le 0.84\pi$, but simultaneously these designs have large amount of relative error in magnitude response over $0.9\pi \le \omega \le \pi$ [14]. Therefore, the accuracy of proposed recursive digital integrator designs $H_{i1-8}(z)$ and differentiator designs $H_{d1-4}(z)$ is compared with the existing US and JGJ designs. The transfer functions of US [12] and JGJ [13] designs are given in (17, 18) and (1, 19), respectively.

$$H_{usi}(z)=\frac{0.8657T(1+0.681z^{-1}+0.0628z^{-2})}{(1-0.4975z^{-1}-0.5025z^{-2})}. \tag{17}$$

$$H_{usd}(z)=\frac{0.5805(1+0.99z^{-1}-1.99z^{-2})}{T(1+0.681z^{-1}+0.0628z^{-2})}. \tag{18}$$

$$H_{jd}(z)=\frac{(1-0.4812z^{-1}-0.5142z^{-2})}{T(0.8647+0.5998z^{-1}+0.0541z^{-2})}. \tag{19}$$

It is observed that the accuracy of proposed and the existing designs is nearly same over $0\le\omega\le0.94\pi$. Therefore, Figs. 1-4 show the PREs of proposed and the existing designs in magnitude responses with the ideal ones over different Nyquist frequency ranges as $0\le\omega\le0.94\pi$ and $0.94\pi\le\omega\le\pi$.

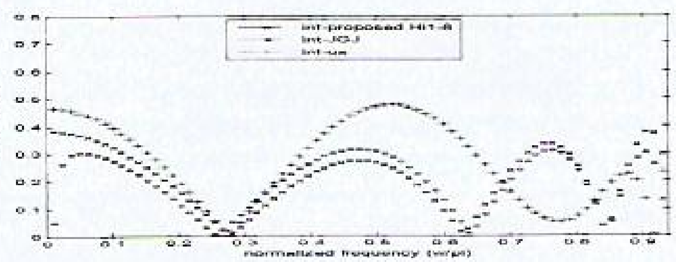

Fig. 1: PREs of proposed and the existing digital integrators over $0\le\omega\le0.94\pi$

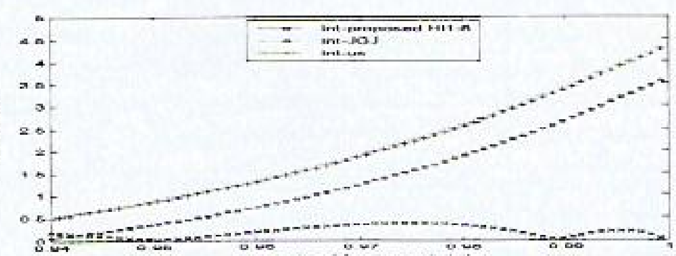

Fig. 2: PREs of proposed and the existing digital integrators over $0.94\pi\le\omega\le\pi$

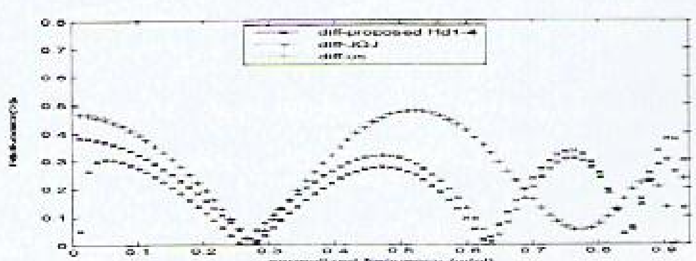

Fig. 3: PREs of proposed and the existing digital differentiators over $0\le\omega\le0.94\pi$

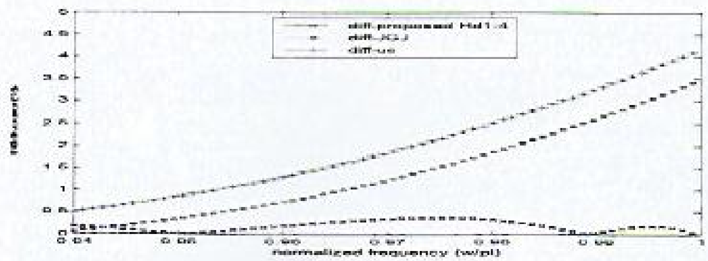

Fig. 4: PREs of proposed and the existing digital differentiators over $0.94\pi \leq \omega \leq \pi$

From Figs. 1-4, it is observed that the designed recursive digital integrators $H_{i1-8}(z)$ and differentiators $H_{d1-4}(z)$ of third-order systems have MPREs of 0.38% in magnitude responses over the full Nyquist band with the ideal ones; while the existing US [12] designs have MPREs of 0.48% up to the Nyquist frequency $\omega = 0.94\pi$, 2.56% up to $\omega = 0.98\pi$ and 4.2% over the full Nyquist band. Further, it is observed that the proposed and the existing JGJ [13] designs have MPREs of 0.3% in magnitude responses with the ideal ones over the Nyquist frequency ranges of $0.11\pi \leq \omega \leq 0.89\pi$ and $0.026 \leq \omega \leq 0.95\pi$, respectively. The observations of Figs. 4 and 6 clear that the existing US and JGJ designs have almost 4.2% and 3.5% relative errors near to $\omega = \pi$, while the proposed designs have only 0.38% relative errors over the full Nyquist band (including $\omega = 0$ and $\omega = \pi$). It can be easily seen that the JGJ designs have large amount of relative errors in magnitude responses over the Nyquist frequency range of $0 \leq \omega \leq 0.025$ with the ideal ones.

It is interesting to note that the recently published recursive digital integrator and differentiator designs of third-order systems have MPREs of 3.16% over the full Nyquist band [9], while the proposed designs of same order have MPREs of only 0.38% over the full Nyquist band. The phase responses of designed full band recursive digital integrators $H_{i1-8}(z)$ and differentiators $H_{d1-4}(z)$ are shown in Figs. 5 and 6, respectively.

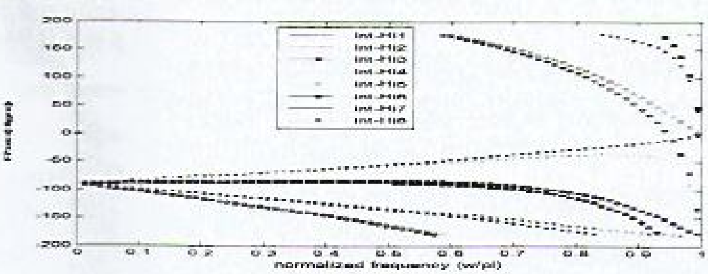

Fig. 5: Phase responses of designed recursive digital integrators $H_{i1-8}(z)$

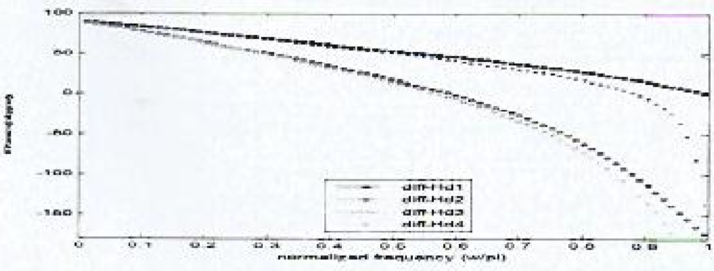

Fig. 6: Phase responses of designed recursive digital differentiators $H_{d1-4}(z)$

From Fig. 5, it is observed that the designed recursive digital integrator $H_{i1}(z)$ i.e., given in (5) has nearly ideal linear phase response over the full Nyquist band and the integrator $H_{i3}(z)$ i.e., given in (7) has almost ideal phase response of -90^0 over the Nyquist frequency range of

$\omega \le 0.75\pi$. Further from the observations of Fig. 6, it is clear that the designed minimum phase recursive digital differentiator $H_{d1}(z)$ i.e., given in (13) has nearly ideal linear phase response over the full Nyquist band.

Fig. 7 shows the absolute phase errors (APEs) of proposed recursive digital integrator $H_{i1}(z)$ and the differentiator $H_{d1}(z)$ in phase responses over the full Nyquist band with the ideal linear phase responses. This figure also shows the APE of another proposed recursive digital integrator $H_{i3}(z)$ in phase response over the full Nyquist band with the ideal phase response of -90^0.

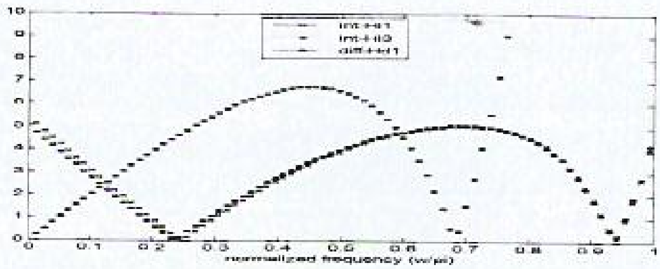

Fig. 7: APEs of designed integrators $H_{i1,3}(z)$ and differentiator $H_{d1}(z)$

From Fig. 7, it is observed that the designed minimum phase recursive digital integrator $H_{i1}(z)$ and the differentiator $H_{d1}(z)$ have maximum APEs of 5^0 in phase responses over the full Nyquist band with the ideal linear phase responses. Further, it is observed that the proposed recursive digital integrator $H_{i3}(z)$ has maximum APE of 6.7^0 in phase response with the ideal phase response of -90^0 over the Nyquist frequency range of $0 \le \omega \le 0.75\pi$.

4. Conclusions

The results show that the designed recursive digital integrators and differentiators have MPREs of 1.39% in magnitude responses over the full Nyquist band (including the extremes $\omega = 0$ and $\omega = \pi$) with the ideal ones, while the currently available full band designs in literature have MPREs of 3.16% in magnitude responses over the full Nyquist band. It is also shown that the designed recursive digital integrator $H_{i1}(z)$ and differentiator $H_{d1}(z)$ have maximum APEs of 5^0 in phase responses over the full Nyquist band with the ideal linear phase responses. Finally, it is shown that one of the proposed recursive digital integrator designs $H_{i3}(z)$ has maximum APE of 6.7^0 in phase response over the 75% of Nyquist band with the ideal phase response of -90^0. Thus, the proposed full band recursive digital integrator and differentiator designs of third-order systems may be the better alternate of existing recursive and non-recursive designs.

References

[1] A.S. Sidra and K.C. Smith: *Microelectronic Circuits* (Oxford Univ. Press, USA 2004).

[2] M.A. Al-Alaoui: Novel approach to designing digital differentiators, *Electron. Lett.*, vol. 28 (15), pp. 1376–1378, 1992.

[3] M.A. Al-Alaoui: Novel digital integrator and differentiator, *Electron. Lett.*, vol. 29 (4), pp. 376–378, 1993.

[4] J.L. Bihan: Novel class of digital integrators and differentiators, *Electron. Lett.*, vol. 29 (11), pp. 971-973, 1993.

[5] M.A. Al-Alaoui: Novel IIR differentiator from the Simpson integration rule, *IEEE Trans. Circuits Syst. I, Fundam. Theory Appl.*, vol. 41 (2), pp. 186-187, 1994.

[6] M.A. Al-Alaoui: A class of second-order integrators and low-pass differentiators, *IEEE Trans. Circuits Syst. I, Fundam. Theory Appl.*, vol. 42 (4), pp. 220-223, 1995.

[7] N. Papamarkos and C. Chamzas: A new approach for the design of digital integrators, *IEEE Trans. Circuits Syst. I, Fundam. Theory Appl.*, vol. 43 (9) (4), pp. 785-791, 1996.

[8] N.Q. Ngo: A New Approach for the Design of Wideband Digital Integrator and Differentiator, *IEEE Trans. Circuits Syst. II, Exp. Briefs*, vol. 53 (9), pp. 936-940, 2006.

[9] M. Gupta, M. Jain and B. Kumar: Novel class of stable wideband recursive digital integrators and differentiators, *IET Signal Process.*, vol. 4 (5), pp. 560-566, 2010.

[10] D.K. Upadhyay: Recursive wideband digital differentiators, *Electron. Lett.*, vol. 46 (25), pp. 1661-1662, 2010.

[11] M.A. Al-Alaoui: Class of digital integrators and differentiators, *IET Signal Process.*, vol. 5 (2), pp. 251-260, 2011.

[12] D.K. Upadhyay and R.K. Singh: Recursive wideband digital differentiator and integrator, *Electron. Lett.*, vol. 47 (11), pp. 647-648, 2011.

[13] M. Jain, M. Gupta and N. Jain: Linear phase second order recursive digital integrators and differentiators, *Radio Engineering Journal*, vol. 21 (2), pp. 712-717, 2012.

[14] D.K. Upadhyay: Class of recursive wideband digital differentiators and integrators, *Radio Engineering Journal*, vol. 21 (3), pp. 904-910, 2012.

Information Engineering Letters, ISSN: 2163-4114
Volume 3, Number 3, September, 2013

Static Configuration on FPGA of Fuzzy-ART Neural Network

Yahiaoui Réda[a], Alilat Farid[b], Loumi Saliha[c]
Université des Sciences et de la Technologie Houari Boumediene, Alger
[a]ryahiaoui@hotmail.fr, [b]faralilat@yahoo.fr, [c]salihaloumi@yahoo.fr
doi.10.5729/iel.vol3.issue3.65

Keywords: Artificial Neural Networks, ART, Fuzzy ART, Learning, Multispectral classification, Remote Sensing, FPGA.

Abstract. This article presents the implementation of a neural network architecture to the family of ART (Adaptive Resonance Theory), performed on a FPGA with static reconfiguration. This is to give one configuration to the system to meet the needs of an application. we operate the proposed architecture to achieve the same configurable circuitry the two fundamental steps in our network: learning and generalization. We propose an architecture and its validation by the implementation of the multi-spectral classification of a satellite image with Fuzzy ART. Since, FPGAs are limited by the number of resources available on an embedded map, the proposed architecture takes the maximum benefit from these resources. The characteristic and performance of this implementation are compared with those obtained by a purely software version developed with MATLAB.

1. Introduction

In our daily life, the image plays an increasingly role to inform us or entertain us. In parallel, the information processing has also developed through the development of microelectronics systems offer more efficient to execute complex algorithms. Research the computing power has given rise to various types of computers [1,2]. Many parallel machines have emerged since the early 80s. Mention may be made for example Warp [3] and CLIP7A [4]. Advances in the ability to integrate electronic circuits have opened new perspectives for the real-time image processing in embedded systems. On the one hand, specific processors are commonly perform billions of operations per second and on the other hand, reprogrammable components have billions of logic gates. These circuits allow implement applications with performance in terms of computing time ever growing. In this context, the FPGA (Field Programmable Gate Array) with its large integration capabilities and reconfiguration are a key component to quickly develop prototypes. Splash2 [5] is an example of this evolution. The interest generated by the FPGA is mainly due to their affordability, easy of implementation, flexibility and computational power [6].This exploitation of the reconfigurability, more or less sophisticated, depending on the technological characteristics of FPGAs, but also the spirit in which it is implemented. There are two modes of reconfiguration. The first method uses a static configuration, for which we have a system configuration by applying (reconfiguration between applications) [7].The second uses a dynamic mode of reconfiguring the system several times during the execution of the same application [8]. During the marketing of the first programmable pre-broadcast (FPGA) in 1985, the use of these circuits are constantly expanding to various fields and applications, among which we can mention the image processing [9,10], neural networks [10], etc ... Indeed, these reconfigurable circuits allow take advantage of the inherent parallelism of neural networks and open up new prospects for use in fields, until then deprived of such a computing power. Since 1943, several hardware implementations of neural networks have been conducted by large companies such as IBMand Intel [9]. They differ in the number of neurons emulated precision in bits, the number of synapses and the speed of the learning process.Several specific to the Fuzzy ART algorithm properties facilitate a hardware implementation and explain its adoption for a hardware implementation for a categorizingapplication. This algorithm offers simplified calculations for the formation of classes as hyper-box, unlike circular classes such as those found for most neural network algorithms. This algorithm runs in two steps based on two criteria of distance or activation and choice. It lends itself to parallel processing, offers good categorization results with moderate accuracy of the weight of neurons and the multiplication is not required in the synapses. We have focused our research on the implementation of networks such as Fuzzy-ART. We propose in this paper a static reconfigurable architecture meets the constraints of learning neural networks of the family of ART and the generalization of a multi-spectral classification of a satellite image remote sensing of Algerian satellite Alsat-1 on FPGA. This solution incorporates the major constraint is the minimization of the use of logic resources.

2. Network Fuzzy-ART

The network used is the Fuzzy-ART which belongs to the networks of hétéro-associative neurons of the family of Article This family has a rather complex architecture. Composed of three subsets inter acting: the subset of attention (F0, competition), the subset of orientation (F1, comparison), and a control system of the factor of attention (F2 layer) [11].

Fuzzy-ART [12] is a recurring and resonant competitive network not supervised in phase of training. It has three layers of neurons as illustrated on Figure 1.

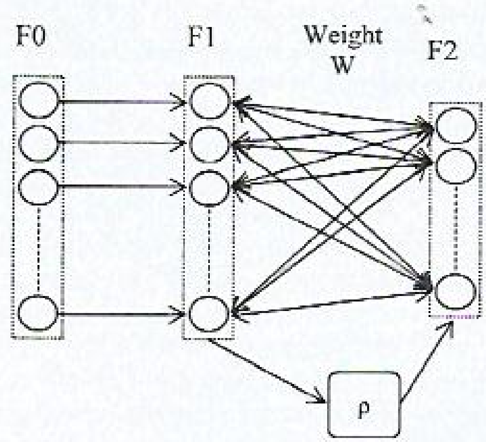

Figure 1.Fuzzy-ART architecture

- The F0 data preparation layer receives the body of the input vector blur I. This layer has a number of nodes twice the size of a vector of data, due to a coding complement a_c.
- The comparison layer F1 has the same number of nodes as F0. Each node is connected to node F1 the same order of F0 by a weight equal to '1 '.
- The competition F2 layer is fully interconnected to F1. Each node j in F2 is connected to all nodes in F1. There Wj the adaptive weight vector associated. T is the activation of the F2 layer vector.

The Fuzzy ART network is characterized by three parameters: selection parameter α, β the learning rate, and the rate of vigilance ρ. These settings must meet the following conditions: $\alpha > 0$, $0 < \beta < 1$, $0 < \rho < 1$.The algorithm of the Fuzzy ART network is described in the flow chart shown in Figure 2.

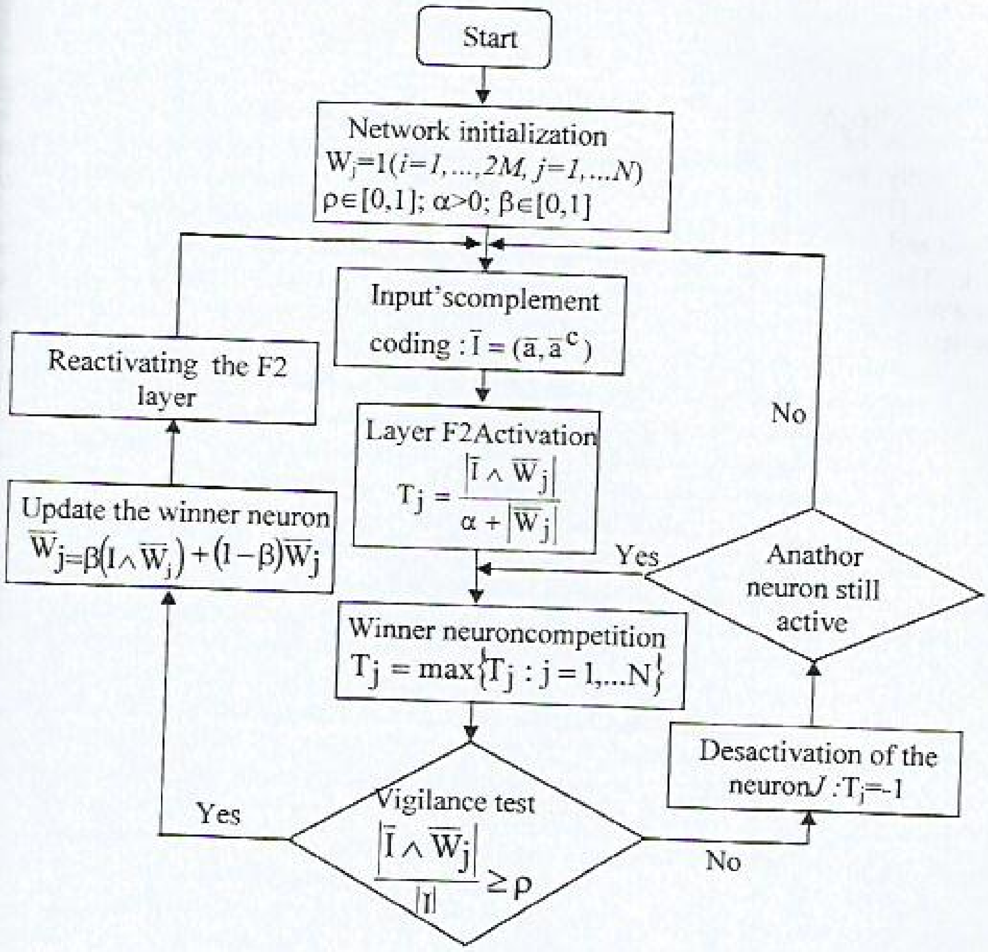

Figure 2. Flow chart of Fuzzy-ART

2.1 Software implementation

The difficulty of such networks lies in the fact that it is unsupervised, competitive, scalable and has a recurring resonant learning phase. In this section, we propose an implementation of the algorithm of the Fuzzy-ART on MATLAB environment that we organized in three (03) steps:learning,test of learning andgeneralization.

1. We developed the learning algorithm, in this phase we look for the best network parameters (selection parameter α, β the learning rate, and the rate of vigilance ρ), which give the average rate of good classification noted ARGC.
2. We tested our network after his learning on the basis the control already created. This phase should provide us with a good value of ARGC, which will validate the results before generalization.
3. In this part we get the parameters (α, β and ρ) and the weight vector (W) gave the best TMBC in the learning phase. The classification was tested on several images corresponding to several regions acquired at different date micro Algerian satellite ALSAT-1.

2.2 Hardware / software interface

The Fuzzy ART algorithm presented above has been focused on Virtex 6 broadcast connectivity kit with a FPGA family Xilinx Virtex 6 (XC6VLX240). This kit receives and transmits the data via the series port by a software developed on MATLAB. The process is done by technology UART (Universal asynchronous receiver/transmitter) of the series port of the chart and the PC.

3. Fuzzy ART architecture on FPGA

The main advantage of FPGAs is parallel processing data. This property gives the network faster than the software-only version of learning. Figure 3 shows the architecture created on a Virtex 6 for the implementation of neural network Fuzzy-ART.On this architecture seven (7) blocks are configured. Initially, the *config* entry directs the application to run by taking the choice on learning or generalization [10]. This choice being made, through the block of data, the input raw *Data*will be complement and the prototypes required to provide the comparison to the weight vector W of the second block. The activation block performs the addition of the minimum values between the prototype and the weight vector W. This sum is then divided by the sum of prototypes and selection parameter α. Block competition, through a comparator, stockes the value of Tj max and position.

Depending on the value of the LSB of the *config* input, the application block selects one of two predefined operations: learning or generalization. Indeed, for a value of '0 ', the operation will allow generalization to present output Class, the class prototype (input MUX) block competition. As against a value of '1' will take learningmode. In this case, the block of vigilance test divides the output received by the activation block Tj (denoted L1) by the sum of prototypes present at the input and compares rates of vigilance parameter ρ:

- If it is greater than or equal to L1, the selected neuron has not won and returns to block competition to find another neuron. If it does not exist a new neuron is added to the network.
- By cons, if ρ is less than L1, the block update is enabled for the storage of weight vector of the winning neuron in the RAM dedicated to this operation.

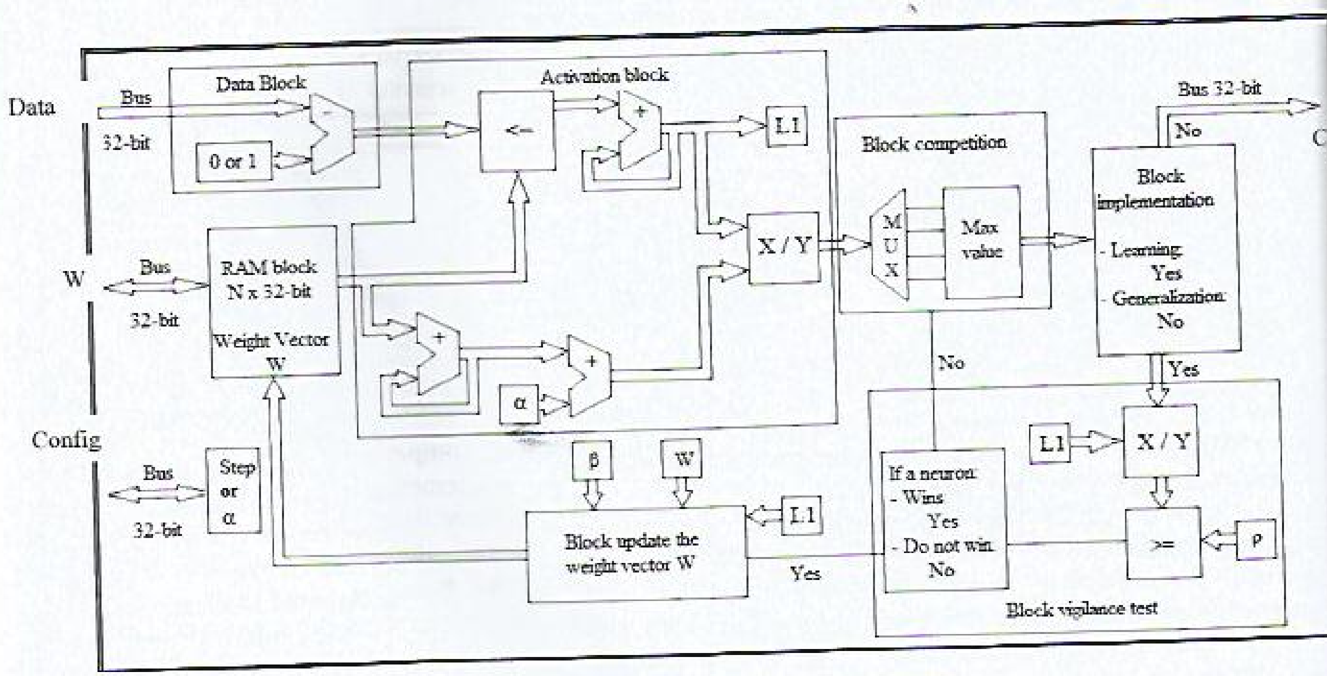

Fig. 3,Fuzzy-ART architecture developed on FPGA.

3.1 Status of the inputs / outputs of the FPGA in two configurations

The FPGA receives the data in the *Data* entry, and the entry *config*. The bit of LSB of *config*, the 2^{-30} of figure 4 is put at "1" for learningand the remainder of the bits will code in fixed point the step of the parameters. At the end of the phase of the learning, the FPGA present at exit *config* the value α and the vector weightW on the output. During generalization, the bit of LSB of *config*, the 2^{-30} of fig. 4, is put at "0" for a classification and the remainder of the bits will code in fixed point the parameter α. At the end of the process, we recover the data of categorization in the port *class*.

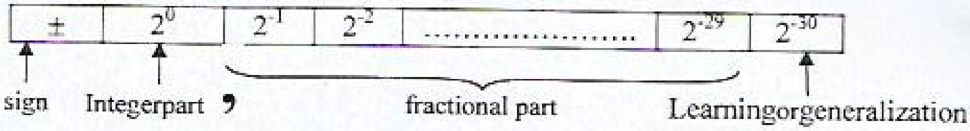

Figure 4. *config* Port Configuration

3.2 Resources

As part of this work, we sought to develop an architecture to minimize the use of logic resources, this architecture is eventually led to only be part of a global circuit. The resources required for this architecture are given in Table 1.

Table 1.Material resources of the implemented circuit.

occupied / available			
Silices	FlipFlops	LUTs	IOs
4530 / 37680 12%	76801 / 301440 25%	65112 / 241152 27%	99 / 360 27%

4. Results

Our work consists in carrying out an application embarked time-reality on a reconfigurable circuit of type FPGA. This application gathers the training of Fuzzy-ART and its generalization for the multispectral classification of a satellite image taken by Algerian satellite ALSAT-1. With this intention we start for the software part, by developing all the network of neuron on MATLAB, then follows a description in a material language of type VHDL for the implementation part in an embarked system. We chose four classes: water, urban, forest and bare soil or agricultural. We extracted from this image two bases of samples, a base of training and a base of control. The characteristic and the performances of this implementation are compared with that obtained by a purely software version developed under MATLAB. The criteria of evaluation, we chose the average rate of good classification (ARGC) and the execution time of the application.

$$\mathrm{ARGC} = \frac{Number\ of\ pixels\ correctly\ classified}{Number\ of\ pixel\ control\ database} \times 100\% \tag{1}$$

4.1 Data and feature satellite

The data are classified from the Algerian satellite ALSAT-1 whose main characteristics are summarized in Table 2.

Table 2. Technical Specifications of micro satellite Alsat-1.

Shooting mode	**Push-Broom**
Multispectral sensor	02 cameras covering 16 km
spectral bands	Green, Red , Infrared
Swath	2 x 300 Km
Number of pixels	10200 /camera
spatial resolution	32m
Size of the scene	600 x 560 Km

We extracted two bases samples. Table 3 contains the number of samples considered for each class and each frame.

Table 3.Distribution of samples in each class.

Class Sample bases	**Water**	**Urban**	**Soil or agricultural**	**Forest**
Learning	*250*	*250*	*250*	*250*
Control	*125*	*125*	*125*	*125*

4.2 Performance

Until today there is no method to specify parameter values (α, β, ρ) of the ART network necessary to obtain a good classification. We were led to vary these parameters in the interval [0 1] with several steps and calculate the rate of correct classification. At the end of this study, and for illustrative purposes, we have grouped in table 4, the values obtained for three (3) different pitches: 0.1, 0.01, and 0.001.

Table 4.Network performance for basis control.

Step	$\alpha - \beta - \rho$	ARGC (%)	MATLAB (Learning Time)	FPGA (Learning Time)
0.1	0.6000 - 0.2000 - 0.3000	72	7 min	9 sec
0.01	0.5800 - 0.1500 - 0.4200	85	2 heurs	8 min
0.001	0.5910 - 0.1580 - 0.3720	97	5 heurs	40 min

The parameters obtained in the learning phase gave a very good learning, because the best generalization based control 500 samples gave an average rate of correct classification (TMBC) of 97%. These results obtained with the software implementation is identical to the result of the hardware implementation on FPGA, the difference is of course in the execution time. The clock frequency is 200MHz FPGA.

For a better appreciation of the results, we propose an estimation of the quality of the classification of the Fuzzy-ART network. For each class, we consider the rate points correctly classified and misclassified point rate base test. Figure 5 summarizes the results.

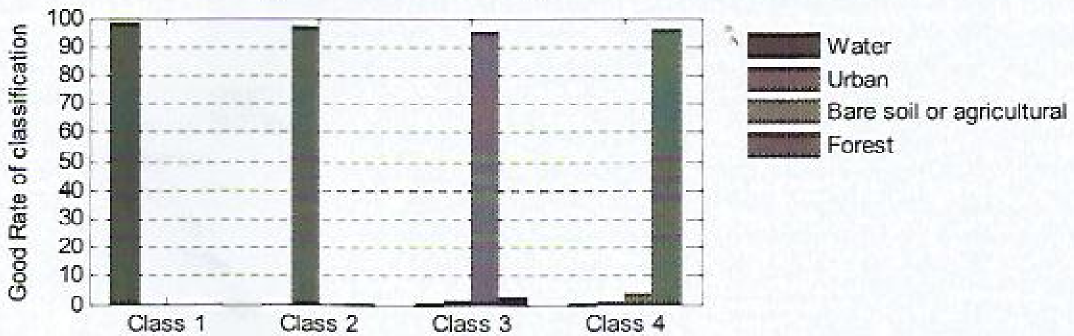

Figure 5. Classification Fuzzy ART network for step 0.001.

In view of these results, it appears that there is some confusion between the class or bare agricultural land and forests class. It is predictable to the extent that these two classes are very similar. Figure 6 shows the spread on any image from the satellite Alsat-1.

(a)

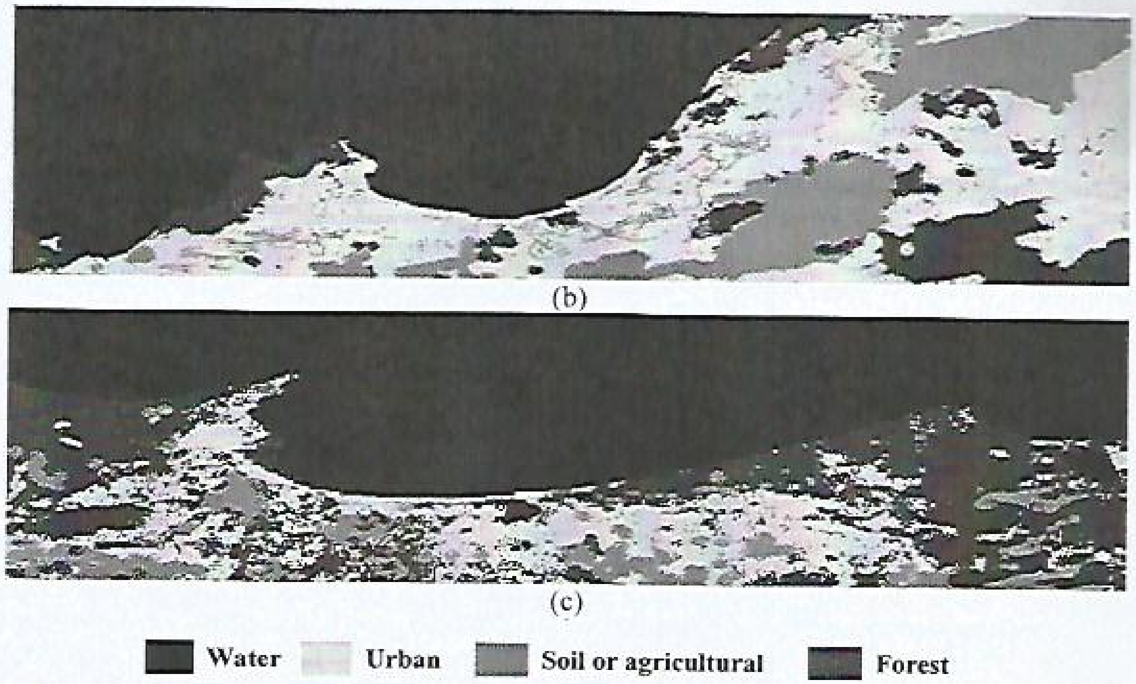

Figure 6. Images classified by the Fuzzy-ART network developed on FPGA.

(a) Bay of Algiers (Center), (b): Bay of Oran (East), (c): Bay of Annaba (West)

5. Conclusion

In this paper, an architecture implementing the static reconfiguration of FPGAs is presented. The main objective is to build a hardware demonstrator covering several aspects: architecture, development methods and applications. We presented a static configurable FPGA architecture for the neural network comprising Fuzzy ART learning and generalization. This architecture is of course valid for satellite multi spectral image with three channels of representation of the image. Learning and generalization developed on the FPGA has a very good quality of classification (in this case 97%). The circuit shown operates optimally technology reconfigurable FPGAs. The presented architecture takes full advantage of the intrinsic resources available on this circuit FPGAs. It offers very low occupancy logical resources, which allows you to use such algorithms in combination with other treatments. Indeed, this is even more interesting, the logical resources saved can then be used to implement other types of algorithms as pretreatment of the data presented to the network, operations standards, post-treatment, for example. Moreover, we confirmed the feasibility of porting applications of real-time computing complex on current reconfigurable circuits.

Future work will examine the implementation of the network with a static to a reconfigurable architecture appear with the architecture presented in this paper. More complex work of the same family ART and spiking neural networks are designed for architecture on FPGA circuits.

References

[1] Mc Cullogh W.S. & Pitts W., 1943. A logical calculus of the ideas immanent in nervous activity. Bulletin of Mathematical Biophysics, Vol. 5, pp. 115-133.

[2] Stuart Russell and Peter Novig. Artificial intelligence 3rd edition. 2010 Pearson Education France

[3] M. Annaratone, E. Arnould, T. Gross et al., « The Warp Computer: Architecture, Implementation, and Performance », IEEE Transactions on Computers, Vol. C-36, No.12, 1987.

[4] T. J. Fountain, K. N. Matthews, M. J. B. Duff, « The CLIP7A Image Processor », IEEE transactions on Pattern Analysis and Machine Intelligence. Vol. 10, No. 3, 1988.

[5] D. A. Buell, J.M. Arnold, W.J. Kleinfelder, « Splash 2, FPGAs in a custom computing machine », IEEE Computer Society Press, Los Alamitos, 1996.

[6] Shah,S.K. ; Vishwakarma,D.D. Communication, Networks and Satellite (ComNetSat), 2012 IEEE International Conference on "FPGA implementation of ANN for reactive routing protocols in MANET".

[7] Frangieh, T. ; Chandrasekharan, A. ; Rajagopalan, S. ;Iskander, Y. ; Craven, S. ; Patterson,C.Parallel & Distributed Processing, Workshops and Phd Forum (IPDPSW), 2010 IEEE International Symposium on "PATIS: Using partial configuration to improve staticFPGA design productivity"

[8] Mehmet Ali Cavuslu, Cihan Karakuzu, Fuat Karakaya. Neural identification of dynamic systems on FPGA with improved PSO learning. Elsevier 17 March 2012.

[9] Ye Li ; Qingming Yao ; Bin Tian ; Wencong Xu. Vehicular Electronics and Safety (ICVES), 2011 IEEE International Conference on "Fast double-parallel image processing based on FPGA".

[10] R.Yahiaoui, F.Alilat, S.Loumi, Information Science and Technology (CIST), 2012 Colloquium in "Implementation of fuzzy-ART on FPGA: Classification of the Algiers's Bay".

[11] F. Alilat, S. Loumi, H. Merrad , B. Sansal, "Nouvelle approche du réseau ARTMAP Flou Application à la classification multispectrale des images SPOT XS de la baie d'Alger", Revue Française de Photogramétrie et de Télédétection SFPT, (2005-1),.no.177, pp 17-24, 2005.

[12] Carpenter G. A., Grossberg S. & Rosen D. B.,. Fuzzy ART : An Adaptive Resonance Algorithm for Rapid, stable classificationof Analog Patterns. Proc. International Joint Conference of Neural. 1991

Information Engineering Letters, ISSN: 2163-4114
Volume 3, Number 3, September, 2013

Modeling of an Ubiquitous Building Energy Management System

JrJung Lyu [a], Han-Chi Fu [b]

Department of Industrial and Information Management, National Cheng Kung University, Tainan,Taiwan, ROC.

[a]jlyu@mail.ncku.edu.tw, [b]r3895110@mail.ncku.edu.tw

doi.10.5729/iel.vol3.issue3.73

Keywords: Soft System Dynamics Methodology, Ubiquitous Sensor Networks, Energy Management System, Policy Analysis

Abstract. A modern building energy management system (BEMS) integrates the ubiquitous sensor network (USN) technology in order to monitor and control the environment in real time. Such kind of the internet of things (IOT) application involves with complicated networking communication technologies and the associated behaviors of system users, where the design and implementation issues are often too difficult to be handled by traditional system analysis approach. This work applies the Soft System Dynamics Methodology (SSDM) as basis to model a ubiquitous BEMS. We demonstrate it is not only feasible, but can provide insights in analyzing such a complicated system using the proposed approach.

1. Introduction

A great proportion of the energy consumption is in the buildings (Raftery et al., 2011). In this energy lacking ages, the building energy management system (BEMS) has therefore played an important position. In many countries, developing zero energy building (ZEB) or low energy building (LEB) have become their prerequisite mission (Djuric and Novakovic, 2012). The main target of the BEMS is to decrease the energy consumption and to increase the energy utilization via an effective monitoring and controlling system (Foley, 2012). In general, a BEMS is an integrated management system which monitors different sub-systems, such as electronic system, HVAC (heating, ventilation, and air conditioning) system, and security system. Several companies have using the information and communication technology (ICT), such as ubiquitous sensor network (USN, Lertlakkhanakul et al., 2010), to develop a modern BEMS which can remotely access, transmit, sharing, analysis, and control energy data through online system in real-time.

Although the availability of the USN enabling the ubiquitous BEMS, the planning and implementation issues, considering wide different behaviours of the system users, would still be a challenge. As reported, the interactions among different system users would raise the complexity in managing system (McIntyre and Pradhan, 2003). Furthermore, the status of energy consumption changed dynamically, and the traditional system analysis is difficult since the energy management is not so rigid to analyse. To deal with the analysis problem and to provide a decision feedback loop, this study applied the soft system dynamics methodology (SSDM), which was a composite method of the soft system methodology (SSM, Ngai et al., 2012) - to discover the cause and effect of the problem, and the system dynamics (SD, Wong et al., 2012) - to present the problem and to simulate its effects (Barrenetxea et al., 2008; Rodríguez-Ulloa et al., 2011). This manuscript would model a complicated BEMS using a systematic analysis approach that basically modified from SSDM. The application of the proposed approach was to illustrate how hidden problems and extended issues would be revealed in advance and the managers could design and implement a modern BEMS effectively for the case hotel.

2. Energy management in buildings

Global buildings accounted for approximately 40% of world energy in developed countries, 25% of forest or timbers, and 16% of fresh water (Perez-Lombard et al. 2008). 50% of Carbon dioxide and 70% of sulfur dioxide also came from the buildings (Santamouric, 2006). However, buildings were widely reported to operate inefficiently (Piette et al., 2001; Ardehali et al., 2003), and thus, it was naturally to get better building energy management (Urge-Vorsatz & Novikova, 2008; Cárdenas et al., 2012). The building energy management involved with a rigid process of optimizing the energy utilization and was multidisciplinary in nature, combining the skills of architecture, engineering, management, cost and others to carry out the required functions (Lee et al., 2011). The complicated managerial criterions required for a comprehensive and instantaneous management system such as the BEMS to integrate all kinds of information from various sub-systems (Cárdenas et al., 2012).

The traditional BEMS originated from the building automation system (BAS) which was an intelligent computer-based control system and was designed to control and monitor the mechanical and electronic devices in a building. Compared to the non-controlled building, the energy efficiency and cost was improved by the independent management system. However, the dramatically increasing energy demand and the complicated energy management tasks made the traditional BEMS no longer efficient enough to be acceptable. Managers were seeking a better way to integrate wide difference subsystem with the management platform, which is expected to provide the real-time system control.

Modern BEMS was different from the traditional one in the application of ICT to develop the wed-based building remote diagnosing and controlling system. The element of modern BEMS consisted of decision making, energy auditing, identification and implementation of energy measures, monitoring and evaluation (Kannan and Boie, 2003). These elements consist of real-time information communication, network connection, and devices feedback control. Since the chief scientist of Xerox PARV (Palo Alto Research Center), Mark Weiser, proposed the concept of "ubiquitous computing" in 1988 (Weiser & Boehm, 1988), the applications of "ubiquitous computing" in the building energy management were greatly applied. As the Web 2.0, RFID, WSN, and many ICT become cost-effective for the users, the ubiquitous environment is feasible for the system developer. As to a BEMS that operates in a ubiquitous environment, it represents that the managers can monitor and operate the system real-teim and invisibly through the web-based system (Hwang and Yoe, 2011). The modern BEMS smashed the limitation of traditional building management, and increased the whole system interoperability with the so called ubiquitous sensor networks (USN) (Lertlakkhanakul et al., 2010).

The USN could be added without disrupting the indoor decoration or comfort (Bleda et al., 2012). Applying this technology, one could collect the environment parameters of different phenomena, such as temperature and humidity, and then transformed the collected data into electronics signals and sent them to the gateway simultaneously. Also, from the feedback of the USN, the improper behaviours of using energy including the obliviousness in energy using and incorrect electric devices operating could be avoided. This greatly improved the ability of the modern BEMS which could quickly response the environment variation and prevented from unnecessary energy loss.

An ubiquitous BEMS which adopted the USN could administer building energy simultaneously. But the problems arose when new devices and networks were installed in existing buildings that lack of infrastructural support and feasible implementing plan. Host of technical, implementation, and systems design issues were often underestimated when it came to the new technology adoption. That is, adding new facilities or making changes to the existing building can be very challenging and expensive (Markovic et al., 2012). For a system developer, implementing the ubiquitous BEMS was a complicated task that required close cooperation and coordination between various system users and devices providers. The ongoing problem with the deployment of ubiquitous energy system had shown that implementation was largely determined by broad social acceptance issues, and the social impact of new technologies was also hard to predict (Wolsink, 2011).

3. A systematic evaluating approach

Checkland proposed the SSM in 1981 to analyze and model the managerial issues which were usually complicated and hard to define (Checkland, 1981; Reisman & Oral, 2005). Compared to the systems engineering or hard systems which fitted only to the situation that has already known, the SSM focused on dealing with the complicated or unstructured problem including inconspicuous goal, multiple goals, or the circumstances of different hypotheses and perspectives (Jackson, 2001). The SSM consisted of seven stages which separated in "Real World" and "System-Thinking Situation" in dealing with real life problem. Ngai et al. (2012) deemed the SSM as a useful methodology that browsing the real world.

Another well-recognized simulation approach that usually being applied in dealing with social dynamic issues was SD. In order to deal with the perplexing social problems, the decision maker not only had to classify the problem types but also had to identify the essential characters of the dynamic system which was hidden behind (Sterman, 2001; Wong et al., 2012). The processes of the SD were divided into three stages. Through the SD analysis, a user can clearly capture the whole system picture and its dynamical behaviours.

Combining the advantage of well-rounded perspective for problem constructing in the SSM and the superior policy analysis ability in the SD, Rodriguez-Ulloa and Paucar-Caceres addressed the SSDM which merged the principles, ideas, philosophies, and techniques of SSM and SD (Rodriguez-Ulloa and Paucar-Caceres, 2005). The Methodology developed three different worlds, (1) the Real World, (2) the Problem-Situation System Thinking World, and (3) the Solving-Situation System Thinking World. These three worlds were further divided into ten systematic stages, including problem defining, problem analyzing, modelling, and possible action planning. Furthermore, general system implementation plan comprised analyzing environment, implementing project, and evaluating benefits (Barrenetxea et al., 2008; Buratti, 2009). Considering the complicated issues involving with the modelling of an ubiquitous BEMS, this study proposed a systematic approach, based on SSDM, for the implementation planning (see Fig. 1), and detailed steps are also as shown.

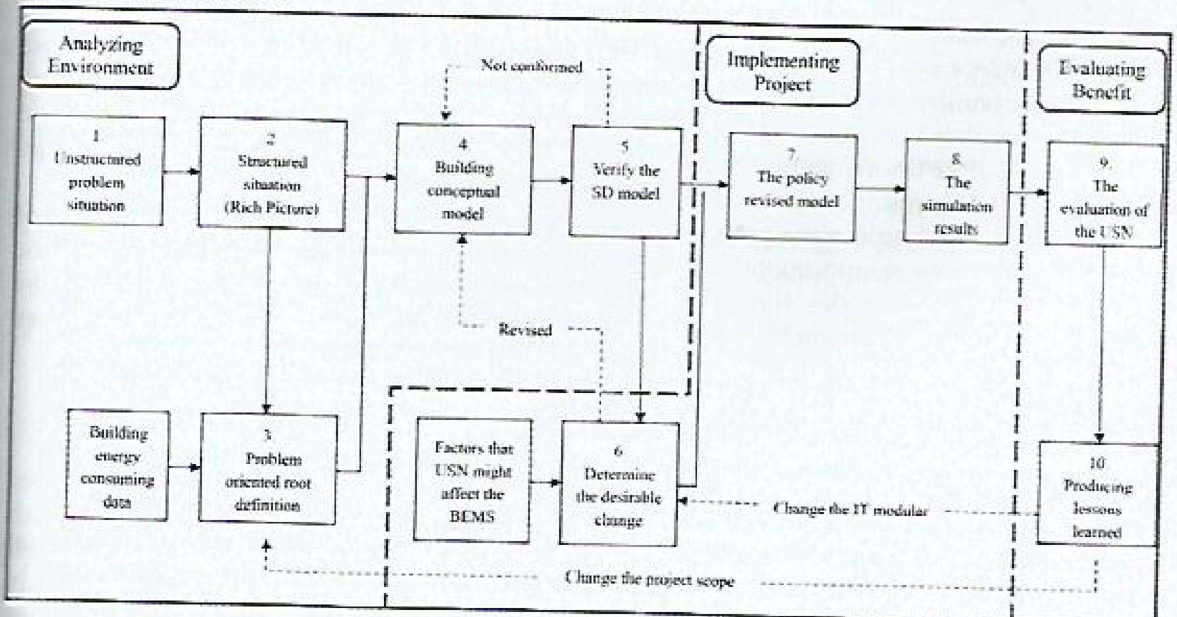

Figure 1. The process to implement an ubiquitous BEMS based on proposed approach

4. Case study

Implementing the ubiquitous BEMS involves with three phases: environment analysis, project execution, and benefits evaluation (Akyildiz et al., 2002; Barrenetxea et al., 2008). In practice, managers require to consider various issues, such as which spaces would be include, how many devices would be used, and which modular would be selected, etc al. Unlike other energy saving techniques which may simply replacing devices, the USN was adopted to avoid manual omission which might waste the energy. The manual omission, however, was much more difficult to control compared to devices replacing. Besides, the manual energy consuming environment was a complex dynamical cycle. These situations resulted in the difficulty to design and justify the ubiquitous BEMS implementation. A case hotel would be used to illustrate the entire process of the ubiquitous BEMS implementation, long-term energy variation observation, and the possible energy saving policies suggestion.

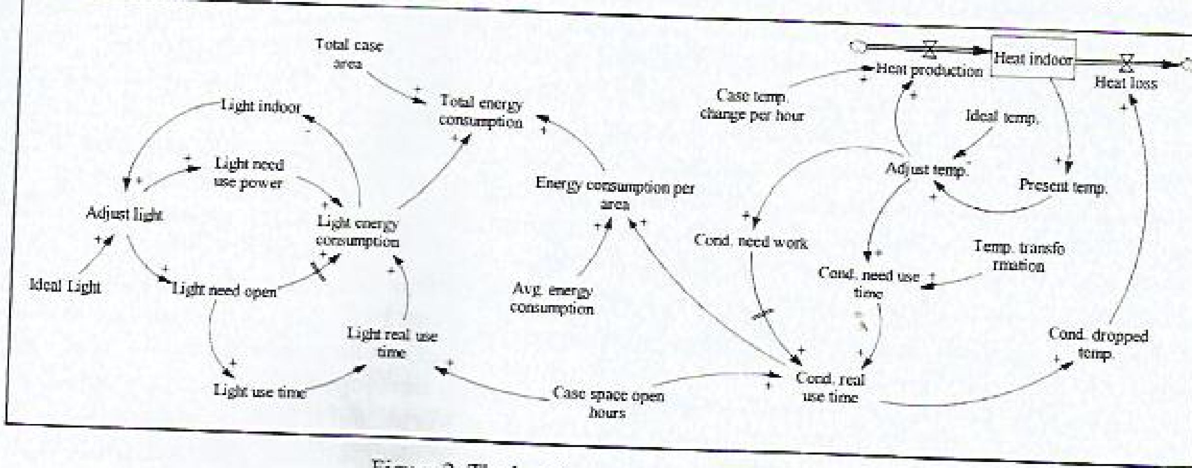

Figure 2. The hotel energy model (HE model)

The hotel energy model (HE model in Figure 2) was based on the activities of the air-conditioners and lighting devices in the implementation space which simulates the dynamic changes of the temperature and brightness. It took "Hour" as the time unit, and therefore the season factor was deleted. The HE model focused on the public space, and thus the situation of the accommodation did not to require to be considered. The HE model was verified based on a case hotel environment data and scenario. The basic data included the area of the implementation space, the opening time of the space, the ideal indoor temperature, the ideal illumination, and the power of the devices set up, where the realistic environment parameters were also recorded. The model was simulated for one month period and the simulated energy used was 9,986.64 watts or 7,190.38 kilowatt-hours. Comparing to the energy usage before the ubiquitous BEMS implementation (about 8,500.1), the retrenched energy was about 14.2%. This result confirmed the energy saving applying an ubiquitous BEMS.

Once the simulation results were positive, the case hotel launched the project. The equipment of the project included one monitoring program, twenty temperature sensors, twenty lighting sensors, and four networks I/O modules (including adaptor, receiver, and transformer). Based on the evaluation of the project, the suggestions were proposed and detailed documents for the project were prepared.

5. Conclusions

The growing environmental awareness exploited a new field of research. Among the energy related studies, the buildings energy management was highly regarded. The energy-saving equipments, such as inverter air-conditioners, fluorescent bulbs, and other green construction materials, were all produced for the purpose of being the green buildings. However, the energy utilization is not only related with the devices, but also concerned with the behaviours of the user. The extra energy usages were considerable in the circumstance of carelessness. To avoid the habitual carelessness in using electric equipments, the applications of the USN to integrate with BEMS was suggested. In order to complete an evaluation process systematically for the ubiquitous BEMS implementing, this study applied the SSDM as the basis for policy analysis. Through a 10 stages process, the managers could estimate the possible energy saving and the benefits of using the ubiquitous BEMS. A case hotel is selected to evaluate the potential saving and the results were promising. The authors expect that, in the future, the implementation of an ubiquitous BEMS would all adopt a systematic approach, such as what we proposed, in order to complete the project in a cost-effective way.

References

[1] Akyildiz, I. F., Su, W., Sankarasubramaniam, Y., and Cayirci, E. Wireless sensor networks: A survey. *Computer Networks*, Vol. 38:4 (2002), p. 393-422.

[2] Ardehali, M., Smith, T., House, J. and Klassen, C. Building energy use and control problems: an assessment of case studies. *ASHRAE Transactions*, Vol. 109 (2003), p. 111-121.

[3] Barrenetxea, G., Ingelrest, F., Schaefer, G. and Vetterli, M. *The hitchhiker's guide to successful wireless sensor network deployments*. Proceedings of the 6th ACM conference on Embedded network sensor systems, Raleigh, NC, USA (2008), p.43-56.

[4] Bleda, A.L., Jara, A.J., Maestre, R., Santa, G. and Gómez Skarmeta A.F. Evaluation of the impact of furniture on communications performance for ubiquitous deployment of Wireless Sensor Networks in smart homes. *Sensors*, Vol. 12:5 (2012), p. 6463-6496.

[5] Cárdenas, J.J., Romeral, L., Garcia, A. and Andrade, F. Load forecasting framework of electricity consumptions for an intelligent energy management system in the user-side. *Expert Systems with Applications*, Vol. 39 (2012), p.5557-5565.

[6] Checkland, D. *Systems Thinking, Systems Practice*: London: Wilkey (1981).

[7] Djuric, N. and Novakovic, V. Identifying variables of energy use in low energy office building by using multivariate analysis. *Energy and Buildings*, Vol. 45 (2012), p.91-98.

[8] Foley, H.C. Challenges and opportunities in engineered retrofits of buildings for improved energy efficiency and habitability. *AIChE Journal*, Vol. 58:3 (2012), p. 568-667.

[9] Hwang, J. and Yoe, H. Study on the Context-Aware Middleware for Ubiquitous Greenhouses Using Wireless Sensor Networks. *Sensors*, Vol. 11:5 (2011), p.4539-4561.

[10]Jackson, M.C. Critical systems thinking and practice. *European Journal of Operational Research*, Vol. 128:2 (2001), p. 233-244.

[11]Kannan, R. and Boie, W. Energy management practices in SME - case study of a bakery in Germany. *Energy Conversion and Management*, Vol. 44:9 (2003), p. 45-59.

[12]Lee, S.-K., Teng, M.-C., Fan, K.-S., Yang, K.-H. and Horng, R.S. Application of an energy management system in combination with FMCS to high energy consuming IT industries of Taiwan. *Energy Conversion and Management*, Vol. 52:8-9 (2011), p. 3060-3070.

[13]Lertlakkhanakul, J., Yoon, S. and Choi, J. Developing a building energy management framework based on ubiquitous sensor networks. *Indoor and Built Environment*, Vol. 19:1 (2010), p. 192-201.

[14]Markovic, D., Cvetkovic, D., Zivkovic, D. and Popovic, R. Challenges of information and communication technology in energy efficient smart homes. *Renewable and Sustainable Energy Reviews*, Vol. 16:2 (2012), p. 1210-1216.

[15]McIntyre, J. and Pradhan, M. A Systemic Approach to Addressing the Complexity of Energy Problems. *Systemic practice and action research*, Vol. 16:3 (2003), p. 213-223.

[16]Ngai, E.W.T., To, C.K.M., Ching, V.S.M., Chan, L.K., Lee, M.C.M., Choi, Y.S. and Chai, P.Y.F. Development of the conceptual model of energy and utility management in textile processing: A soft systems approach. *International Journal of Production Economics*, Vol. 135:2 (2012), p. 607-617.

[17]Perez-Lombard, L., Ortiz, J. and Pout, C. A review on buildings energy consumption information. *Energy and Buildings*, Vol. 40 (2008), p. 394-398.

[18]Piette, M.A., Kinney, S.K. and Haves, P. Analysis of an information monitoring and diagnostic system to improve building operations. *Energy and Buildings*, Vol. 33 (2001), p. 783-791.

[19]Raftery, P., Keane, M. and O'Donnell, J. Calibrating whole building energy model: An evidence-based methodology. *Energy and building*, Vol. 43 (2011), p. 2356-2364.

[20]Reisman, A. and Oral, M. Soft systems methodology: A context within a 50-year retrospective of OR/MS. *Interfaces*, Vol. 35:2 (2005), p. 164-178.

[21]Rodríguez-Ulloa, R.A., Montbrun, A. and Martínez-Vicente, S. Soft system dynamics methodology in action: A study of the problem of citizen insecurity in an Argentinean province. *Systemic Practice and Action Research*, Vol. 24:4 (2011), p. 275-323.

[22]Santamouric, P. M. Recent Progress on Passive and Low Energy Cooling of Buildings. *Singapore* (2006).

[23]Sterman, J. D. System dynamics modeling: Tools for learning in a complex world. *California Management Review*, Vol. 43:4 (2001), p. 8-25.

[24]Urge-Vorsatz, D. and Novikova, A. Potentials and costs of carbon dioxide mitigation in the world's buildings. *Energy Policy*, Vol. 36:2 (2008), p. 642-661.

[25]Weiser, M., & Boehm, H.-J. Garbage Collection in an Uncooperative Environment (1988).

[26]Wolsink, M. The research agenda on social acceptance of distributed generation in smart grids: renewable as common pool resources. *Renewable and Sustainable Energy Reviews*, Vol. 16:1 (2011), p. 822-835

[27]Wong, H. J., Morra, D., Wu, R. C., Caesar, M. and Abrams, H. Using system dynamics principles for conceptual modelling of publicly funded hospitals. *Journal of the Operational Research Society*, Vol. 63:1 (2012), p.79-88.

Volume 3, Number 3, September, 2013
Information Engineering Letters Contents

21634114

ISSN:2163-4114